Inorganic X-ray Mask Technology for Quantum-Effect Devices

William Chu

RLE Technical Report No. 577

April 1993

**Research Laboratory of Electronics
Massachusetts Institute of Technology
Cambridge, Massachusetts 02139-4307**

Inorganic X-ray Mask Technology for Quantum-Effect Devices

by

William Chu

Abstract

The fabrication of quantum-effect devices generally requires the ability to pattern sub-100-nm features. The lithography process needed to fabricate such devices must have sufficient resolution and high yield, for it is often important to measure not just a single device, but rather a wide variety of devices on a single chip in order to observe trends. X-ray lithography satisfies both of these requirements. As part of this doctoral research, a process has been developed whereby x-ray masks, consisting of membranes of silicon-rich, silicon-nitride (SiN_x) can be patterned using either electron-beam or focused-ion-beam lithography, and then electroplated with low-stress Au to form the absorbers. The e-beam or focused-ion-beam exposed masks, called parent masks, are replicated using x-ray lithography to generate second-generation, or daughter masks. Experimental results are presented to show that the deleterious effects of diffraction in x-ray lithography are not as severe as had been anticipated based upon simple diffraction calculations. The daughter masks are then aligned and exposed onto small substrates (smaller than the diameter of the mask membrane) using x-ray lithography. This mask technology will be used to fabricate such devices as the planar resonant-tunneling field-effect transistor (PRESTFET), electron-waveguide devices, multiple parallel one-dimensional conductors, and short-channel MOSFETs. The ultimate goal has been to make the lithography step in the fabrication of such devices simple and routine.

Thesis Supervisor: Henry I. Smith
Title: Keithley Professor of Electrical Engineering

Acknowledgments

There have been so may people who have contributed greatly to this thesis in the way of technical and emotional support that a listing of their names would take up an entire chapter. However, one person who has contributed to this thesis at all stages and in all ways is my advisor Professor Henry I. Smith. From Hank, I have learned to be a scientist; to leave no stone unturned in the search for the truth. When there were problems to be solved, he was always ready to roll up his sleeves and offer his assistance. When there were successes, he was always the first to congratulate me. It has truly been a pleasure and a wonderful experience working for and learning from Hank. I would also like to thank my thesis committee members, Professor Jesús del Alamo and Professor James Chung, profusely for being so understanding and supportive these last months as I was in my mad dash to graduate.

I would also like to give a heartfelt "Thank you" to Dr. Mark Schattenburg, who has given me advice on all aspects of my research. Mark's ideas, energy, and ingenuity are an huge asset to the Submicron Structures Lab. This thesis work would not have been possible without the help of the SSL technical staff. Jim Carter, the lab manager, is truly worth his weight in gold! Jimmy is always there to offer assistance or to suggest a better way to do things. To Jimmy, I am truly indebted. It has also been my pleasure to work with Bob Fleming, Mark Mondol, Jeanne Porter and Bob Sisson. Mark has done all those evaporations for me over all these years and never complained! Thanks Mark! I would also like to thank Donna Martinez for all the times that she's helped me out when I've looked lost in the office.

It has been my pleasure to collaborate with a number of groups in the course of my research. I would like to thank Dr. John Melngailis, Dr. Henri Lezec, Chris Musil, and Mark Shepard of the MIT focused-ion-beam group for their help and support. I

would also like to thank Dr. Stephen Rishton and Dr. Dieter Kern at IBM Yorktown Heights for their work in the e-beam patterning of masks. It has also been my pleasure to work with Dr. Kee Rhee, Dr. Robert Bass, and Dr. Martin Peckerar at the U. S. Naval Research Laboratory. Thank you Kee, for all those masks that you wrote for us on such short notice!

I would also like to thank all those friends and fellow graduate students who worked with me and helped teach me during my tenure at MIT. I have had the pleasure of working with Dr. Khalid Ismail, Dr. Tony Yen, Dr. Yao-Ching Ku, Dr. Erik Anderson, Dr. Alberto Moel, Dr. Kathy Early, Dr. Joseph Kung, Cris Eugster, Ray Ghanbari, Martin Burkhardt, Vincent Wong, Scott Hector, Ken Yee, Albert Young, Nitin Gupta, and Arvind Kumar. I would also like to thank Peter Berlin for being such a wonderful friend during those years at Cornell.

All this would not have been possible without the love and support of my sister Virginia and my parents Chung-Shing and Meyen Chu. My parents have always sacrificed to put the concerns and welfare of their children before their own. I hope that one day that I can be as good a parent for my children as they were for me. Lastly, I would like to express my love and gratitude to a very special person in my life, Isabel Yang, who has helped me in more ways than I can describe. This last year has been the very best of my life, and I look forward to spending the rest of my life with her.

Contents

List of Figures

10

List of Tables

Chapter 1

Introduction

Within the last few years, improvements in materials and microfabrication technology have enabled researchers to fabricate structures and devices where the wave nature of electrons manifests itself in interference and diffraction effects (i.e. quantum-mechanical effects). There has been considerable interest in examining transport properties in, for instance, quasi-one-dimensional (Q1D) conductors in Si [3] and GaAs [4, 5], and interference effects in Aharanov-Bohm rings [6]. In these devices, and many others, the critical dimension was made comparable to, or smaller than a characteristic length – typically the electron mean free path or the electron phase coherence length [7]. Even with the highest quality material, the observation of strong quantum effects generally requires critical feature sizes in the sub-100-nm regime.

In most of the work on quantum-effect devices, scanning electron-beam lithography (SEBL) is used to define the fine-linewidth structures. In electron-beam lithography, a source emits electrons in a broad angular distribution. These electrons are collected and focused into a fine beam by a set of apertures and magnetic lenses. The electron beam can be scanned on a substrate using computer-controlled electrostatic or magnetic deflectors. Thus, SEBL, in principle, could be used to write any geometry pattern, and, moreover, a wide variety of patterns could be written on the same substrate. A change in pattern could be achieved easily through a change in software. In this regard, SEBL is intellectually appealing, and one could easily conclude that SEBL is a panacea for all nanolithography (sub-100-nm lithography)

applications. However, a number of problems, shortcomings, and limitations inherent in SEBL make this simplistic view, at best, incomplete, and, at worst, misleading. These shortcomings are discussed in detail in Chapter 2 of this thesis, but for now, it suffices to say that a technique complementary to SEBL is needed, and in my view, x-ray nanolithography fulfills all, or nearly all the requirements for such a complementary technology.

The goal of this thesis is the development of an x-ray mask technology for the fabrication of quantum-effect devices (and other devices where sub-100-nm patterning is required). This thesis will examine: (1) mask material considerations (organic vs. inorganic materials), (2) membrane fabrication, (3) mask patterning schemes (electron-beam and focused-ion-beam lithography), (4) absorber formation (control of absorber stress), (5) mask alignment, (6) contact and proximity x-ray lithography, including the ultimate limits on resolution due to diffraction, (7) the relationship between x-ray lithography and device performance; and (8) the fabrication of quantum-effect devices utilizing the technology developed.

In Chapter 2, nanolithography techniques such as optical-projection, holographic, scanning e-beam, and x-ray lithography are discussed, and the pros and cons of each are analyzed. In Chapter 3, the x-ray mask fabrication scheme is detailed. In this chapter, the mask patterning schemes (by e-beam and focused-ion-beam lithography) are described. Chapter 4 presents the technique we have developed for the electrodeposition of low-stress gold absorbers on x-ray masks. Chapter 5 represents our work on the replication of x-ray masks, both in the process of copying masks and replicating them onto device substrates. Chapter 6 presents results from devices fabricated using the x-ray technology developed. Two specific devices, the planar resonant-tunneling field-effect transistor and the electron waveguide are examined in detail. Chapter 7 highlights the results of the thesis as well as suggests avenues for future research in this field.

Chapter 2

Nanolithography

The work on quantum-effect devices places stringent requirements on the lithography. In order to be applicable for the work on such devices, the lithography scheme must satisfy the following set of criteria:

1. *High resolution:* – The scale of interest for quantum-effect devices is 100 nm or less. Clearly, a high-resolution patterning scheme is necessary in order to obtain such fine features. *Nanolithography* is commonly used to refer to patterning in this size domain.

2. *Compatibility with small, high-mobility substrates:* – The bulk of our work on quantum-effect devices involves III-V element systems, particularly high-mobility GaAs/AlGaAs heterojunction layers grown by molecular-beam epitaxy (MBE). The layes are typically grown on small GaAs substrates, typically only a few centimeters on a side. The grown substrate is then often cleaved into smaller pieces for processing. Any lithography scheme used must be compatible with these sized substrates. Also, with careful MBE growth, the electrons in the two-dimensional gas created at the interface of the GaAs and the AlGaAs can have extremely high mobility (higher than $10^6 cm^2/V \cdot s$). To preserve this high-mobility, the lithography or any subsequent steps should not damage the substrate.

3. *Simplicity of processing:* – The lithography should not introduce any additional unnecessary steps to the device process. Often, the limitations of a lithography scheme require the use of additional steps (e.g. intermediate resist layers, anti-reflection layers) which serve only to increase the number of process steps and decrease yield. This is clearly undesirable.

4. *Substrate independent:* – The lithography exposure conditions should be independent of substrate material. It is often necessary to expose fine patterns over different materials; for example, fine gate lines that run over AlGaAs as well as gold contacts. The exposure conditions (dose, etc.) should be the same over both materials.

In this chapter, we critically examine several lithography schemes available for fabricating devices in the scale of interest (sub-100 nm). The schemes include optical projection lithography, holographic lithography, electron-beam lithography, and x-ray lithography.

2.1   Optical Lithography

2.1.1   Optical projection lithography

Optical lithography has long been the technique used to pattern features for integrated circuits. Our research group at MIT has investigated two optical lithography schemes: high-numerical-aperture (high-NA) optical-projection lithography [8] and holographic lithography [9]. Optical projection lithography can be described as a microscope run in reverse. That is, an image is projected through an objective lens onto a sample (for instance, a resist-coated substrate).

The minimum linewidth that can be resolved by an optical system (assuming incoherent illumination) is theoretically limited by diffraction and is given by the expression:

$$p_{min} = \frac{\lambda}{2NA} \tag{2.1}$$

18

where NA is the numerical aperture of the projection lens, λ is the wavelength of the illumination, and p_{min} is the minimum resolvable spatial period. An optical microscope comes close to this minimum resolution figure. Using near-optimal conditions, 140 nm-linewidth features have been achieved with such lithography [8] using a 453 nm-wavelength lightsource and a 1.4 NA oil-immersion objective lens. However, in our work on quantum-effect devices, we need feature sizes of less than 100 nm. This is currently not possible with optical projection lithography, although one could, presumably, design a high-NA deep-uv lens to accomplish this.

Even if it becomes possible at some point in the future to design a high-NA optical-projection-lens system capable of resolving sub-100-nm- linewidth features, there still remains the problem of insufficient depth-of-focus. The depth-of-focus (DOF) of an optical system is given by the approximate expression:

$$DOF = \pm \frac{\lambda}{2n \sin^2 \theta} \qquad (2.2)$$

where θ is the maximum angle of light convergence of the lens system and n is the index of refraction of the medium between the lens and the substrate. θ is related to the numerical aperture (NA) and the index of refraction (n) by the expression

$$NA = n \sin \theta \qquad (2.3)$$

From Eq. 2.2 and Eq. 2.3, it is apparent that as the NA of the optical system is increased, the depth-of-focus decreases . For the case of reference [8] where $\lambda = 453$ nm and $NA = 1.4$, the DOF is approximately $\pm$ 180 nm. This is a fatal limitation because our substrates (small GaAs pieces) are rarely planar to within 180 nm. This is due to resist build-up at the edges of the sample, mesa etching for isolation, and thick metal interconnects. For the reasons of (1) lack of resolution, and (2) small DOF, optical projection lithography is not a viable technique for fabricating devices with sub-100-nm features.

19

2.1.2 Holographic lithography

Holographic lithography is quite capable of patterning features in the sub-100 nm domain as was demonstrated by A. Yen of our laboratory who succeeded in making gratings of 100 nm-period with 50 nm-linewidth [10] using an achromatic holographic scheme. Holographic lithography can be described simplistically as the process whereby a laser beam is broken up into two beams which are then recombined at the surface of a recording medium (namely a resist-coated wafer) to form a lateral standing-wave-intensity pattern with a period which depends on the wavelength of the laser beam and the recombination angle. While holographic lithography has sufficient resolution for our work in the sub-100-nm domain, its main drawback is that it can only produce periodic patterns (gratings and grids). For our work, we need to pattern arbitrary feature shapes; for example, pads, gate electrodes, grids, etc. This inflexibility severely limits the applicability of holographic lithography.

2.1.3 Standing waves

In addition to the drawbacks for optical projection (insufficient resolution and depth-of-focus) and holographic lithography (only periodic patterns like grids and gratings) that we have discussed in the previous two sections, both holographic lithography and optical projection lithography also suffer from index mismatching at the resist/substrate interface. At the uv wavelengths most commonly used for holographic and optical projection lithography, the index of the substrate (e.g. GaAs or Si) can differ considerably from that of the resist. Table 2.1.3 compares the components of the complex index of refraction:

$$N = n + ik \tag{2.4}$$

for PMMA (polymer resist), polyimide, Si, and GaAs at λ=193 nm. This index mismatch leads to reflections off the substrate, and, hence, standing waves in the intensity as a function of depth into the resist. This standing-wave effect leads to an uneven resist development rate and is undesirable. The effect of the standing waves

Material	n	k
PMMA	1.68	0
polyimide	1.33	0.52
Si	0.88	2.77
GaAs	2.5	0.5

Table 2.1: Real and imaginary components of the index of refraction at $\lambda = 193$ nm for PMMA, polyimide, Si, and GaAs

can be reduced by introducing an anti-reflection layer between the substrate and the resist. However, the addition of this intermediate layer adds several steps to the processing. This is generally undesirable for the reasons discussed at the beginning of the chapter.

2.2 Electron-Beam Lithography

An electron-beam (e-beam) lithography system can be described simplistically as an accelerated beam of electrons focused to a small diameter by a series of magnetic lenses. This beam of electrons can be scanned using magnetic deflectors controlled by a computer. By putting a resist-coated substrate on a motorized x-y stage, energetic electrons can be deposited at specified points on the wafer, thereby exposing the resist. Patterns of arbitrary geometry can thus be "written" onto the substrate. This technique of using e-beam lithography to pattern directly onto the substrate of interest is called "direct-write" e-beam lithography.

The resolution limit of an e-beam lithography system is a function of the beam diameter and the degree to which the electron beam interacts with the resist and substrate. The intrinsic beam diameter d_o of an e-beam system is given by

$$d_o = \left(\frac{4i}{\pi^2 B} \right)^{1/2} \alpha^{-1} \tag{2.5}$$

where i is the beam current, B is the source brightness, and α is the convergence angle. This intrinsic beam diameter is degraded by the effects of spherical aberration,

chromatic aberration, and diffraction. The degradation of the intrinsic beam diameter can be taken into account by adding the degradation effects to the intrinsic beam diameter in quadrature. Specifically,

$$d_{tot}^2 = d_o^2 + d_s^2 + d_c^2 + d_f^2 \qquad (2.6)$$

where d_{tot} is the beam diameter obtained when the effects of spherical aberration (d_s), chromatic aberration (d_c), and diffraction (d_f) are added to the intrinsic beam diameter (d_o).

The interaction of the electron beam with the substrate can be described by a point exposure distribution (the distribution of energy dissipated in the resist by electrons forward-scattered in passing through the resist and backscattered from the substrate). As the name implies, the point-exposure distribution assumes a input electron beam of zero width (i.e. a delta function input). Chang modeled the point-exposure distribution as the sum of two Gaussian terms and showed that it could be empirically fitted to experimental data [11]. This equation can be written as

$$f(r) = \frac{1}{\pi(1 + \eta_E)} \left[\frac{1}{\beta_f^2} exp \left(-\frac{r^2}{\beta_f^2} \right) + \frac{\eta_E}{\beta_b^2} exp \left(-\frac{r^2}{\beta_b^2} \right) \right] \qquad (2.7)$$

where r is the lateral distance from the incident beam, β_f and β_b are the characteristic lengths of lateral influence due to forward-scattered and backscattered electrons, respectively, and η_E is the ratio of the volume integrated exposure by the backscattered electrons to that by the forward scattered electrons.

Given an incident dose distribution $D(\mathbf{r})$, a deposited energy distribution in the resist $E(\mathbf{r})$ is obtained by convolving it with the point exposure distribution $f(\mathbf{r})$

$$E(\mathbf{r}) = k \int D(\mathbf{r})f(\mathbf{r} - \mathbf{r}')d^2\mathbf{r}' \qquad (2.8)$$

Fig. 2-1 shows the effect of convolving an ideal dose distribution (step function) with the point-exposure distribution of the form of Eq. 2.7 to obtain the deposited energy distribution. Two observations can be made from the results depicted schematically

Point-exposure distribution

f(r)

0   x

$\otimes$

Dose distribution

D(r)

0   x

=

E(r)   Energy distribution

0   x
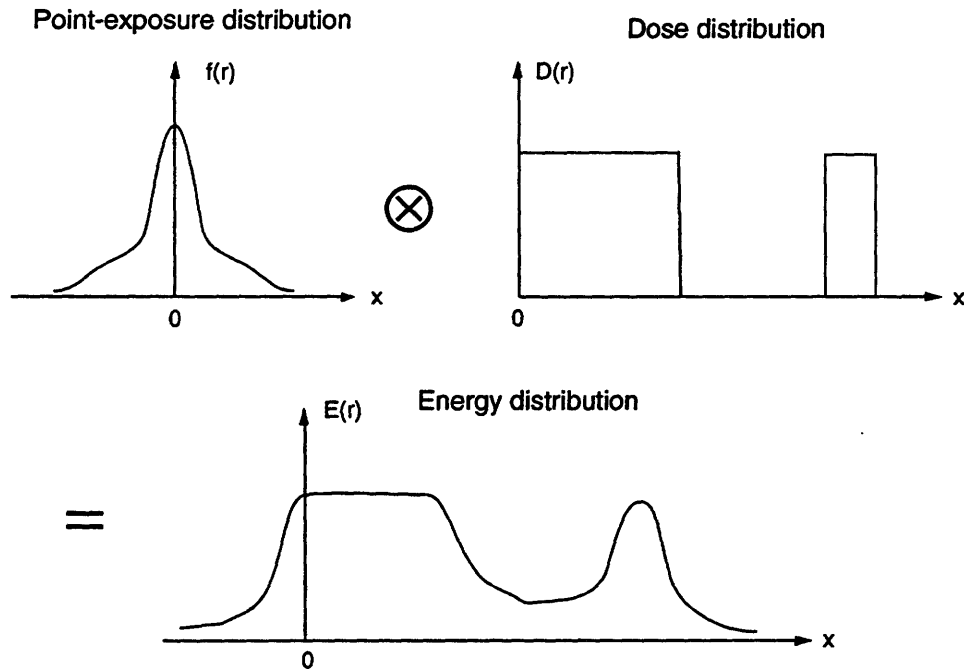
Figure 2-1: Schematic showing the convolution of the point-exposure function with the dose distribution to obtain the exposure-energy distribution. Note that the contrast is reduced due to electron scattering.

in Fig 2-1: (1) the contrast of the energy distribution is greatly reduced relative to that of the dose distribution due to the effect of electron scattering (incorporated into Eq. 2.7), and (2) two patterns in close proximity to one another can have significantly different energy distributions than if the two identical patterns were widely separated, i.e. the so-called *proximity effect.*

As we can see from Fig. 2-1, the effect of electron scattering is to reduce the contrast of the exposure by introducing a background level. Lower contrast in the lithography means that pattern linewidth is extremely dependent on resist development parameters such development time, temperature, and concentration. Because pattern linewidth is so dependent upon these development parameters , we say that e-beam lithography has a low *process latitude*, that is, a low tolerance for variations in processing parameters. This is a clear disadvantage of e-beam lithography.

The proximity effect tells us that the dose required to expose a certain feature depends upon whether there are other exposed features in the vicinity. For example,

to properly expose a 100 nm-wide line in an isolated field requires more dose than to expose the identical feature if it is within close proximity (less than or comparable to the characteristic lengths β_f or β_b) to a large pad, since the energy deposited in the region of the pad affects the background exposure level at the line. Computer programs have been written to correct for such differences in required dose due to pattern geometry and arrangement [12]. However, such programs require very large computational power. In addition, proximity correction software cannot correct for the cases where the pattern lies partially over one substrate type (for instance, GaAs) and partially over another type (e.g. Au). This is a severe drawback of e-beam lithography because it is often necessary to pattern fine features over two or more substrate types.

2.3 X-ray Lithography

X-ray lithography has been proven experimentally to have resolution considerably below the dimensions needed for the study of quantum-effect devices (100 nm and below). Chapter 5 will go into more detail on the resolution limits of x-ray lithography. Flanders had shown in 1980 that 17.5 nm line-and-space patterns could be replicated using 4.5 nm-wavelength x-rays [13]. In 1988, experiments by Early *et al.* [14] showed that absorber patterns of only 30 nm linewidth on a mask can be faithfully replicated in PMMA resist at the wavelengths 0.83, 1.32, and 4.5 nm (wavelengths which lie within the range commonly used for x-ray lithography). The micrographs of the exposures are shown in Fig. 2-2. Such experimental evidence suggests that x-ray lithography has more than sufficient resolution for the device dimensions we are concerned with.

X-ray lithography, unlike e-beam lithography, has a large process latitude. Exposure conditions are independent of the type of substrate used. Unlike e-beam lithography, there is no proximity effect. For example, a fine line close to a pad will get the same exposure as one in an empty field. If a reasonably high-contrast absorber is used (say 10 dB attenuators), then the x-ray exposure is capable of very high process
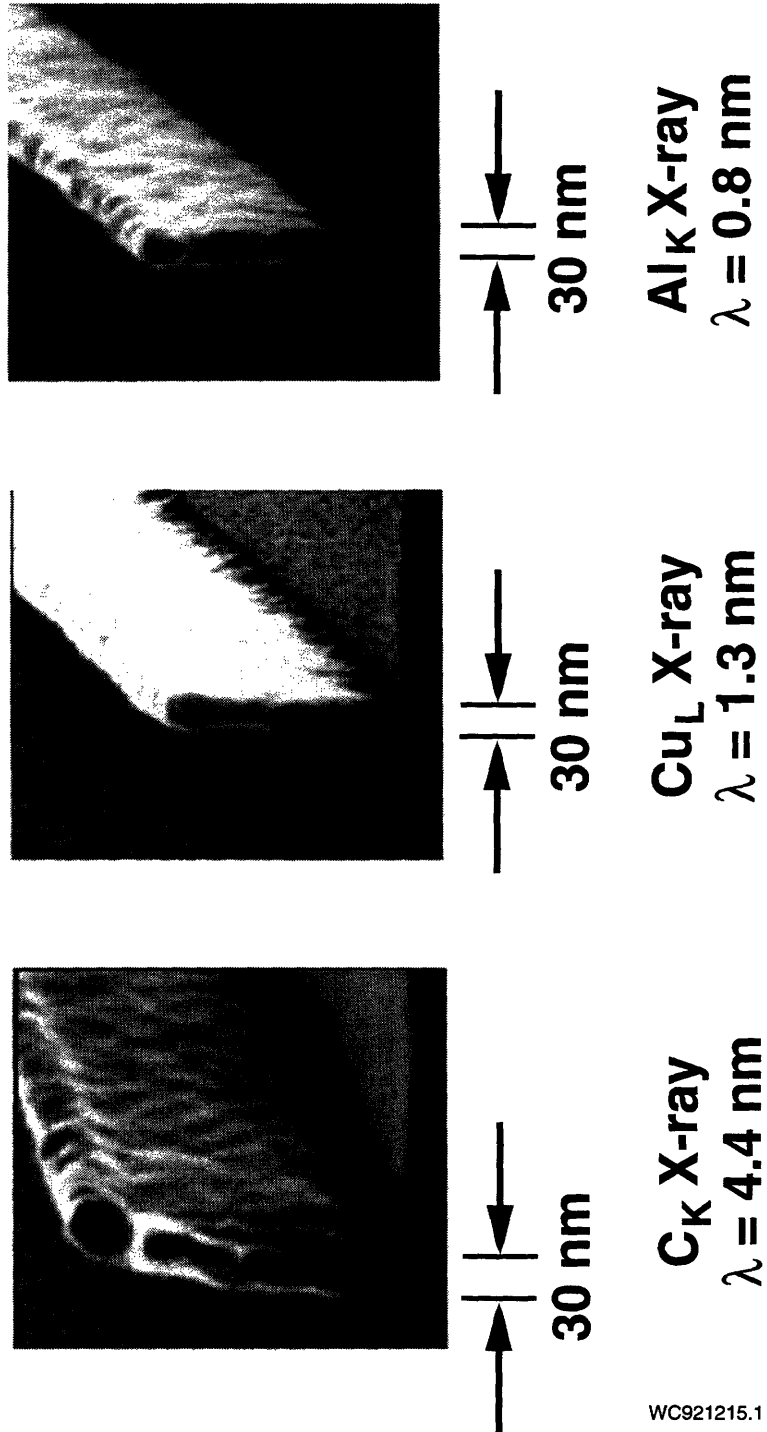
Figure 2-2: Replication of 30 nm-linewidth structures in PMMA with C_K ($\lambda = 4.4$ nm), (b) Cu_L ($\lambda = 1.3$ nm), and (c) Al_K ($\lambda = 0.83$ nm) x-rays. From Early, ref. [1].

latitude and can tolerate large amounts of development process variation with little linewidth variation.

X-ray lithography, unlike optical lithography does not require any anti-reflection coating on the substrate. At the wavelength range used for x-ray lithography (0.8 to 4.5 nm), the index of refraction of both PMMA and the substrate are roughly equal to 1.0. That is, the real part of the complex index, $n \approx 1.0$ while the imaginary part, $k \approx 0$. Since the materials are index-matched, no standing waves occur in the resist.

It has also been determined that x-ray lithography does not damage high-mobility substrates [15]. There is evidence that energetic electrons (like those present in e-beam lithography or e-beam evaporator systems) impinging on high mobility substrates can cause mobility degradation. The mechanism for the e-beam damage is not yet known. This is a significant argument for the use of x-ray lithography rather than direct-write e-beam lithography to make quantum-effect devices because observation of electron quantum effects often depends upon having a high-mobility substrate, undamaged by any of the processing steps.

The discussion in this section points to all the advantages of x-ray lithography; namely large process latitude, substrate independence, no anti-reflection or any other intermediate layers needed, no damage to high-mobility substrates, and high resolution. In order to apply all of these advantages, we must develop an x-ray mask technology which is capable of exposing the devices of interest in the sub-100-nm regime. The next chapter describes the development of this mask technology.

Chapter 3

X-ray Mask Fabrication

In order to expose the critical features on device substrates, we must have an x-ray mask that contains those features. For proximity x-ray lithography, the features on the mask must be identical to those that we desire on the substrate. That is, there is no magnification involved. This requires advanced lithographic techniques to define fine (sub 100 nm) features onto an x-ray mask blank.

3.1   Membrane Material

In order to have an x-ray mask which is suitable for work in the sub-100 nm domain and can be used in a multi-level lithography process, the mask material must satisfy an important set of criteria. The masks must be:

1. *x-ray transmissive* – This usually restricts the mask material to be a membrane of roughly 1 - 2 μm thickness in the x-ray regime in which we operate ($\lambda > 1$ nm).

2. *dimensionally stable* – This is important because the membrane will ultimately be patterned, and the pattern fidelity must be maintained throughout the processing and subsequent exposures.

3. *strong* – The membrane must be robust enough to withstand normal processing such as resist spinning, nitrogen gas blowing, etc.

4. *optically flat* – The gap between the mask and the substrate must be maintained to a high accuracy (to a small fraction of the gap itself, which can be as small as a few microns). Such fine control of the gap requires a flat membrane.

5. *radiation hard* – These membranes will ultimately be exposed to large doses of x radiation. Their properties must remain unchanged after extensive irradiation.

6. *optically transparent* – The masks will be aligned to patterns on a substrate using optical (400 - 900 nm) techniques. The membrane needs to be transparent in that regime so that the pattern can be seen through the mask.

In the past, we have used polyimide membranes with gold and tungsten absorbers as our x-ray masks [16, 17]. However, these membranes do not meet the second criterion listed above. After repeated use, the membranes become severely wrinkled. Also, breakage was common. For these reason, and many others, the polyimide masks are incompatible with the fabrication of devices and circuits which require multilevel alignment.

It is clear that a membrane of an inorganic material is necessary to satisfy all the requirements listed. In the wavelength of interest, membranes of Si, silicon-nitride, SiC, polysilicon, etc. of 1 - 2 μm thickness are sufficiently x-ray transmissive. Films of these materials can be deposited at fairly low stress if the deposition conditions are controlled properly. The properties of a few sample membranes etched from some of these materials are listed in Table 3.1 [2].

From the table, it is readily apparent that silicon-nitride films have all the properties desirable for an x-ray mask material. The data shows that membranes etched from nitride films deposited at MIT and University of California Berkeley (UCB) have high burst pressure, high optical transparency, and are radiation hard. In fact, the nitride membranes have the highest burst strength and strength figure-of-merit of all the membranes tested. In addition, nitride films can be deposited at relatively low temperatures (700 - 800°C) in commercially-available deposition systems. If the temperature is kept within this range, and if the flow rate ratio of dichlorosilane to ammonia is in the range between 5:1 and 7:1, low-stress silicon-rich nitride (hereafter

28

Membrane Material (d) (Test dia., D, 20 mm)	(a) Break Point (atm) P_{bp}	thickness (μm) t	(b) max. deflect. (μm) h_{bp}	(c) Typical Stress (dyn/cm^2) x10^9 σ_m (meas.)	Bulk Modulus (dyn/cm^2) x 10^{12}	(d) FOM (atm) x 10^5	Optical Trans. T @ 633 nm (%)	x-ray rad. dose J/cm^2 ---- ($\Delta\sigma$)
Nitride (UCB)	> 1.0	2	930	0.6-1.5	1.5 - 1.9	> 2.2	58.1	8400 (< 2%)
Nitride (MIT-ICL)	> 1.0	2	1057	3 - 4	1.0	> 1.9	63.6	
Epi-Si (Source 1, SF)		1		0.9-1.4		1.3	43.4	9800 (0%)
Epi-Si (Source 1, NSF)	0.08	1	456	1.1-1.4	2.0	0.70	40.3 - 47	
Poly Si (Source 2)	0.33	1	2288			0.58	17	
SiC (Source 3)	0.13	1.3	540			0.74		
SiC (Source 4)	0.06	0.86	404	1.2	2.4	0.69		
Nitride/Poly/ Nitride (MIT)	0.97	1.2	1705			1.9		
Nitride/Oxide/ Nitride (MIT)	0.50	1.5	611			2.2		

(a) & (b) The burst pressure and the maximum deflection height were measured using the bulge tester with the membrane touching the sealing o-ring.

(c) The stress and bulk modulus were measured using the bulge tester with the supporting rim (typically the Si wafer) placed in contact with the sealing o-ring.

(d) The test diameter (20 mm) refers to the diameter of the sealing o-ring used in the burst test measurement, and not the actual membrane size.

$$\text{FOM} = P_{bp}\left(\frac{D^2}{t h_{bp}}\right)$$

SF = stacking faults

Table 3.1: Properties of various membrane materials. From ref. [2].

denoted as SiN_x) films can be deposited [18]. The SiN_x films from MIT and UCB were deposited in low-pressure chemical vapor deposition (LPCVD) furnaces also used for the deposition of stoichiometric nitride films for MOS device fabrication. For these reasons, we believe that SiN_x membranes meet all the requirements for our research applications, and the work described in this thesis will involve masks made with SiN_x membranes exclusively. It should be noted, however, that the properties of the various membrane materials listed in Table 3.1 are not complete, nor definitive, but are shown to indicate trends. There is considerable interest in SiC – both amorphous [19] and polycrystalline [20] – and diamond [20] as membrane material for x-ray masks. A comparative study of SiN_x versus these material is not available at this time.

3.2   Mask Blank Fabrication

The mask blank is a mesa-etched structure shown schematically in Fig. 3-1. [21]. The SiN_x membrane and rim are collectively known as the "mesa." The mesa is formed by etching back the Si substrate, leaving only a narrow rim to support the membrane. The advantage of this structure is that the mask can be brought into close proximity with a substrate during lithography without the risk of collision between them. Also, any dust particle outside the mesa area, either on the mask or the substrate will not interfere with a small gap setting.

The mask blank fabrication sequence is shown schematically in Fig. 3-2. The fabrication begins with a 100 mm-diameter Si wafer coated with a 1 - 2 μm-thick SiN_x film deposited by a Si-rich LPCVD process. The nitride is etched off the back of the wafer using CF_4 reactive-ion-etching (RIE). The wafer is then cleaved into four quarters and cleaned. The side of the quartered wafer which had the nitride removed is then anodically bonded to an optically- flat Pyrex ring. The Pyrex ring provides rigidity and also serves as a mask for KOH etching. The membrane is formed by KOH etching the Si substrate. Since the wafers are bonded to an optically flat surface, the resulting membrane is itself extremely flat. The flatness of the mesa has been measured using a HeNe ($\lambda = 632.8$ nm) Fizeau interferometer, and has

Mask for Soft X-ray
Nanolithography (λ = 1.3 nm)
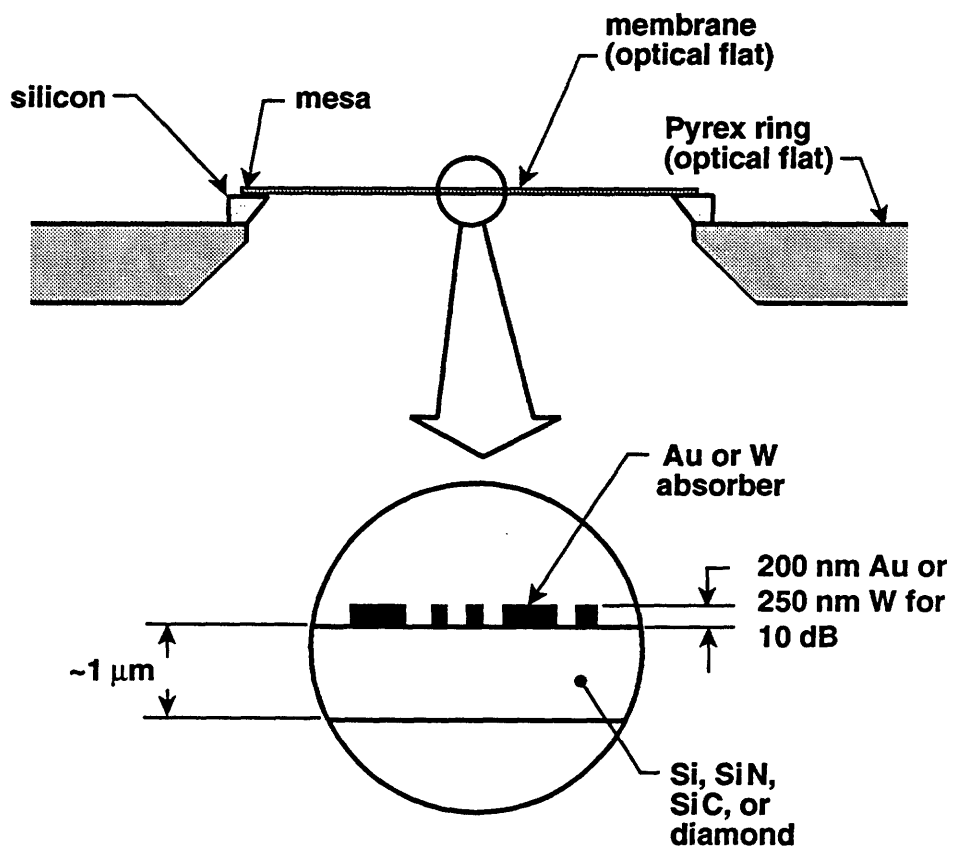
WC920929.1

Figure 3-1: Schematic of typical x-ray mask.

MASK FABRICATION PROCESS

SILICON NITRIDE

SILICON WAFER

1) COAT WITH LOW-STRESS LPCVD NITRIDE

FRONTSIDE

BACKSIDE

2) BACKSIDE RIE ETCH

3) QUARTER WAFER

4) ANODICALLY BOND TO OPTICALLY-FLAT PYREX RING

5) FRONTSIDE MESA STENCIL-RIE ETCH

6) BACKSIDE KOH ETCH-THROUGH AND FRONTSIDE MESA ETCH

7) FRONTSIDE OVERHANG STENCIL-RIE ETCH

8) PATTERN ABSORBER
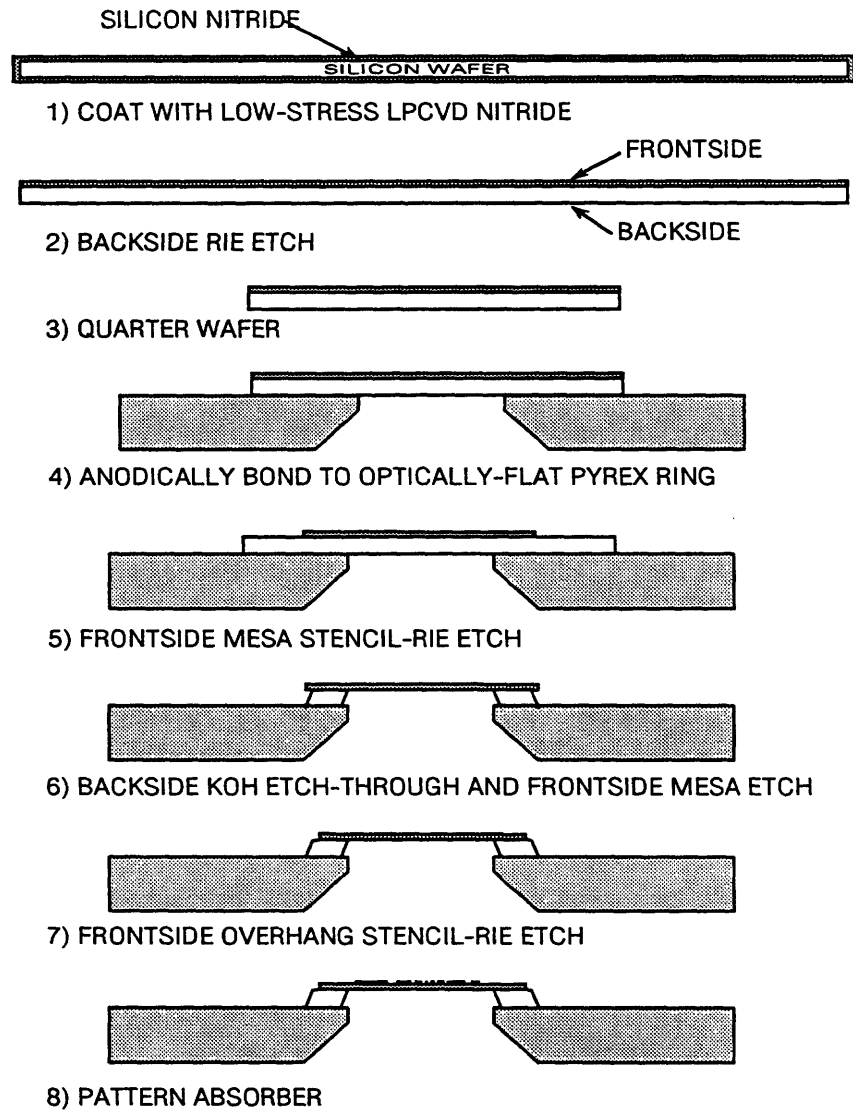
WC921222.2

Figure 3-2: Mask blank fabrication sequence.

been determined to be flat to within 0.25 μm overall, and to better than 0.1 μm in the central 2 cm diameter of the mask membrane [21]. Following the membrane formation, a nitride overhang RIE etch is necessary to remove any nitride which may be hanging off the edge of the mesa. A finished mask blank is shown in Fig. 3-3

After the etching steps are completed, the membranes need to be cleaned again. A careful clean is essential here as contamination on the membrane can result in poor adhesion of the plating base to the SiN_x. The mask blanks are cleaned using "piranha" etch (3:1 H_2SO_4: H_2O_2), followed by "RCA" organic clean (5:1:1 H_2O: NH_4OH: H_2O_2), and a rinse in DI water. After blow-drying the membranes, a plating base of 5 nm NiCr and 10 nm Au is e-beam evaporated followed, in the same pump-down, by a 200 nm-thick Au evaporation which covers the entire sample except for the membrane area in the center (see Fig. 3-4). The thickness of the plating base is an important factor in determining the fraction of electrons that backscatter into the resist during e-beam patterning [22]. The plating base should be as thin as possible while maintaining electrical continuity throughout the processing. The thick Au outside the membrane area lowers the electrical resistance and provides a good electrical contact on the Pyrex area.

Immediately after the plating base evaporation, we spin on PMMA to the thickness required for our process. It is critical that the PMMA be spun on immediately after the masks come out of the evaporator since contamination that accumulates on the plating base can cause resist adhesion problems when the resist is developed after exposure. The molecular weight and thickness of the PMMA needed depends on the application. For example, on the masks exposed using focused-ion-beam lithography (FIBL) at MIT and electron-beam (e-beam) lithography at NRL we used 950 K mol. wt. PMMA of 0.3 μm thickness, while for the electron-beam lithography exposure at IBM, we used 496 K mol. wt. PMMA at a thickness of 0.25 μm.

The PMMA is spun to the desired thickness using a spin chuck specially designed for handling the Pyrex-bonded masks. The PMMA, prefiltered by the manufacturer, is stored in RCA-cleaned, capped, Erlenmeyer flasks. A spin curve is determined for each flask by spinning monitor wafers at different speeds, baking them, and measuring

SiN$_x$ X-ray Mask
(Membrane 31 mm diam.)
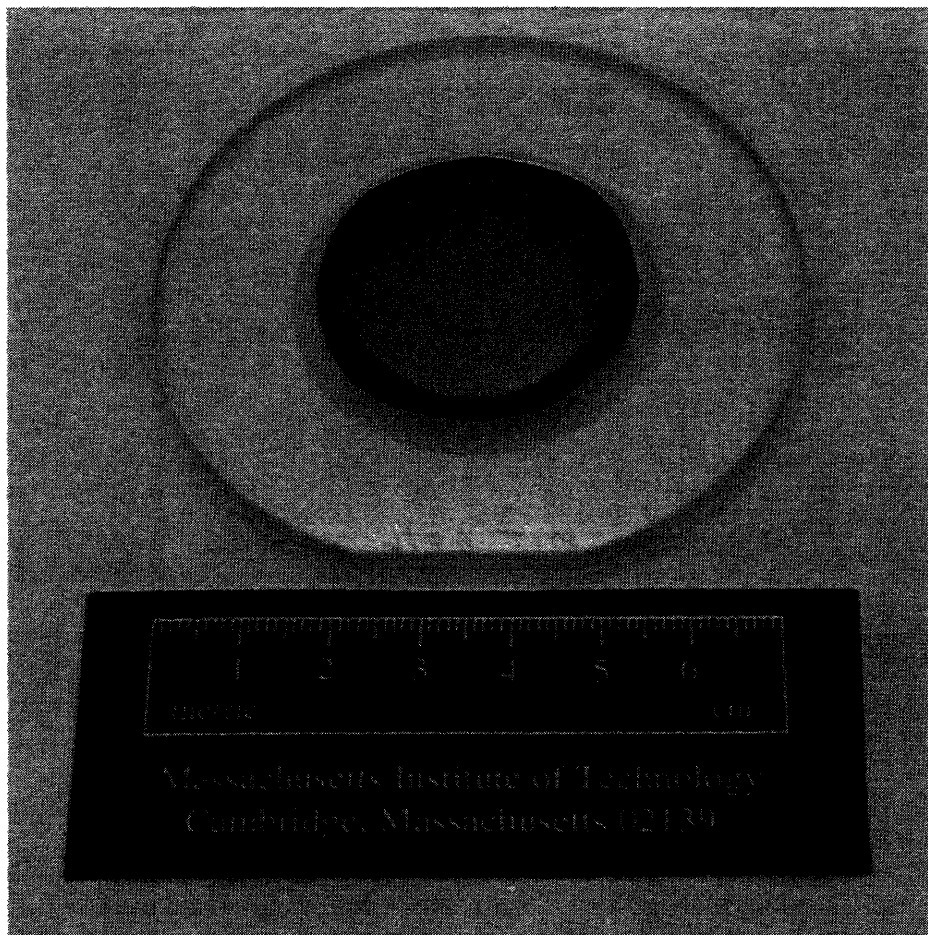
WC921222.1

Figure 3-3: SiN$_x$ x-ray mask blank with 31 mm diameter membrane.

1) 1st evaporation: 5 nm NiCr / 10 nm Au (plating base)
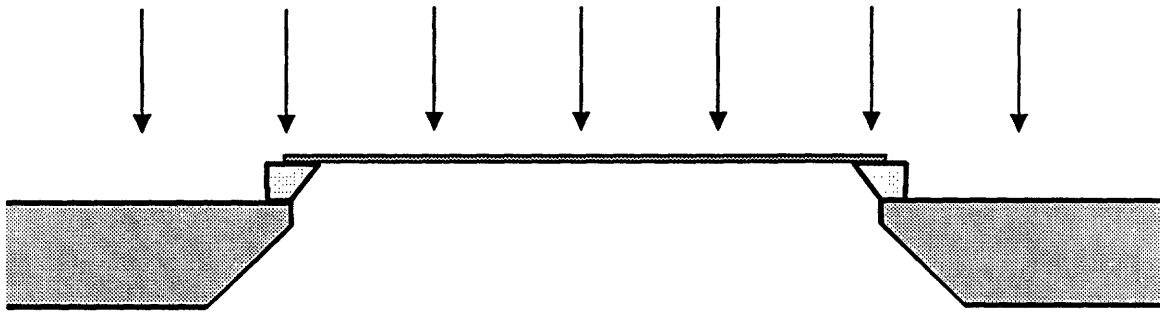
2) 2nd evaporation: 200 nm Au

cover "hat"
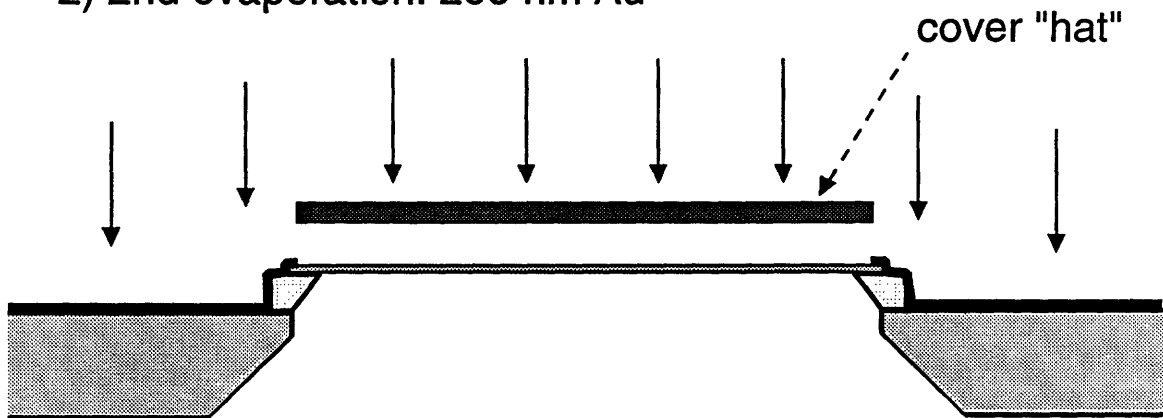
Figure 3-4: Double evaporation scheme for depositing plating base and thick-Au contact metal. A thin plating base (5 nm NiCr followed by 10 nm Au) is e-beam evaporated first and then followed, in the same pumpdown, by an evaporation of 200 nm of Au. The membrane area is covered in the second evaporation by a "hat" which prevents the thick Au from being evaporated onto the membrane.

the thickness of the resist by scratching the film with a metal tip and scanning the surface across the scratch using a profilometer. After determining the spin speed necessary to obtain the desired resist thickness, PMMA is spun onto the mask. With the flat of the Pyrex ring down (at 180°), we then clean off PMMA in four small spots at diametrically-opposed positions on the mesa (at 0°, 90°, 180°, and 270°) using a chlorobenzene (or acetone)-soaked q-tip. The 200 nm-thick Au is then scratched with a metal pin (not a diamond-tip scribe as this scratches the Si and leaves particles on the sample). The mask blank is then baked at 180°C for one hour. Longer bake times can result in bad plating results due to NiCr diffusing into the Au and, presumably, oxidizing. After allowing the mask blanks to cool, they are stored in individual mask carriers.

3.3   Mask Exposure

We have used a number of techniques for patterning the absorbers including ultraviolet (UV) contact lithography, holographic lithography [23], focused-ion-beam lithography (FIBL) [24] and scanning electron-beam lithography (SEBL) [25, 26]. These patterning techniques are usually followed by etching of tungsten or electroplating of Au in order to form the absorber pattern. In this section, I will describe our work on FIBL and SEBL and in the next chapter, I will describe our results on low-stress Au plating.

3.3.1   Focused-Ion-Beam Lithography

Focused-ion-beam systems can be readily utilized as high-resolution lithography tools [27, 28]. Because of the their larger mass, ions scatter much less than electrons. The implication for lithography is that there is negligible ion scattering in the imaging resist and low backscattering from the substrate [29] and as a result, there is no proximity effect, as there is in e-beam lithography. In contrast to electrons, ions also generate only low-energy secondary electrons [27]. Structures defined by focused-ion-beam lithography (FIBL) are thus limited only by the secondary electron range

and lateral straggle of ions in the resist which are both considerably smaller than the scattering ranges for electrons in e-beam lithography. The rest of this section describes our work to expose x-ray masks with 50 nm line-and-space patterns using FIBL for the PRESTFET project.

Our original motivation was to avoid a tri-level resist process commonly used when e-beam lithography is utilized to make x-ray masks [30]. (The tri-level process and the problems it introduces are discussed in the next section on using e-beam lithography to write x-ray masks.) A desirable alternative was to have a process where a single resist layer was used, and where the developed resist pattern has sharp, vertical sidewalls suitable for use as a mold for Au-absorber electroplating. Since the proximity effect is all but absent in FIBL, and the range of heavy ions in thick resist can be quite large at high accelerating energies, we decided to explore the possibility of using the single-resist-layer process and FIBL to expose 50 nm interdigitated lines on our x-ray masks.

The process used to fabricate the masks is shown schematically in Fig. 3-5. The FIBL was done at 280 keV with Be^{++} ions from a Au-Si-Be alloy source. The FIBL scan field was 164 × 164 μm and the beam current was 20 pA (doubly charged ions). The mask blank used is similar to those described in Sec. 3.2; the PMMA used was 950 K molecular weight spun on to a thickness of 300 nm. The plating base was 5 nm NiCr and 10 nm Au. The linear charge density needed to properly expose a film of this thickness was roughly 10^{-11} C/cm. At 280 keV, the accelerated Be^{++} ions penetrated completely through the PMMA, enabling a clean vertical sidewall structure to be developed down to the plating base. Electroplating yielded 250 nm-thick (12.5 dB contrast at 1.32 nm wavelength) structures in Au. A top view of a feature on the finished x-ray mask is shown in Fig. 3-6. The complete process is very high yield. The lines are generally well-formed and do not widen as they approach the pad which indicates a lack of proximity effect.

In addition to this lack of proximity effect, writing time for FIBL is much shorter than that necessary to expose the same pattern in e-beam because PMMA, and most

Focused-Ion-Beam Lithography and Electroplating

FIB (Be^{++})

PMMA

Au plating base

Develop & Plate Au

Dissolve PMMA

50 nm
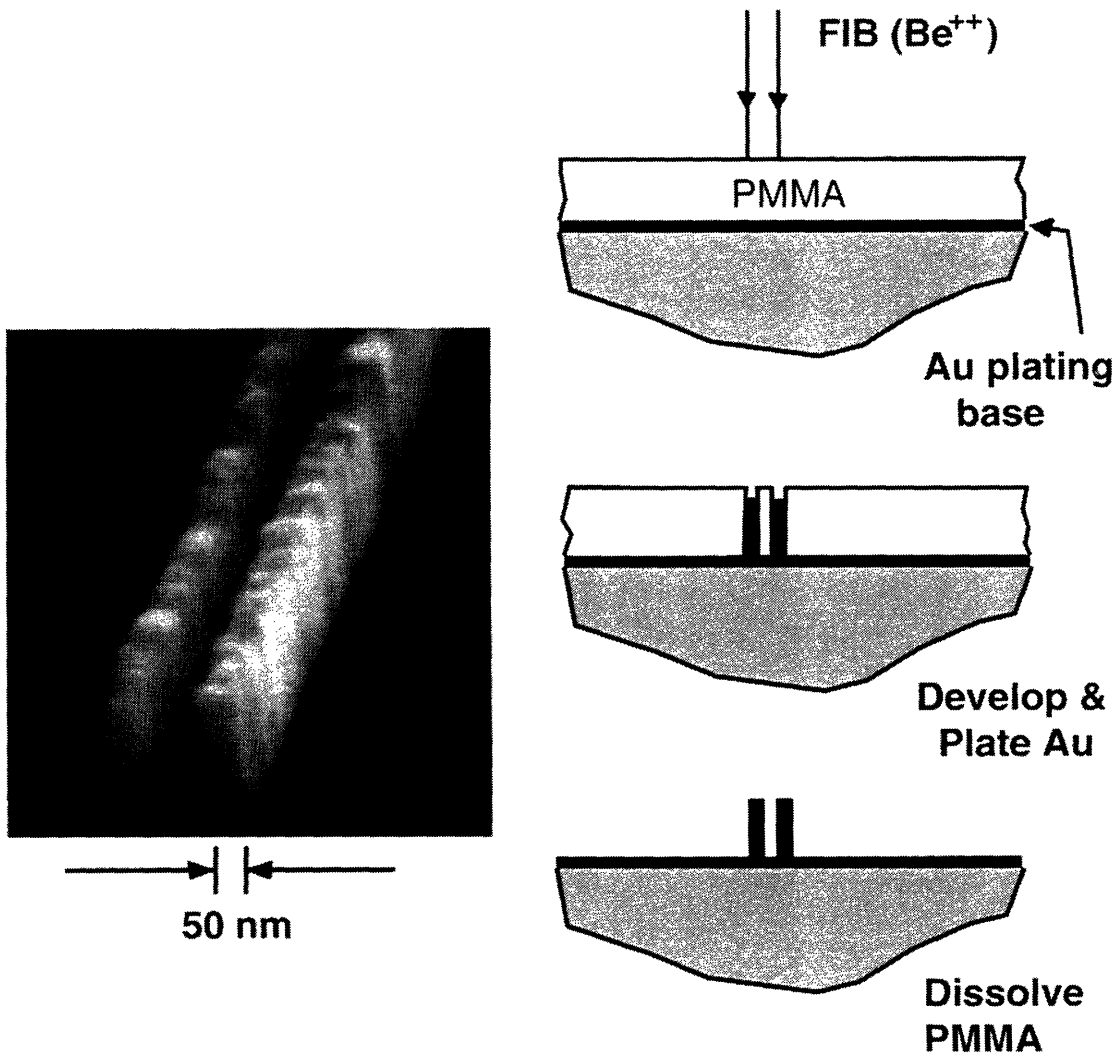
WC930204.1

Figure 3-5: Schematic of x-ray mask patterning using Be^{++} focused-ion-beam lithography (FIBL). The developed resist profile is sharp and vertical as witnessed by the vertical sidewalls of the plated Au in the micrograph to the left.
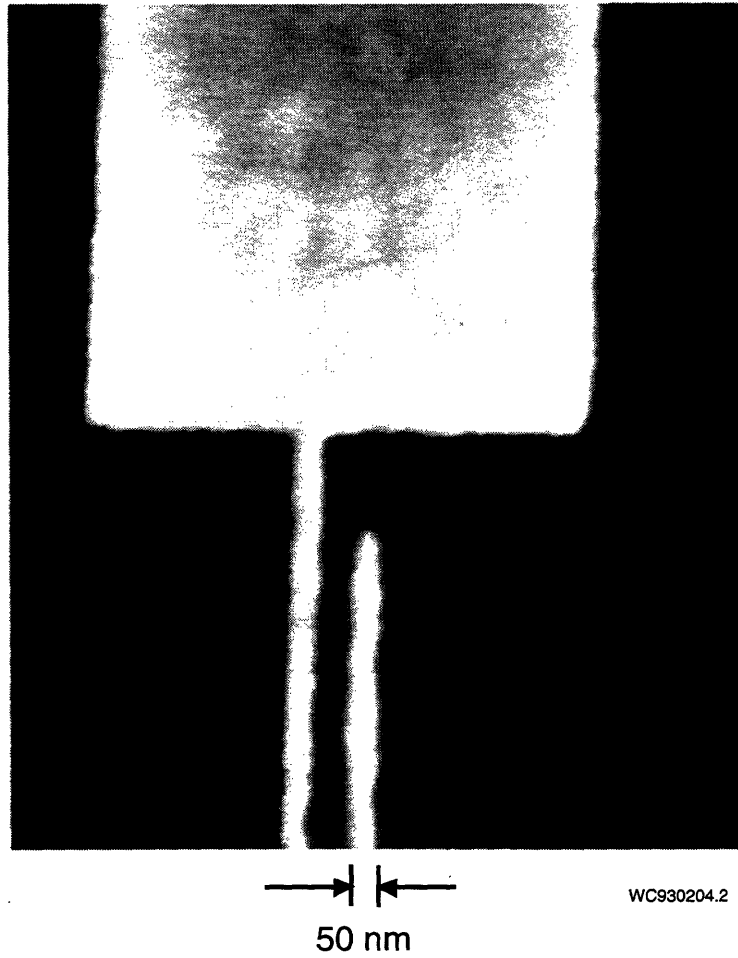
50 nm

Figure 3-6: Scanning-electron micrograph (top view) of a of a 50 nm-linewidth pattern (PRESTFET) made using 280 keV Be^{++} focused-ion-beam lithography and Au electroplating.

other organic resists, are more sensitive to ions than electrons [27]. For example, for the 300 nm PMMA that we use, the linear charge densities for full exposure of the 50 nm line for ions and electrons are $\sim 10^{-11}$ and 2×10^{-9} C/cm, respectively. The lower number for ions – corresponding to roughly 30 ions per 10×10 nm pixel – is due to the fact that ions lose more energy than electrons do in passing through a resist film due to their significantly larger scattering cross-section.

While FIBL has proven to be a valuable tool for writing fine features on x-ray masks, there are some points at which improvements and more study are necessary. The alloyed ion sources have a short lifetime, to the extent that the condition of the source can fluctuate between runs and even during a run. This is perhaps due to the interaction of the molten alloy with its holder needle, or with the background gas due to poor vacuum, resulting in a change in the composition of the alloy [31]. Advances in source technology are occurring constantly, so that the outlook for this problem is optimistic. In addition, electromagnetic shielding is absolutely critical in minimizing noise in the column. The line-edge raggedness of the interdigitated fingers of Fig. 3-6 can be attributed to either insufficient shielding or shot noise due to the relatively small number of ions needed to expose a 50 nm $\times$ 50 nm box . The statistical fluctuation in this small number of incident ions can create variations in exposure level along a line [1]. As a result, line-edge-raggedness may arise. Nevertheless, the results of the exposures shown in Fig. 3-6 show that FIBL is a viable method for patterning x-ray masks with feature sizes as small as 50 nm.

3.3.2   Electron-Beam Lithography

We have also used e-beam lithography to pattern x-ray masks. For our work on quantum-effect devices, such as the PRESTFET, we need mask patterns with 50 nm line-and-space features. Since our x-ray source uses the Cu_L line (($\lambda = 1.3$ nm), in order to get a 10 dB attenuation at this wavelength, we need a 200 nm-thick Au film (see Fig. 3-7). If we wished to use the exposed and developed PMMA resist as a mold, this would require an exposure which yields a 50 nm-linewidth, 250 nm-thick PMMA line (5-to-1 height-to-width ratio) with vertical sidewalls. This was possible

40

with focused-ion-beam lithography because the ions used were massive, and thus traveled through the resist and well into the substrate without scattering. As a result, exposures with FIBL have high contrast. With e-beam lithography, on the other hand, the electrons are light and scatter easily. The point-exposure distribution (Chang double-Gaussian) of Eq. 2.7 describes the interaction of the incident electrons with the resist and substrate. The long range scattering, predominantly due to backscattering (the second Gaussian term in Eq. 2.7), serves to lower the contrast of the exposure. Consequently, for a pattern of 50 nm line-and-space exposed at beam accelerating voltage of 25 kV, resist thickness cannot be much greater than 100 nm; otherwise the unexposed resist line develops away before the exposed area fully develops out. This is insufficient resist thickness to be used directly as a mold for electroplating the absorbers since the Au thickness needed (200 nm) would exceed the height of the mold (100 nm). To circumvent this problem others have used a tri-level process depicted schematically in Fig. 3-8 whereby thin resist is e-beam exposed and used as a mask for reactive-ion-etching a thin metal layer, which is then itself used as a mask for etching a thick organic film (typically polyimide or resist) which will ultimately be used as a mold for electroplating [30]. This tri-level scheme has a narrow process window because the two critical dry etching steps have to be performed without undercutting the mold.

An alternative and simpler scheme is to use high-voltage e-beam lithography to expose onto thick resist (> 250 nm thick) and to use the resist as a mold for electroplating. In Eq. 2.7 reproduced below,

$$f(r) = \frac{1}{\pi(1 + \eta_E)} \left[\frac{1}{\beta_f^2} exp\left(-\frac{r^2}{\beta_f^2}\right) + \frac{\eta_E}{\beta_b^2} exp\left(-\frac{r^2}{\beta_b^2}\right) \right]$$

it is well known that β_f decreases and β_b increases as the electron energy is increased [12]. This occurs because the higher the kinetic energy of the incident electron, the smaller the differential scattering cross section for high-angle scattering. This is
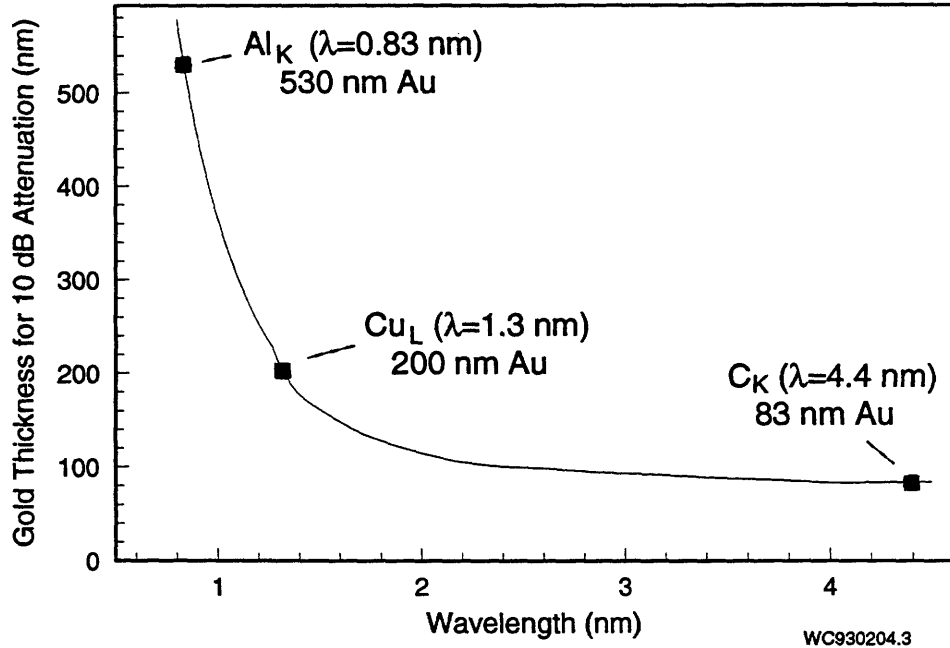
Figure 3-7: Thickness of Au needed for 10 dB attenuation as a function of x-ray wavelength. Thickness values are given for three x-ray lines.

evident in the equation for the Rutherford-scattering cross section [32]

$$\sigma(\Theta) \propto \frac{1}{E^2} \csc^4\left(\frac{\Theta}{2}\right) \tag{3.1}$$

where E is the incident electron kinetic energy, Θ is the angle at which the electron is scattered (relative to its original trajectory), and $\sigma(\Theta)$ is the differential scattering cross section. Eq. 3.1 shows that for high energy electrons, the differential scattering cross section is large only near $\Theta = 0$. This means that high-energy electrons scatter predominantly at low angles (near $\Theta = 0$), resulting in a smaller beam spread (β_f).

At high energies, backscattered electrons from the substrate can travel farther from their point of entry in the resist, thus leading to a larger backscattering range, β_b. On solid silicon, for example, β_b is 2.8 μm at 25 keV and 8.8 μm at 50 keV [33]. However, if the substrate is a thin membrane, like those that we use for x-ray masks, it is well known that at high accelerating energies η_E is substantially reduced relative to a solid substrate, thus substantially reducing the second Gaussian term, and thus, reducing the background exposure level [22]. This makes physical sense because η_E is

PMMA (80 nm) — Ti (7.5 nm)

Polyimide (200 nm)

— Au (10 nm)
— Membrane (1-2 μm)

E-beam
exposed

RIE Ti (CCl_2F_2)
and
RIE polyimide (O_2)

Electroplate Au
and
Strip polyimide
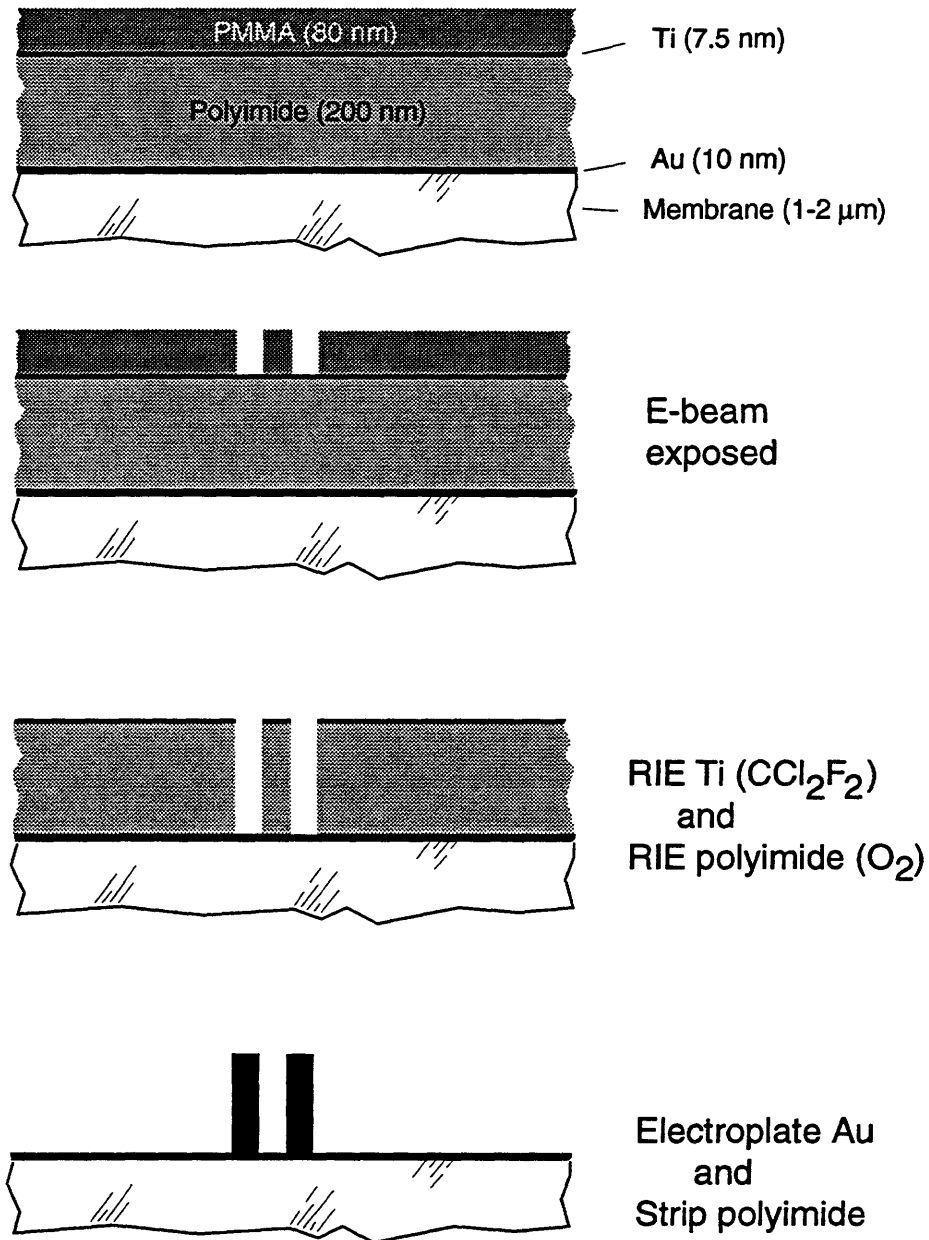
Figure 3-8: Schematic of tri-layer process used to pattern 50 nm line-and-space features on x-ray masks. Because of undercutting during the two reactive-ion etching steps, this process has a very small process latitude.

the ratio of the volume integrated exposure by the backscattered electrons to that by the forward scattered electrons, and for a thin-membrane substrate, a large fraction of the incident, energetic electrons simply go all the way through the membrane. The electrons which exit out the back side of the membrane cannot be backscattered into the resist and contribute to exposure at remote locations. With the reduction of this background exposure level, the contrast of the e-beam exposure on a membrane can be significantly higher than that on a solid substrate. Computer simulation programs have been written to model the electron scattering and predict their effect on process parameters [34].

We have successfully used 50 keV e-beam systems to expose features as fine as 50 nm line-and-space on resist as thick as 250 nm. In this case, the resist is thick enough to use as a mold for electroplating. This simple, three-step (expose, develop, electroplate) method is shown schematically in Fig. 3-9. Compare this simple process with the much more complicated tri-level scheme depicted in Fig. 3-8 and it's not surprising that the former has significantly higher yield. The keys to the success of the high-energy e-beam lithography are: (1) The use of the high energy electrons to reduce β_f and to give the electrons sufficient energy to penetrate the membrane. (2) A thin membrane enables most of the incident electrons to exit out the back side, reducing the number of backscattered electrons and, thus, the background exposure level. (3) A thin plating base (5 nm NiCr/10 nm Au) reduces the fraction of electrons backscattered from the plating base. (A number of groups use a significantly thicker plating base [22]. We feel that a 10 nm-thick layer of Au is more than sufficient. Additional Au only serves to increase backscattering.)

A reduction in the number of backscattered electrons and, hence, the background exposure level leads to a reduction of the proximity effect (described in Sec. 2.2). We have verified experimentally with 50 keV e-beam lithography and 1 μm-thick mask membranes with plating base thicknesses (5 nm NiCr/10 nm Au) that a substantial reduction in η_E occurs, and leads to a reduction in the proximity effect relative to solid substrates (see Fig. 3-10) This reduction in proximity effect would likely not be possible at 25 keV.

50 keV E-Beam Lithography

250 nm

PMMA — Au plating base

— Nitride membrane

1) e-beam expose

50 nm

2) Develop and plate Au
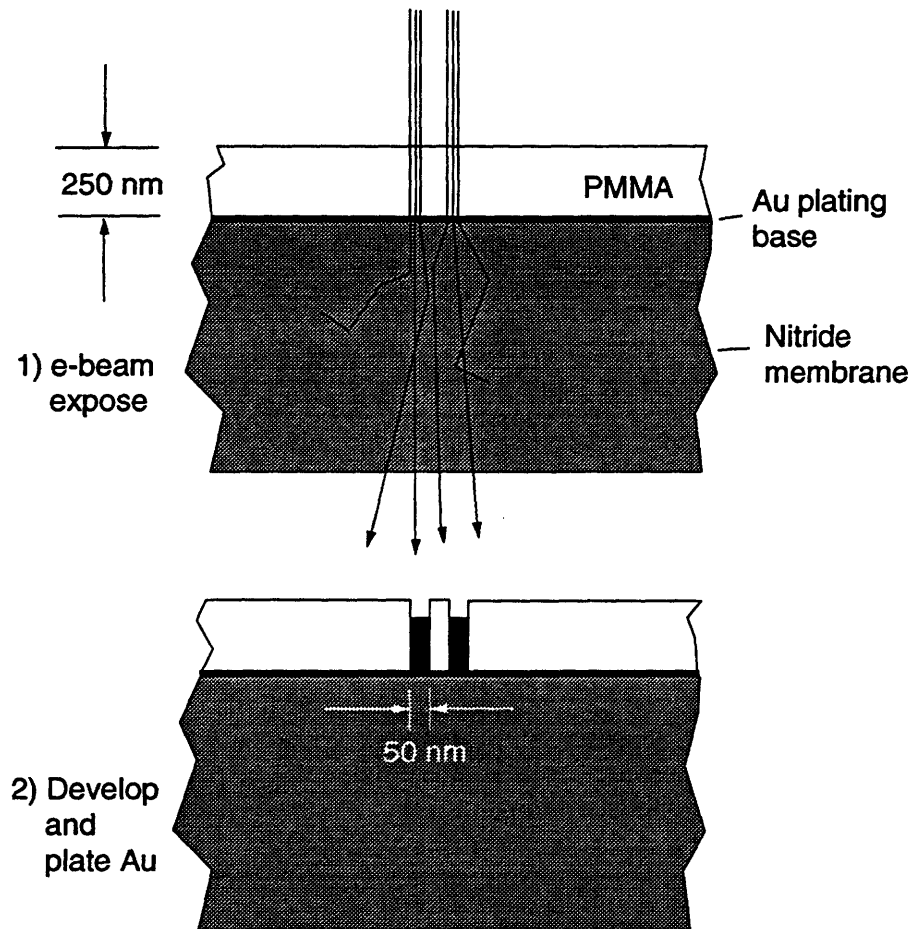
WC930204.4

Figure 3-9: Patterning of x-ray masks using 50 keV e-beam lithography and Au electroplating. A significant number of incident electrons go completely through the membrane, thereby reducing the background exposure level. The resulting increase in contrast allows the exposure of resist thick enough to use as a mold for electroplating.

The next sections describe our work using two 50 keV e-beam lithography systems to write fine features (as fine as 50 nm line-and-space) in thick resist on x-ray masks. The first section describes our collaboration with a research group at IBM Yorktown Heights to write x-ray masks for quantum-effect devices. The VS-6 is a vector-scan e-beam system which has been optimized for resolution [25]. The next section describes our work in collaboration with researchers at the U. S. Naval Research Laboratories (NRL) to write x-ray masks with features as small as 60 nm using a commercially-available e-beam system (JEOL JBX5DII) [26, 35]. The goal of this work is to demonstrate the ease with which a quantum-effect device can be conceived, a mask pattern designed, and an x-ray mask e-beam exposed remotely. This ability to have masks written remotely means that those interested in quantum-effects research need not make the heavy capital investment (> $2.5 million) on an advanced e-beam lithography system, but can instead invest in a low-cost x-ray exposure system and have masks made remotely.

Using the VS-6 to Expose PRESTFET patterns

The VS-6 vector-scan e-beam system at IBM Yorktown Heights is used for lithography in the 10-100 nm linewidth domain [36]. In order to achieve resolution and stability at these dimensions, the system is designed to minimize magnetic interference and electrical noise. In addition, mechanical stability is provided by mounting the sample on a glass substage with glass posts. After the sample is moved to its desired position (as measured by a laser interferometer), the substage is raised until the glass posts touch against the lens mount. This action locks the stage mechanically to the lens support and provides high mechanical stability.

The PRESTFET patterns exposed on the VS-6 consisted of two interdigitated lines spaced at various pitches from 60 nm to 200 nm. Since the pattern is relatively simple, the numerical coordinates of the lines and boxes were entered directly into the computer which drives the e-beam system. For future work, we have written a short computer program that converts the output from a standard CAD layout program to a format which can be interpreted by the computer which drives the beam deflectors.

Plated gold

Pad exposed at 2x clearing dose

← 150 nm →

50 keV e-beam

300 nm PMMA

Plating base

SiN$_x$ membrane

1 μm

RG920721.2.ai
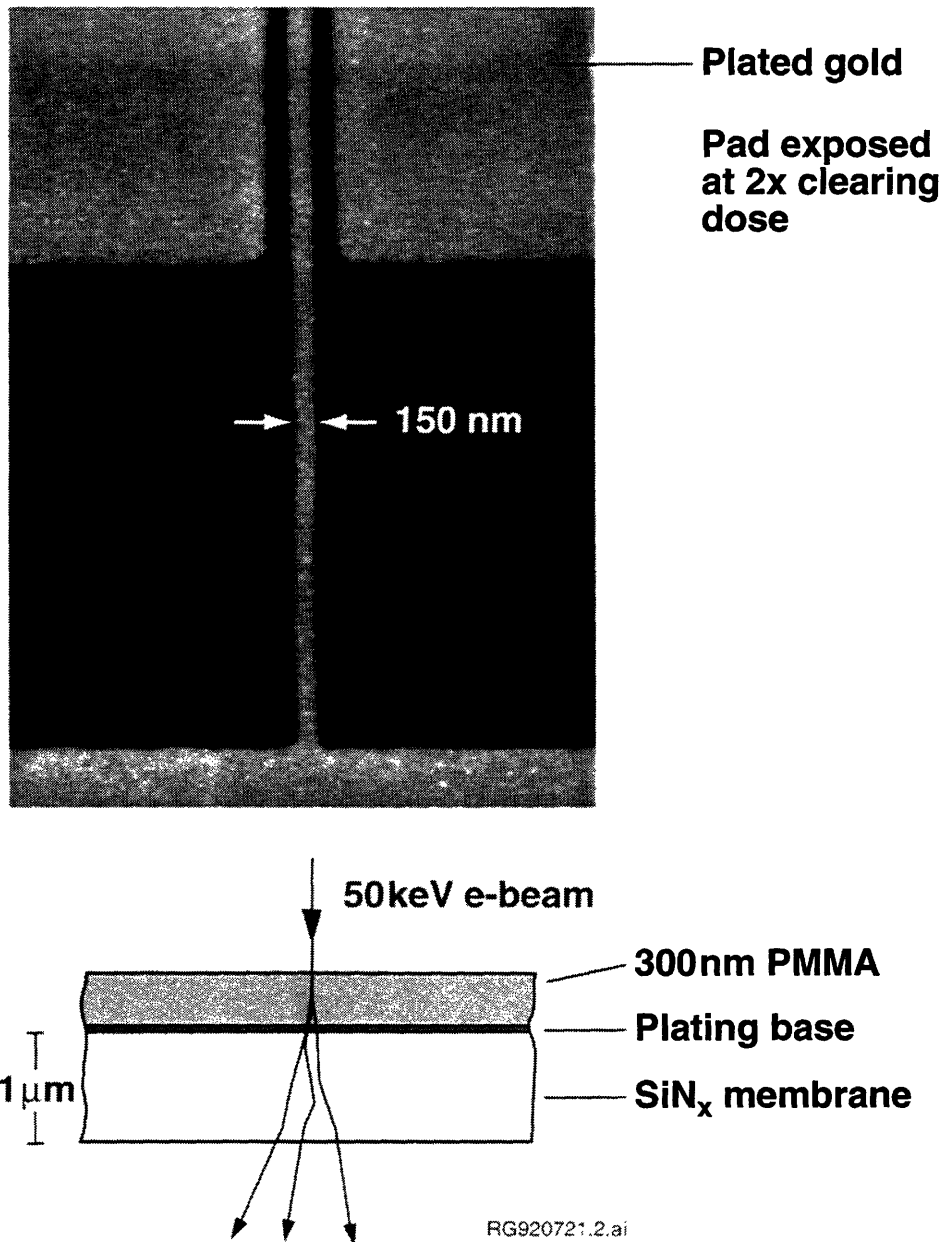
Figure 3-10: In the micrograph, the absence of linewidth-widening as the line runs between the large pads indicates the absence of proximity effect for e-beam patterning *on an x-ray mask blank.* A large fraction of the incident electrons simply go through the membrane, thus leading to reduced backscattering.

We can then send the converted data electronically.

An array of three different doses was used at each device pitch to determine optimal exposure conditions. We set the e-beam focus by looking at the four areas on the mesa of the mask where the PMMA had been been stripped off, and the 200 nm-thick Au film scratched. The scratch marks are located at the diametrically opposite positions (0°, 90°, 180°, and 270°). Since the mesa and membrane form an optically-flat surface, the focus at any point on the membrane where the patterns are to be written can be easily calculated by interpolation. In addition, astigmation was set by looking at fine features of the scratch marks. A total of 150 device patterns plus alignment marks were exposed per mask. A typical strategy was to center the dose around a particular value (in our case, for the development parameters listed in the next paragraph, this was around 430 $\mu C/cm^2$) and varied by $\pm$ 5%. Once the masks were e-beam exposed at IBM, they were shipped back to MIT for further processing.

The membrane samples were developed in a solution of 1:2 methyl isobutyl ketone (MIBK) : isopropyl alcohol (IPA) at a temperature of 21.0 $\pm$ 0.1°C for 2 minutes, followed by a 30 second rinse in isopropyl alcohol. We used a gentle nitrogen flow to dry the sample and then immediately placed it in a reactive-ion etching (RIE) system for a quick oxygen plasma etch to remove any residual organics (so-called "de-scum"). The anisotropic nature of RIE allows us to clean out the region between resist lines without substantially affecting the resist linewidth or profile. The etch was designed to remove 20 nm of PMMA which took about 6 seconds with the parameters we used (0.13 W/cm^2, 400V bias, and 10 mtorr pressure). After de-scumming, the samples were immediately electroplated with Au (see next chapter for Au plating details). The Au was plated to a minimum thickness of 200 nm.

The masks were then inspected in the scanning electron microscope (SEM). Figure 3-11 shows the top view of patterns of typical masks exposed with the VS-6. Such first generation masks (those patterned by e-beam or FIBL), are referred to as "parent" masks. In Figure 3-11, note the lack of line widening as the lines run into the large gate pad. This again demonstrates the lack of proximity effect when e-beam

48

lithography is performed at 50 keV on mask blank membranes with a thin (10 nm of Au) plating base.

Using the NRL JEOL to expose x-ray masks

The NRL JEOL JBX5DII system is a commercially-available vector-scan electron-beam lithography system designed to write nanometer-scale patterns on a wafers or membranes. The electron source is a high- brightness, single-crystal LaB_6 cathode. The system employs an in-lens deflector. The JEOL systems allows for flexibility in beam size; up to 1 μm for coarse features and down to 8 nm for fine features.

The data format that the JEOL accepts is the J51 format. Patterns were designed at MIT using the CAD tool KIC [37]. In KIC, the smallest dimensional unit, "lambda", is typically set to the value of the smallest feature in the mask design or at the decade value just below the minimum feature size. For example, if we wish to make 80 nm features, it is convenient to set the lambda at 10 nm so that all features will be some integer number of lambda in size. For our x-ray mask work, lambda was usually chosen to be 10 nm (100 lambda per micron).

Once the mask is layed out, the pattern data file (KIC format) is converted to an appropriate intermediate format. In the past, we have converted the files to the binary stream format using the command "kictostrm." The files were then sent down to NRL using ftp over the Internet. Once at NRL, the stream files were viewed using GDSII, another CAD tool and then converted to the JEOL J51 format. At this point, field boundaries were defined relative to the patterns. It is important that field boundaries do not bisect fine features as jogging and stitching errors may occur in the patterning. The conversion software allows for shifting the pattern so that field boundaries do not intersect the fine features.

We have also converted files to the JEOL J51 format by using file conversion software developed by T. Lyszczarz at MIT Lincoln Laboratory. This conversion program accepts CIF (Caltech Intermediate Format) as the intermediate ASCII data form. KIC files are easily converted to CIF format by using the command "kictocif."
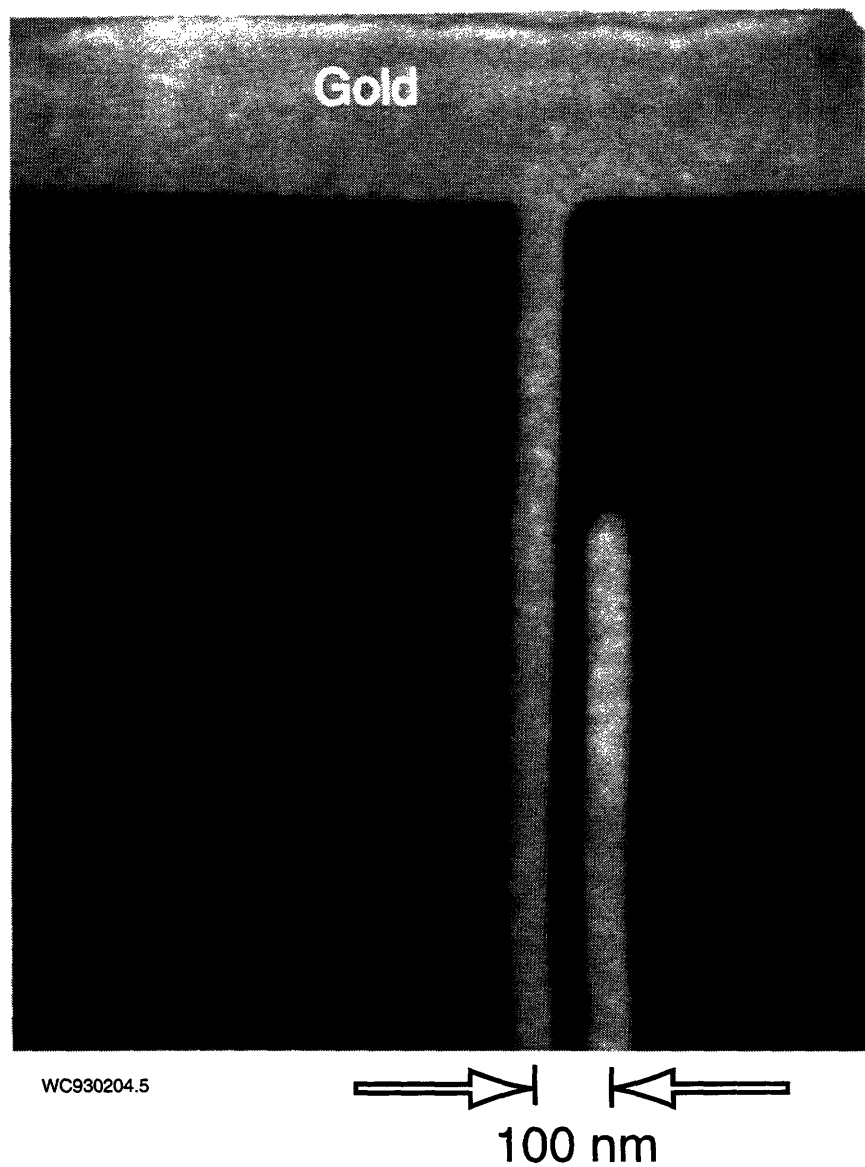
Figure 3-11: Top view of PRESTFET parent mask made using the IBM VS-6. The Au absorbers are plated to a thickness of 200 nm.

This conversion takes CIF files as its input and produces converted J51 files as its output. Beam voltages and field sizes are set. Again, the program allows the flexibility to shift field boundaries so that stiching errors are minimized.

The preparation of the mask blank was described in Sec. 3.2. We used 300 nm-thick PMMA (950 K mol. wt.) for all of our exposures. The samples were prepared at MIT and shipped by express mail to NRL. The accelerating voltage used was 50 keV. The focus was set by looking at the four scratch marks, as described in the previous section. The beam current used was determined via a compromise between resolution and writing time. The equation which relates the intrinsic beam diameter (without taking into account degradation due to aberrations, diffraction, and space charge) to current is given by Eq. 2.5. Clearly, the smaller the current, the smaller the beam diameter and, hence, the better the resolution. However, writing time increases with smaller beam current.

For most of the patterns below 0.1 μm in linewidth, a current of 15 pA was used. A dose of 500 $\mu C/cm^2$ was typically needed to expose isolated patterns at that linewidth. For large pads and optical alignment mark patterns, a beam current of 1 nA or 5 nA was used. Figs. 3-12- 3-14 shows top views of masks written by e-beam lithography at NRL for a variety of device projects where nanometer-scale lithography was needed.

X-ray Mask for 0.1 µm Gate Length
NMOS Ring Oscillator
(Mask written by e-beam lithography at NRL)
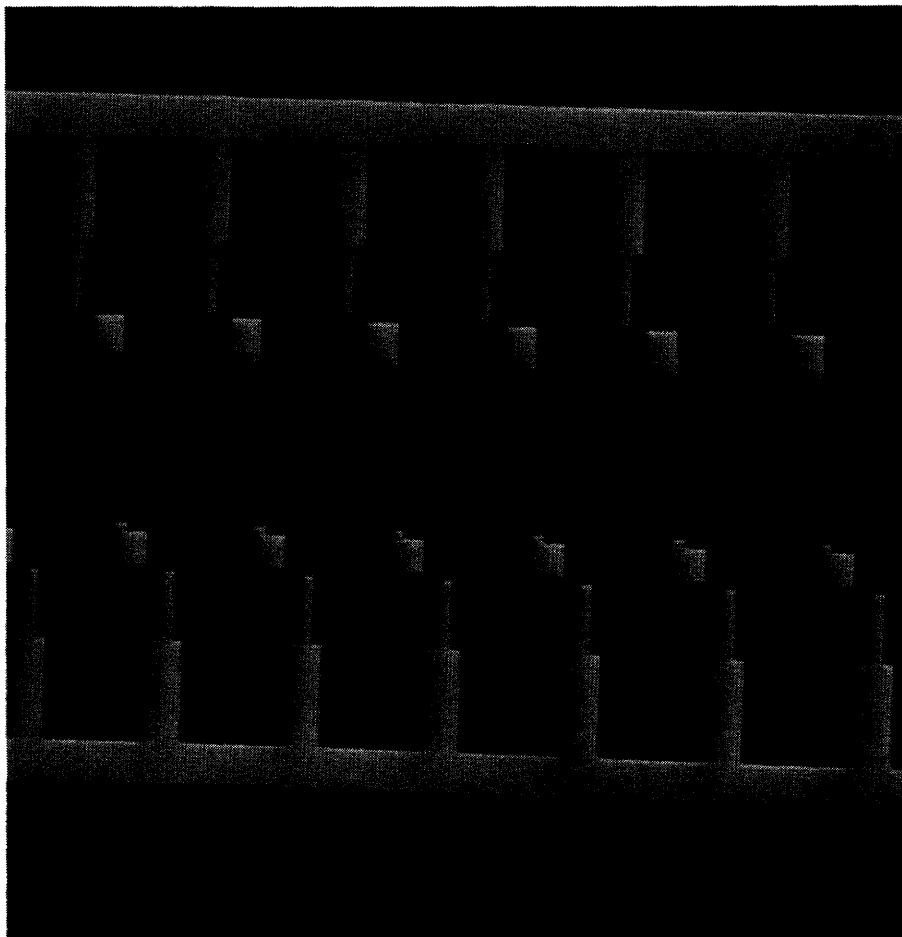
WC921001.1.ai

Figure 3-12: X-ray mask for a 0.1 μm gate length NMOS enhancement/ depletion ring oscillator. The e-beam lithography was performed at the Naval Research Laboratory (NRL).
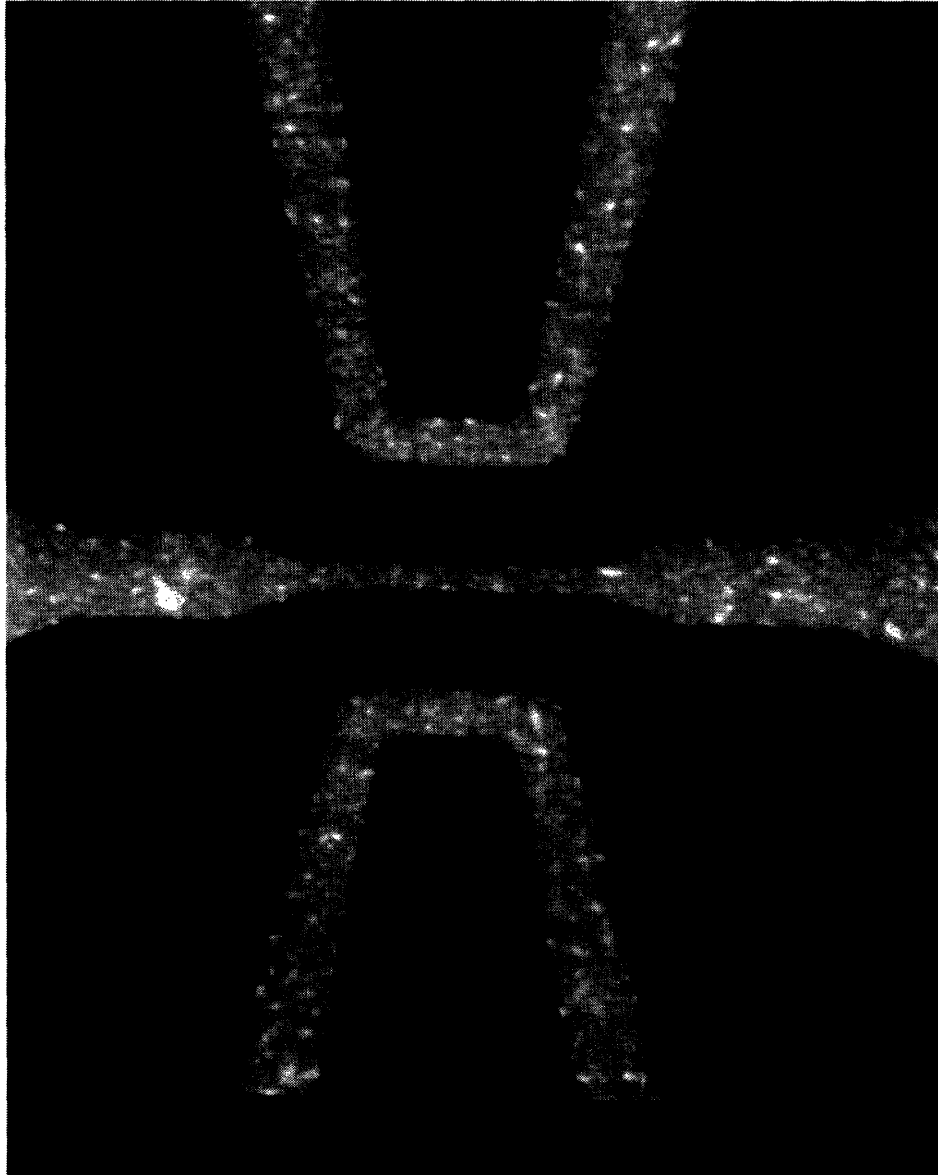
WC930204.6

Figure 3-13: X-ray mask for coupled electron waveguide devices The e-beam lithography was performed at the Naval Research Laboratory (NRL).

X-ray Mask for Grid-Gate Transistor
(E-Beam Lithography at NRL)

WC930204.7

150 nm
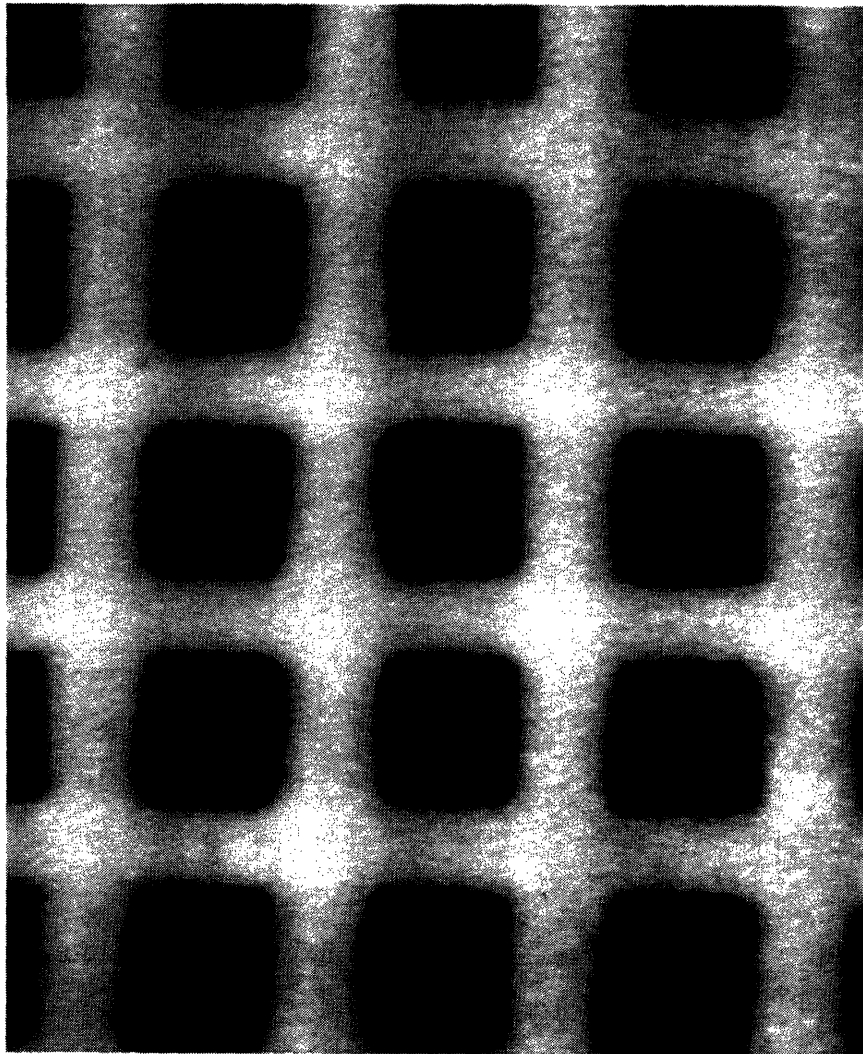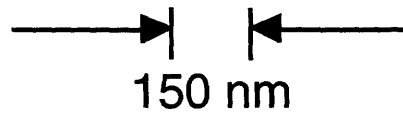
Figure 3-14: X-ray mask for GaAs/AlGaAs grid gate transistors. The e-beam lithography was performed at the Naval Research Laboratory (NRL).

Chapter 4

Gold Electroplating

4.1 Absorber Configuration

The choice of an x-ray mask technology involves the choice of an x-ray wavelength such that the mask membrane is reasonably transmissive (50 % or more) and the absorber thicknesses needed to get sufficient attenuation (10 dB attenuation) is small enough to allow sub-100-nm-feature patterning. For example, with the 1.32 nm Cu_L x rays that we use, a 1 μm-thick SiN_x membrane transmits roughly 50 % of the incident x-rays. The materials used for x-ray absorbers are high atomic-number elements such as tungsten (W) or gold (Au). At the 1.32 nm wavelength, a 10 dB attenuation would require a 200-nm-thick Au film or a 250-nm-thick W film. A 50-nm-linewidth pattern would then require patterning of a 4:1 height-to-width Au structure or a 5:1 height-to-width W structure. This is the essential challenge of absorber patterning technology.

Tungsten absorbers are patterned using a subtractive process. Low stress W absorbers can be deposited by controlling pressure during sputter deposition [38]. After deposition, resist is spun onto the sample and patterned using e-beam, focused-ion-beam, or x-ray lithography. The application of e-beam lithography to pattern resist on tungsten films will probably be quite limited due to strong proximity effect due to significant electron backscattering from the high atomic-number W film. This proximity effect can be reduced by using an intermediate insulating film between the

W and the resist [39], but this added complication in the processing is undesirable. The patterning of masks with W films would presumably be left to focused-ion-beam lithography, where backscattering is not an issue (see Sec. 3.3.1). Once the resist is patterned, the W is etched using the resist as an etch mask. There are two problems associated with this etching: (1) PMMA resist, desirable for its high resolution, has a low resistance to the fluorine based etchants used to etch W, and, thus, is a poor etch mask. Chemically-amplified novolak resists such as SAL-601, Ray-PN, and Ray-PF have good etch resistance, but have not proven to have resolution in the sub-100-nm domain. (2) Even if an adequate resist were available, the etching of a 50 nm-linewidth, 5:1 height-to-width W structure without significant undercutting is extremely difficult. The problem is exacerbated by etching directly onto a membrane which is not properly heat sunk. It is believed that He back side cooling during the etch will partially alleviate the undercutting problem [40].

In contrast to the difficulties associated with W etching, an x-ray mask fabrication process utilizing Au electroplating is remarkably straightforward. E-beam lithography can be used with a Au-plating process and achieve very high resolution (see Sec. 3.3.2) because the substrate is a thin membrane of SiN_x coated with a thin plating base, and, thus, a significant number of incident electrons go through the membrane and do not contribute to backscattering (and, hence, the proximity effect). The resulting high-contrast exposure allows for use of a resist film thick enough to be used as a mold for electroplating Au features on x-ray masks for use at the 1.32 nm source wavelength. Consequently, a process using Au electroplating is straightforward (no dry etching process needed) as depicted for the case where e-beam lithography is used (Fig. 3-9) or where focused-ion-beam lithography is used (Fig. 3-5); it is equally straightforward where x-ray lithography is used. For this reason, the x-ray masks described in this thesis work utilized Au electroplating to form the absorber patterns. The next sections describe our work in developing a low-stress Au electroplating procedure.

4.2 Low-Stress Au Electroplating

Control of the Au plating process is essential for repeatably achieving high-quality absorber films. The characteristics of the plated Au film can affect the x-ray masks in the following ways:

- *Stress of the film* – films plated under high stress may affect the absorber pattern in two ways: (1) absorber delamination from the substrate, and (2) pattern distortion.

- *Plating uniformity* – the thickness of the film should be the same across the entire plated area.

- *Morphology* – the grain size and the surface roughness should be small in the plated films [41].

- *Reproducibility* – plating results should be reproducible from run to run. This requires careful monitoring of the the plating solution.

In-plane pattern distortion may arise due to stress in the plated Au. Films plated under stress can distort a desired pattern. The distortion at any point on a pattern should be a small fraction (e.g. 1/5 to 1/10) of the minimum feature size on the mask. Otherwise, pattern distortion will lead to mask overlay errors. This section describes the basic principles of our plating technique using a commercially-available plating solution with a confined plating geometry and a stagnant solution to produce low-stress Au films.

In our electroplating system the solution is pumped, filtered, and circulated while held at fixed temperature (to within $\pm$ 0.5 °C). The bath can be agitated inside the plating beaker through the use of a magnetic stirrer (see Fig. 4-1). We use a commercially-available plating solution (Sel-Rex BDT-510) [42]. Because this alkaline, sulfite electroplating bath contains neither cyanide nor thallium, it is generally safer to use than other popular baths.

Sample holder

Thermocouple

Connector to current supply

Plating solution

Pump

Hotplate & Stirrer

Particle filters
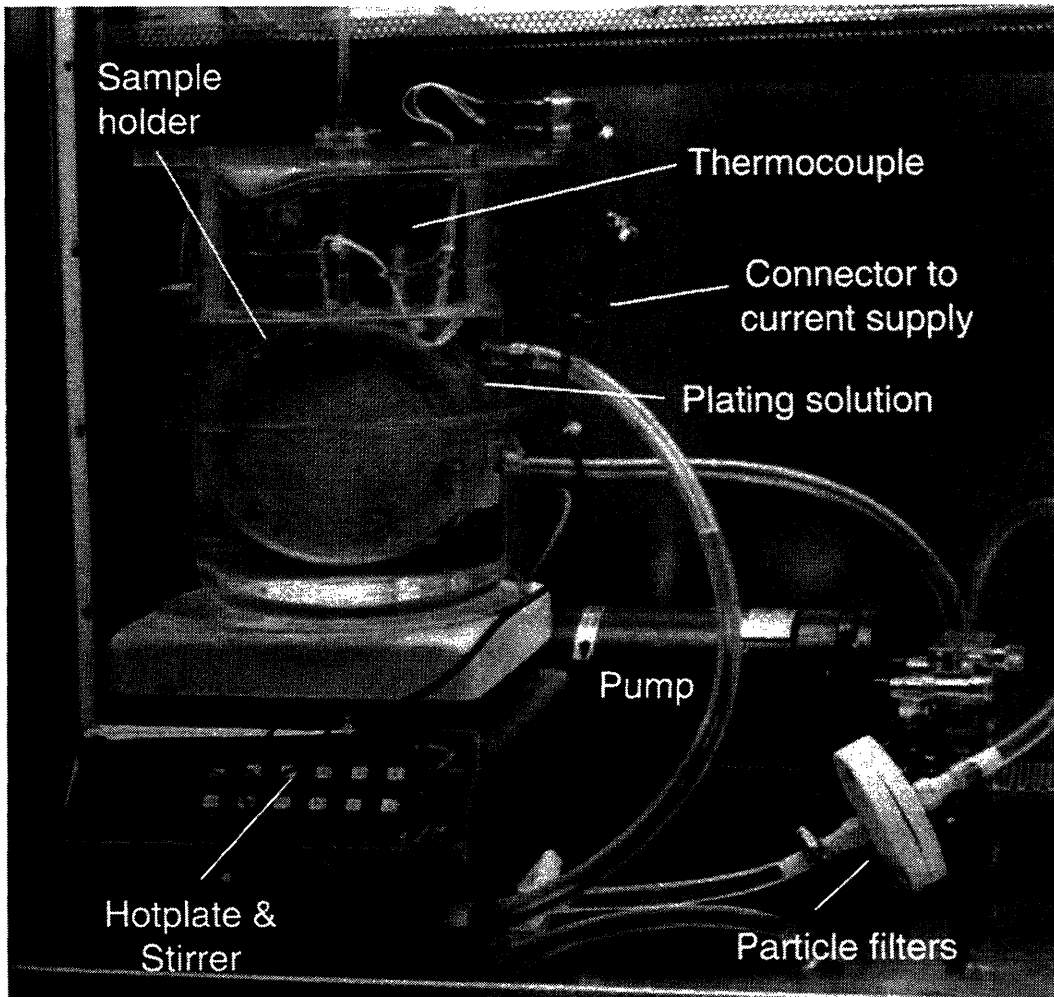
WC930204.8

Figure 4-1: Au electroplating system.

The sample holder includes a spacer ring used to separate the anode and the sample in a "sandwich" configuration as shown schematically in Fig. 4-2 and in the photograph in Fig. 4-3. The ring accomplishes two objectives: (1) It separates the anode (in our case a platinum mesh and the sample by a small, fixed gap. This keeps the electric field lines normal to the surface and parallel to one another between the two electrodes (i.e. reduced fringing), yielding a uniform current density, and, hence, a uniform plating rate. (2) It restricts the area plated to the area within the inner diameter of the spacer ring. The Pt mesh is used to make an ohmic contact to the plating solution while allowing the plating solution to flow through it. A constant-current supply connected between the Pt mesh (anode) and the sample (cathode) drives the plating reaction (see Fig. 4-2).

Plating is performed using a stagnant solution – that is, with the pump and stirrer off. We discovered that plating in an agitated solution led to a non-uniform plating rate across our samples. This was perhaps caused by the effects of turbulence on the boundary layer between the electrolyte and the surface of the substrate. (Another method to reduce the effects of turbulence is to use a fountain plating scheme [41, 43]). Plating in a stagnant solution yielded Au films with a maximum thickness variation of 3% over the area plated while plating in a stirred and pumped solution yields more than 30% thickness variation. The amount of Au in the solution within the volume defined by the substrate, the spacer ring, and the Pt mesh, is an order of magnitude more than the quantity plated on our typical x-ray mask ($\sim$ 200 nm). Thus, Au depletion within the stagnant volume is negligible. In between plating samples, the stirrer and pump are turned on to maintain solution uniformity.

Using a stagnant solution held at a temperature of 33 °C, with the anode and sample configured as in Fig. 4-2, we can measure the stress of the plated-Au film as a function of current density. The stress was calculated by measuring the bow of a Si wafer before and after electroplating, and converting the difference in curvature into

Pt Mesh Anode   **Spacer ring**   **Sample to be plated**
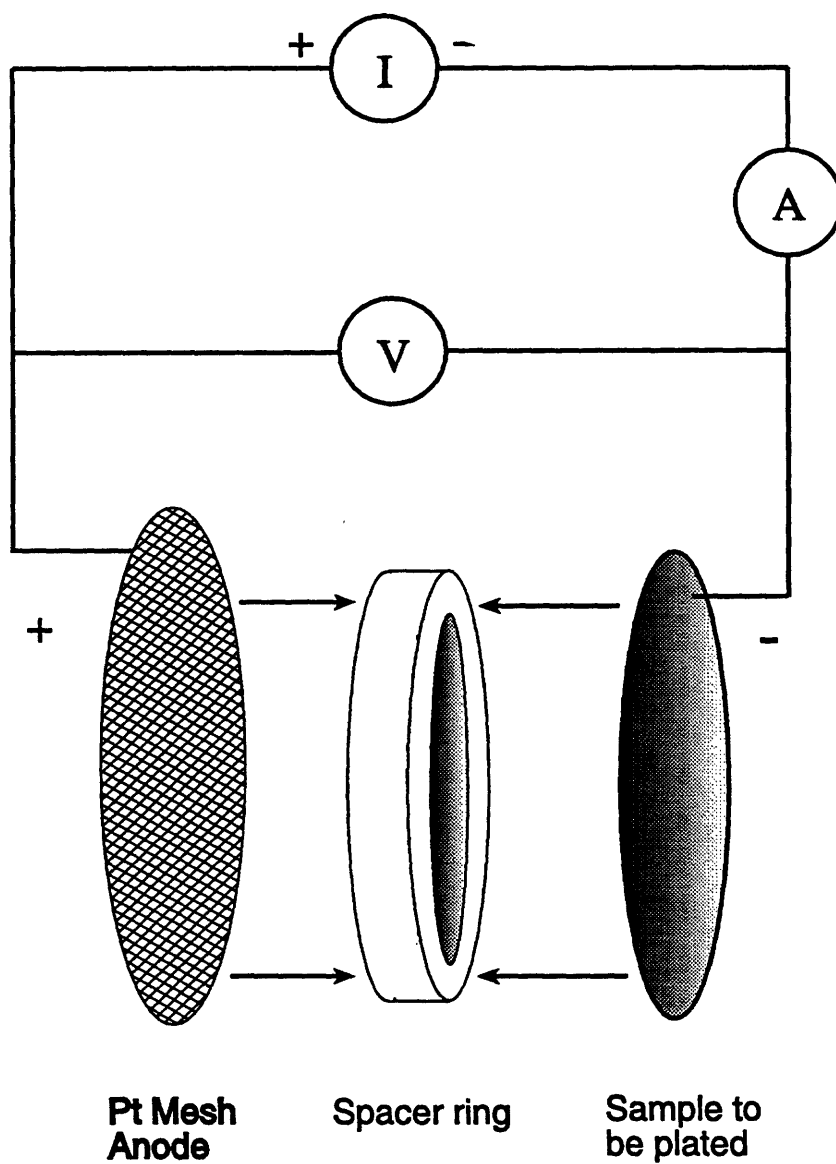
Figure 4-2: Plating configuration. The Pt anode and sample are held apart by the thickness of the spacer ring. Plating is induced by a regulated current supply.

Current source connector

Pt mesh anode

Contacts (3)

Mask

Spacer ring
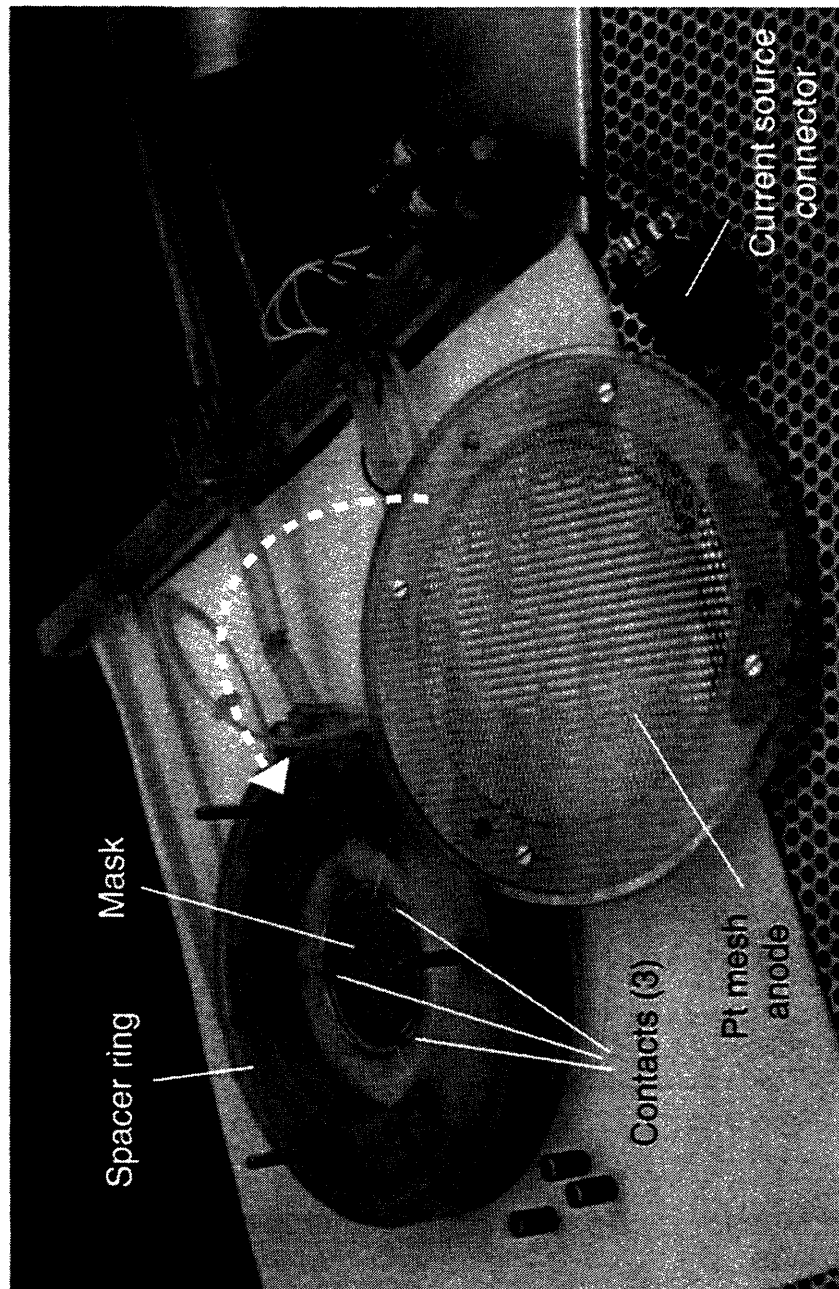
WC930204.9

Figure 4-3: Sample holder in the electroplating system (designed by R. Fleming of the MIT Center for Space Research). Note that electrical contacts is made to the sample through three contact pins located 120° apart.

stress by applying Stoney's Formula [44]:

$$\sigma_f = \frac{1}{6} \frac{E}{1-\nu} \frac{t_s{}^2}{t_f} \frac{1}{R}$$ (4.1)

where σ_f is the stress of the plated Au film; E, ν, and t_s are, respectively, Young's modulus, Poisson's ratio, and thickness of the substrate (Si wafer); t_f is the thickness of the Au film; and R is the radius of curvature of the substrate. Only azimuthally-symmetric wafers were selected. The wafer curvature can be measured using either a Fizeau interferometer or a surface profilometer. The interferometer gives a contour map of the Si wafer. By counting the number of fringes from the center of the wafer out to some distance r and comparing it with the number of fringes after plating, we can extract the stress of the Au film. The profilometer can also be used to determine the stress of the plated Au. The stylus of the profilometer can be scanned from the center of the plated wafer radially outward. A scan of the sample before plating is compared to a scan of the wafer after plating. The difference in curvature can be related to film stress using Eq. 4.1. The measurements between these two methods are in excellent agreement.

The measurements of plated-Au stress versus current density under the conditions described in the previous paragraph is shown in Fig. 4-4. The figure shows that at low values of current density the Au is plated under compressive stress, while at high values the film is under tensile stress. The curve goes through the zero-stress point at around 0.8 mA/cm^2. Other researchers have failed to find such a zero-stress point [45]. This result provides a prescription for plating zero-stress Au absorbers: use the confined plating geometry defined by the spacer ring, and plate at a current density value of 0.8 mA/cm^2 in a stagnant solution of BDT-510.

4.3   Au Plating for X-ray Masks

The plating of Au absorbers for x-ray masks exactly follows the techniques described in the previous section for plating of low-stress Au. In order to calculate the value of

62
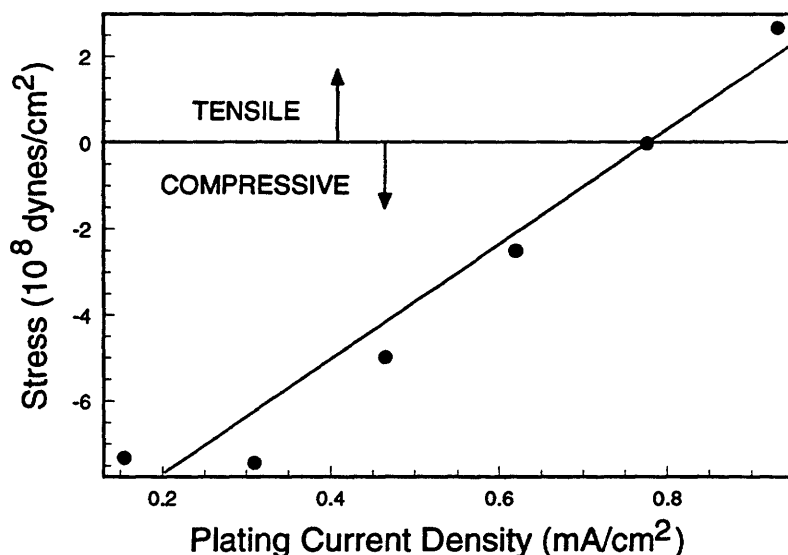
WC930204.10

Figure 4-4: Stress of electroplated Au films as a function of plating current density for the BDT-510 solution in the plating configuration depicted in Fig. 4-2.

current used for electroplating, the area to be plated must be known with accuracy. In practice, when plating fine geometries such as 50 nm patterns, we usually uncover a large region of the sample outside the membrane area so that the plating area is fixed and easily calculated. The step-by-step plating procedure is listed in Appendix C.

The plated Au films tend have low surface roughness (e.g. see Fig. 4-5) and are uniform in thickness over the entire area of the mask. In order to ensure reproducibility, the plating is monitored through the use of a computerized data base [46]. The pH of the plating solution is measured before each plating run and the value is noted in the log book. The pH of the BDT-510 solution should be between 8.5 and 9.0. The amount of Au plated out of the solution is calculated by multiplying the thickness of Au plated by the area plated and by the density of Au. This is also recorded in the log. When the accumulated amount of Au plated out of the solution exceeds a small fraction (say 10 %) of the total Au originally in the solution, the solution is
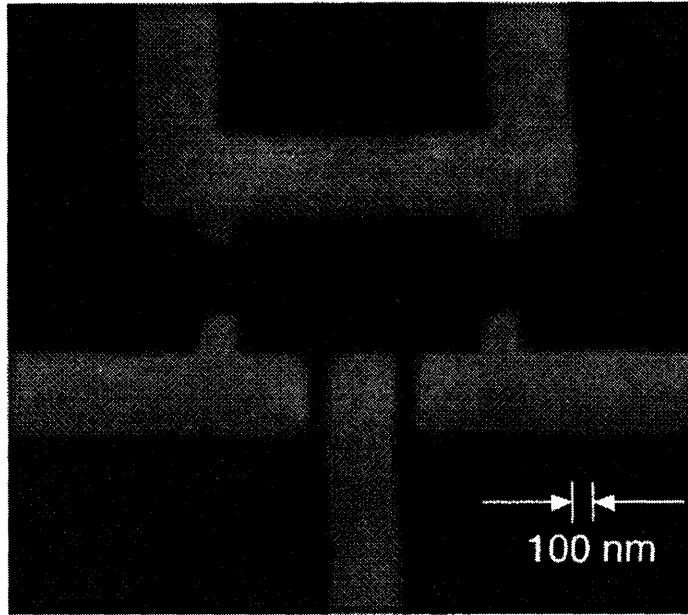
WC930204.11

Figure 4-5: SEM micrograph showing lack of surface roughness in the low-stress plated Au.

considered due for replacement and is sent back to the vendor.

Chapter 5

X-ray Mask Replication

An x-ray mask which has been patterned by e-beam or focused-ion-beam lithography (parent mask) can be replicated using x-ray lithography to yield many copies (daughter masks). If positive resist is used to make both the parent and daughter masks, then the daughter mask will have a polarity opposite to the parent. In other words, what was originally x-ray opaque on the parent mask becomes x-ray transmissive on the daughter and vice versa. For our applications devices in the sub-100-nm-linewidth scale, this is often desirable. The daughter mask can be used to expose the desired pattern into PMMA (a high-resolution positive resist) on the device substrate.

The replication of parent masks requires that patterns originally written on the parent mask be faithfully reproduced on the daughter. This is a question of resolution. The first section of this chapter is a discussion of the factors which can limit resolution; factors such as photoelectron range, penumbra, and diffraction. The section also describes a series of experiment that we performed demonstrating that the effects of diffraction are not as severe as had been anticipated based upon simple scalar diffraction calculations. The second section in the chapter describes the procedure we use to replicate x-ray masks, based upon the resolution limits described in the first section. The last section lists the procedure by which the replicated masks are aligned to, and exposed onto device substrates, often small pieces of GaAs.

5.1 X-ray Lithography – Resolution Limits

5.1.1 Photoelectrons

There is a considerable discussion of the resolution limits of x-ray lithography in the literature [47, 14, 48]. Up until 1988, it was widely believed that the minimum achievable feature size was about equal to the maximum range of the photoelectrons that are released when an x-ray photon is absorbed in the imaging resist [49]. Photoelectron emission is depicted in Fig. 5-1(a) where an x-ray photon is absorbed by an atom in the resist and an electron is emitted from an inner shell of the atom. The emitted electron, a photoelectron, has an energy E_{pe}, where E_{pe} is given by:

$$E_{pe} = h\nu - E_b \tag{5.1}$$

where $h\nu$ is the x-ray photon energy and E_b is the binding energy of the electron in the atom from which it was ejected. Because it was believed that given a high enough energy, the photoelectron would have sufficient range to expose resist in remote locations (where exposure was not desired), in experiments where the finest linewidth resist features (17.5 nm-linewidth) were desired, low energy x-ray photons (i.e., $\lambda = 4.5$ nm, $E = 280$ eV) were used [13]. The ability to resolve the fine features in the experiments of Flanders appeared to be limited either by the property of the resist, polymethyl methacrylate (PMMA) or by the adhesion of the resist to the substrate.

While lower energy (longer wavelength) x rays have been used effectively to reproduce fine features (as the work by Flanders demonstrates), it is generally desirable to use higher energy (shorter wavelength) x rays to limit the effects of diffraction and to allow the use of inorganic membranes such as silicon-nitride and silicon, which are virtually opaque to x rays with wavelength longer than 2 nm. The motivation for using inorganic as opposed to organic membranes was discussed in Chapter 3.

As discussed in Chapter 2, experiments by Early *et al.* [14] showed that absorber patterns only 30 nm wide on a mask can be faithfully replicated in PMMA resist at the wavelengths 0.83, 1.32, and 4.5 nm, in a configuration designed to maximize any
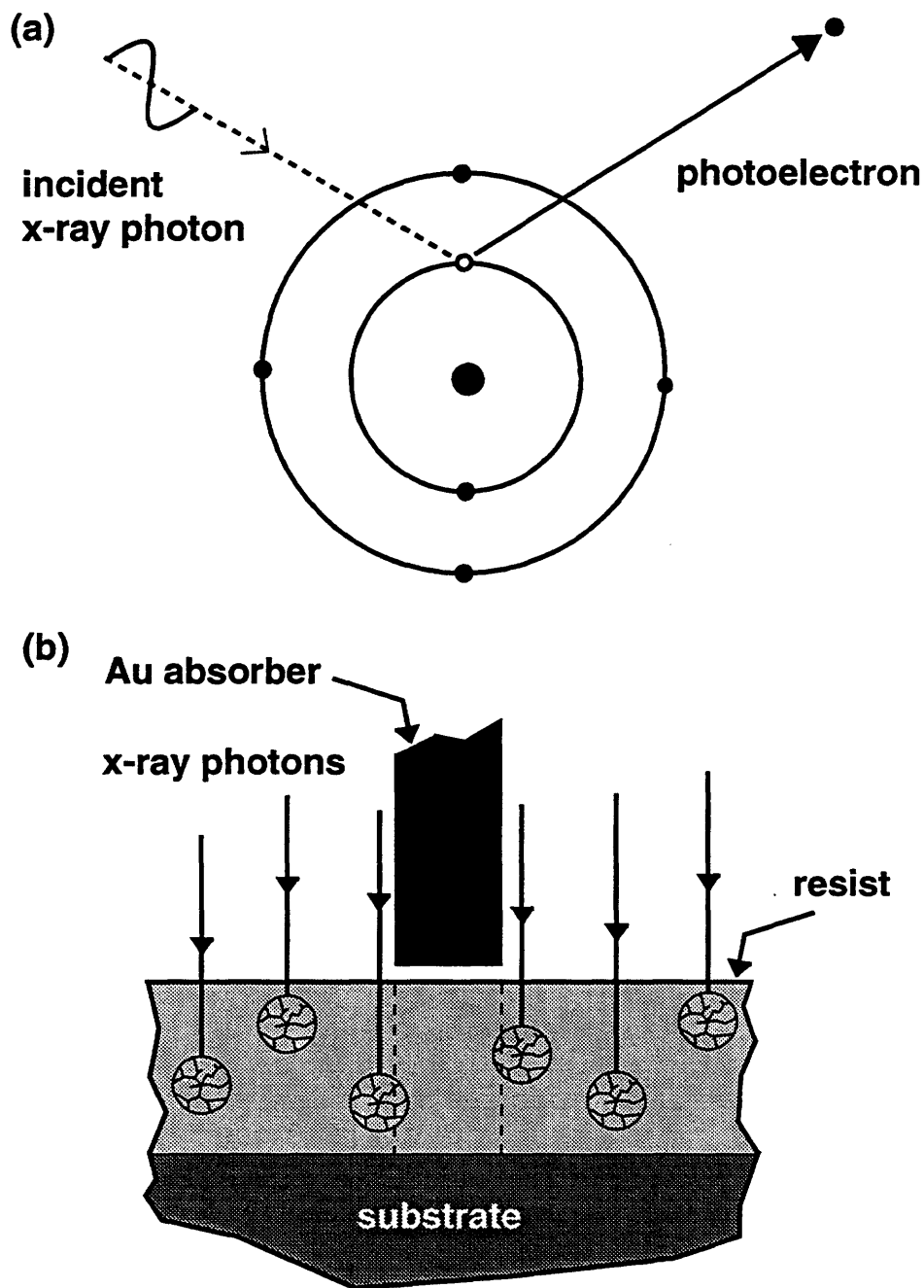
WC930204.12

Figure 5-1: (a) Photoelectron generated by an x-ray photon incident on a carbon atom, the predominant constituent of resist. (b) For many years, it was believed that photoelectrons generated during x-ray exposure had sufficient range to limit resolution. Recent experimental results have shown that the effect of a finite photoelectron range is substantially smaller than had been predicted because of the strongly-peaked "point-spread" function for Auger and photoelectrons. After Early, ref. [1].

deleterious effects of photoelectrons (i.e., isolated 30 nm-wide PMMA lines were left undeveloped in an otherwise fully exposed field). The micrographs of the exposures were shown in Fig. 2-2. These results were consistent with the modeling by Murata et al. [50] which showed that the "point-spread functions" for exposure with 0.83 and 1.32 nm x rays are strongly-peaked due to Auger electrons, and fall off by $\sim$ 50 % for 0.83 nm x rays and $\sim$ 90 % for 1.32 nm x rays at a radial distance of $\sim$ 5 nm. The energy absorbed in resist is a convolution of this sharply-peaked point-spread function and the areal image, which depends on the diffraction that takes place between the x-ray mask and the resist film. Since the point-spread function is sharply peaked, the convolution of any areal image with this sharply peaked function leads to only a slight degradation of the original image (i.e. in the limit of an infinitely sharp point-spread function, the delta function, the convolution of the areal image with the delta function yields the original image). This is demonstrated in Fig. 5-2 where the point-spread function for 1.32 nm x rays is plotted as a function of lateral distance (Fig. 5-2(a)). In Fig. 5-2(b), the point spread function is convolved with the areal image of a 30 nm-linewidth slit and absorber line

5.1.2 Diffraction Experiment

From the results of Early et al. [14], it is now clear that diffraction is the only significant limit on resolution in proximity x-ray lithography in the wavelength range 1 to 4.5 nm at least down to $\sim$ 20 nm minimum feature sizes. In order to explore the limits imposed by diffraction, we performed an experiment in which a patterned x-ray mask was exposed onto a resist coated substrate at a series of well-defined mask-to-substrate gaps. After development of the resist and lift-off of metal, we analyzed the substrate in the scanning-electron microscope.

The configuration of the x-ray mask used in this experiment is shown in cross section in Fig. 5-3. In top view, it consists of two interdigitated lines or "fingers" connected to large pads. The pitch (p) is 100 nm (linewidths $\sim$ 50 nm) and the line length is 50 μm. The mask pattern was fabricated using 50 keV scanning elec-
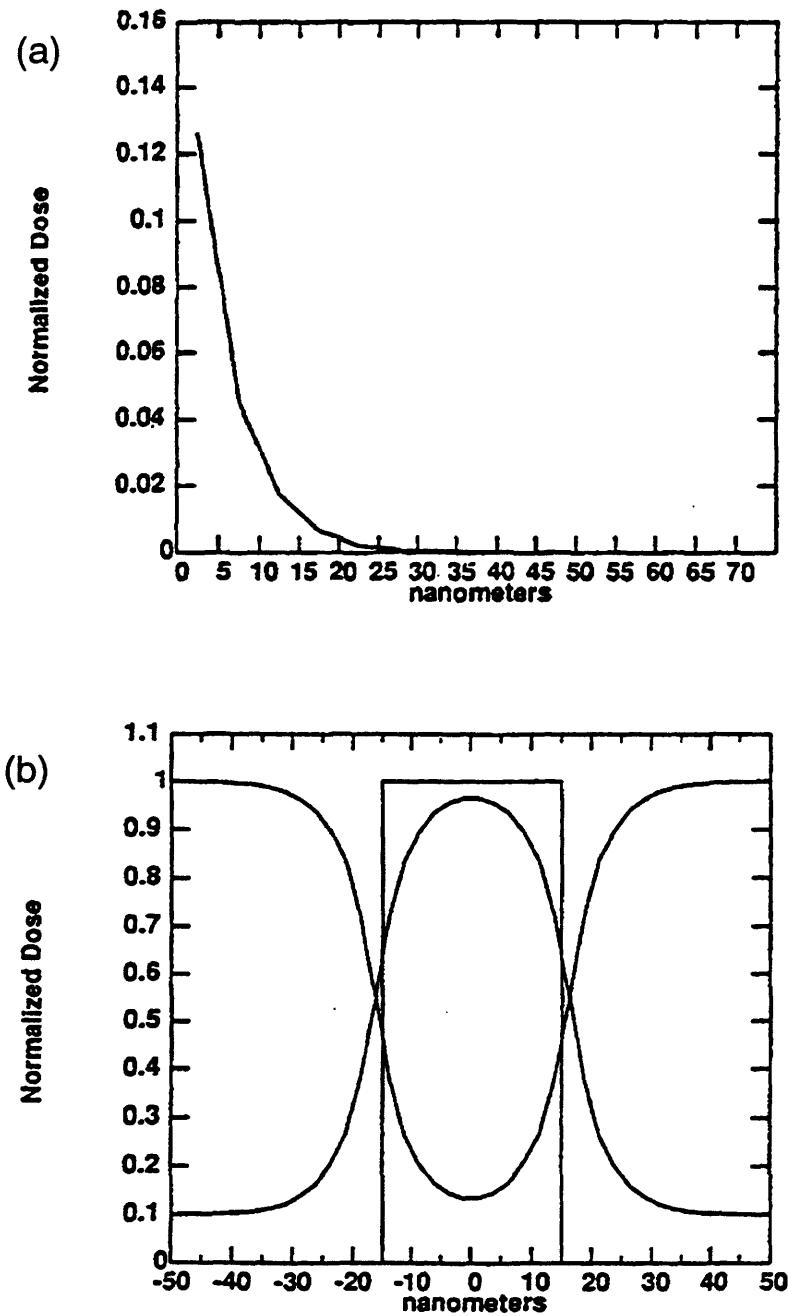
Figure 5-2: (a) Normalized energy distribution for absorbed Cu_L x rays from an infinitely thin line source (point-spread function). (b) Convolution of point spread function in (a) with the intensity function corresponding to a 30 nm-linewidth slit and a 30 nm-linewidth absorber. 10 dB attenuation absorbers are used. After Early, ref. [1].

69

tron beam lithography followed by electroplating (see Chapter 3 and 4). The mask membrane (1 μm- thick SiN$_x$) attenuates the 1.32 nm x rays by about 50%. The Au absorbers attenuate the x rays by 9.9 dB (i.e. by a factor of 9.8).

Mask Membrane, SiN$_x$

p = 100 nm

200 nm

electroplated Au

~ 50 nm
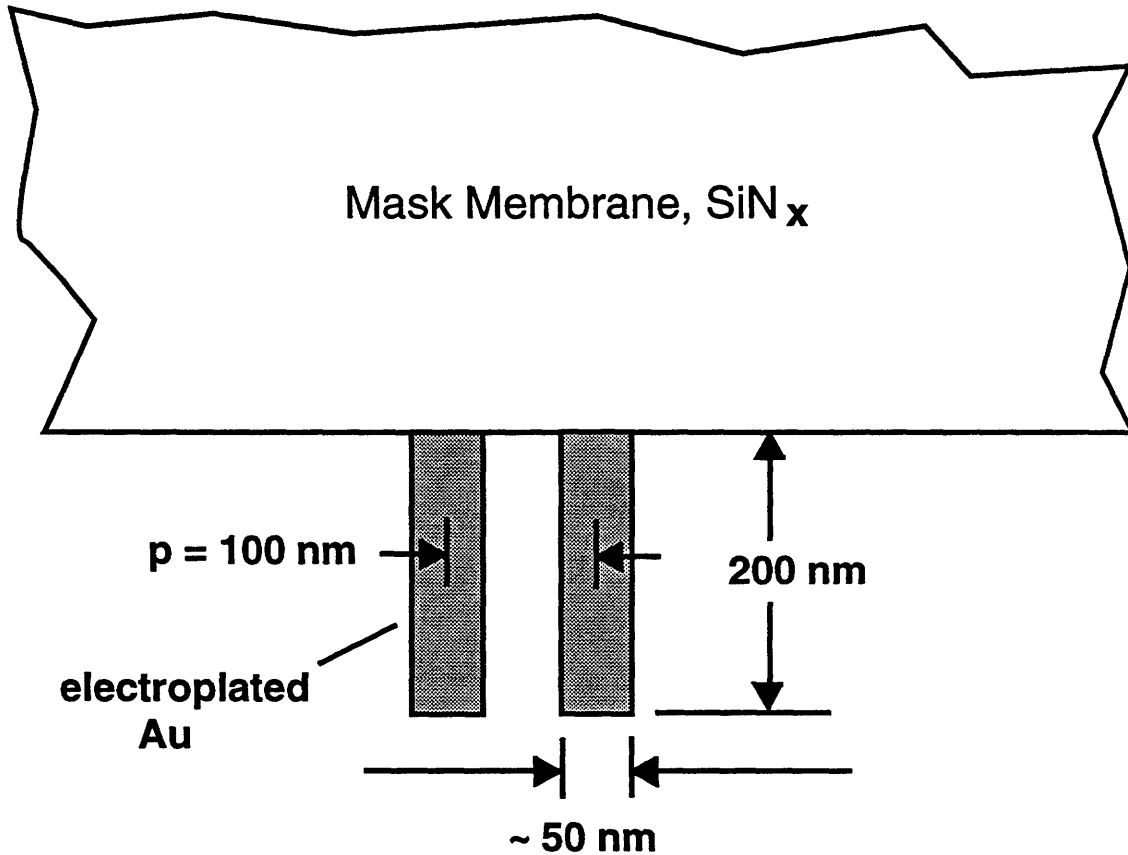
Figure 5-3: Schematic cross section of the 100-nm-pitch x-ray absorber structure on a silicon-rich SiN$_x$ membrane. The 200-nm- thick gold provides 9.9 dB attenuation (9.8-to-1 maximum image contrast).

X-rays were generated by electron bombardment of a water cooled Cu anode at 8 kV in a spot 1-2 mm in diameter. The only strong Cu$_L$ lines are at 1.3336 nm ($L\alpha_{1,2}$) and 1.3053 nm ($L\beta_1$) [51]. They have relative intensities of 1.0 and 0.75 [52], and linewidths 0.0053 and 0.0048 nm, respectively [53]. Using the expression for coherence length:

$$l_c \sim \frac{\lambda^2}{\Delta\lambda} \tag{5.2}$$

where l_c is the coherence length, λ is the wavelength, and $\Delta\lambda$ is the linewidth, the coherence length is ~ 340 nm for the $L\alpha_{1,2}$ line and 360 nm for the $L\beta_1$ line.

Exposures were carried out in vacuum at mask-to-sample gaps of 0.17, 1.79, and 2.72 μm. For the purpose of this experiment, where precise gap control is essential, we patterned photoresist stripes of known thickness on the mask and then held the mask in contact with a PMMA- coated Si substrate by applying a potential of 60 V between the back of the mask and the Si substrate. (This scheme also eliminated the possibility of relative motion due to vibration.) During exposure, the capacitance was monitored to ensure that the gap remained unchanged. The photoresist stripes were 50 μm wide with 100 μm pitch, and were oriented perpendicular to the interdigital line pairs. Thus, each test pattern was about half covered by a photoresist stripe. Because the photoresist stripes partially attenuate the x rays, the result of two exposure doses could be evaluated in a single experiment.

Penumbral blurring due to the finite source size (i.e. the spatial incoherence of the source) was measured in a separate experiment. For a constant-intensity source of spatial extent d, the penumbral blur δ can be expressed as:

$$\delta = d\frac{G}{D} \qquad (5.3)$$

where G is the mask-to-substrate gap, and D is the source-to-mask distance. This can be derived from a simple geometrical argument. Assuming a Gaussian-source spatial distribution, the full width at half maximum (FWHM) of our source was found to be 1.87 mm. The source-to-substrate distance was 26 cm. At a gap of 2.72 μm this corresponds to an image blur at the resist plane of 19.6 nm FWHM. A useful parameter β can be defined to relate the penumbral blurring to the minimum feature size, W [54].

$$\beta = \frac{\delta}{W} \qquad (5.4)$$

β as defined in Eq. 5.4 is a measure of the *spatial coherence* of the illuminating source. A β value of zero implies a spatially coherent source (i.e. plane wave illumination). For our particular case where δ is 19.6 nm, and W is 50 nm, our β value is 0.39.

Following exposure at the gap values of 0.17, 1.79, and 2.72 μm, the resist (PMMA) was developed, 5 nm of NiCr and 30 nm of Au were evaporated onto the substrate,

and the pattern was lifted off. Fig. 5-4 shows a result at the 2.72 μm gap. The pattern for the PRESTFET (interdigital fingers) was chosen for this experiment because it represented a more stringent test pattern than an isolated line. In addition, the pattern is mostly "open" (i.e. isolated, unexposed lines in an otherwise fully exposed field) which would serve to maximize any "proximity effects." As shown in Fig. 5-4, the pattern geometry was preserved even at the largest gap (2.72 μm).

Figure 5-5 plots the measured "finger" width following lift-off for the 0.17 and 2.72 μm gaps. For the case of the $p = 100$ nm pair, the width was averaged along the length of both fingers. The large error bars are due to the linewidth fluctuations in the mask, ragged edges due to lift-off, noise in the scanning electron microscope, etc. No systematic variation in finger width as a function of gap was detectable for either pitch pattern. Changes in measured finger width when the dose was changed by the factor of 2.3 at the 2.72 μm gap were within the error bars. No systematic trend was observed. This broad exposure latitude (factor of 2.3) indicates that the irradiance distribution at 2.72 μm gap is relatively steep and *not significantly degraded by diffraction.* Clearly, the effects of diffraction are not as deleterious as implied by earlier calculations [55].

The criterion we use for the maximum allowable gap, G, in proximity x-ray lithography is given by [49]

$$G = \alpha \frac{W^2}{\lambda} \tag{5.5}$$

where W is the minimum feature size, λ is the wavelength, and α is a coefficient (inverse of the Fresnel number squared). On the basis of experiments at visible and uv wavelengths, and calculations based on the Kirchhoff boundary conditions of abrupt apertures, it had been believed that α should not exceed 0.4 [49]. From the experiment described in this section, it is clear that α values of 1.44 and perhaps larger can be used and give reasonable exposure contrast.
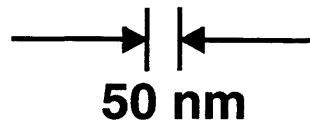
50 nm

Figure 5-4: Scanning-electron micrograph of a 100-nm-pitch interdigital electrode pattern ($\sim$ 50 nm nominal linewidth, W) exposed using a 1.32-nm-wavelength x-ray and a mask-to-substrate gap of 2.72 μm. This corresponds to $\alpha = 1.44$ in the expression $G = \alpha W^2/\lambda$, and a β value of 0.39.
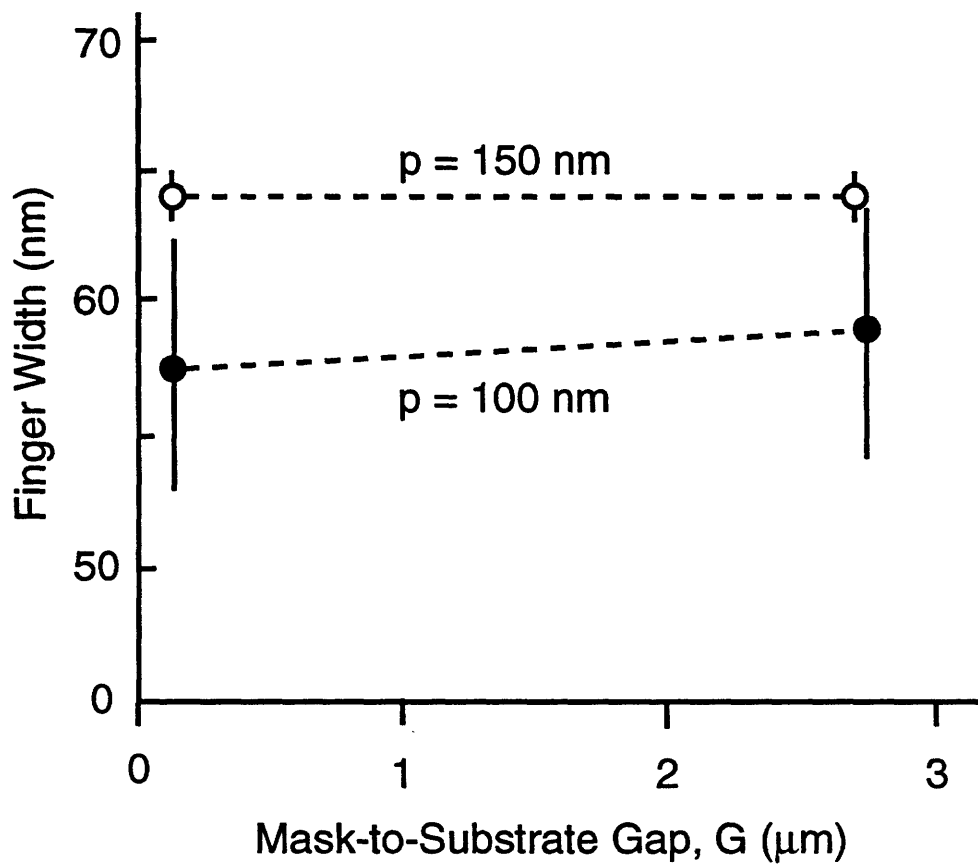
Figure 5-5: Plot of the measured average "finger" width following lift-off vs. mask-to-substrate gap, G, for two pitches, p, of 100 and 150 nm. The large error bars for the $p = 100$ nm patterns include several sources of error (e.g. fluctuations in width along the length of fingers in the mask, ragged edges due to lift-off, SEM noise, etc.). Changes in finger width due to a change in dose of a factor of 2.3 were within the error bars.

5.1.3 Discussion of Diffraction Experiment

Having demonstrated the disparity between the results of previous diffraction calculations and our experimental results, the following explanations are offered. Previous calculations used the Kirchhoff boundary condition and assumed that the x-ray absorber is much thinner than the wavelength [55]. That is, they assumed that the field amplitude immediately "downstream" of the absorber makes an abrupt transition from zero to a maximum value. Such a field distribution contains a significant contribution from high spatial frequencies and hence, according to the theory of the angular spectrum of plane waves [56], radiation is diffracted at large angles. Those assumptions are inapplicable [57]. An x-ray absorber is a lossy dielectric (index of refraction $N = 0.998 + j0.0012$ for Au at 1.32 nm wavelength [58]. We used 200 nm of Au, which is 151 wavelengths thick, gives 9.9 dB attenuation and a phase shift of 2.25 radians (129°). Thus, the absorber can be modeled as a lossy dielectric waveguide with a very small ($\sim$ 2 parts per 1000) refractive index discontinuity. As a result, the high spatial frequencies predicted by previous analysis [55] should be absent.

Secondly, the x-ray source used in our experiment was partially coherent ($\beta = 0.39$). In the calculations of Lin, the illuminating source was spatially coherent ($\beta = 0$). It is well known that illumination of an absorber pattern with a spatially coherent source leads to dips and bumps in the image (i.e. "ringing"), thereby lowering the contrast of the exposed pattern. If the source is made partially coherent, as in our experiment, these spurious effects disappear.

Recent modeling has shown that the contrast of the image can actually be optimized by selecting the proper degree of spatial incoherence in the illuminating source [54]. This modeling program, developed by Hector *et al.*, employs the full vector form of Maxwell's equation and runs on a workstation. The program allows for variation of the spatial coherence of the source. Such calculation power enables the user to predict the image of the exposure at the resist plane and is a powerful tool for x-ray mask replication.

5.2 Mask Replication

5.2.1 X-ray lithography

The x-ray masks generated by e-beam or focused-ion-beam lithography (parent masks) can be replicated using x-ray lithography to yield copy or "daughter" masks. The purpose of the replication is to minimize the risk to the parent mask by removing it from everyday use. A single parent mask can be replicated multiple times to yield numerous daughter masks. Some consequences of the mask replication process include: (1) pattern polarity reversal if positive resist is used for patterning both the parent and daughter mask, and (2) handedness reversal. For most of the work that we do (where lift-off of metal gate patterns are required), the polarity and handedness of the daughter mask are compatible with exposure onto substrates if positive resist is used for the parent mask, daughter mask, and substrate. If either the polarity or handedness of the daughter is not as desired, an additional replication may be necessary (i.e. grand-daughter mask) or negative resist may be employed.

Mask replication can be performed in contact, or in proximity using a microgap scheme [59]. For parent masks with minimum-feature linewidths larger than 100 nm, microgap replication is typically used. The effect of the gap on the areal image can be simulated using calculation programs [54]. Fig. 5-6 shows the configuration of a typical mask replication using a microgap configuration. The gap between the parent mask and the daughter mask blank is set by a group of equispaced Al studs, 350 μm in diameter, stencil-evaporated onto the mesa of the parent mask. For parent masks with minimum-feature linewidths below 100 nm vacuum-contact replication is preferred. The vacuum-contact and microgap configurations are identical, except that for vacuum contact, a partial pressure is applied between the two membranes, bringing them closer than the stud height. bringin

After the gap has been set, either by the studs in a microgap configuration, or by the vacuum in a contact configuration, the value of the gap can be measured using a monochromatic light source by counting the number of fringes, n, which move past

76

Cu$_L$ x-rays

parent mask

Al stud

gap, G

daughter mask
blank

WC930204.13
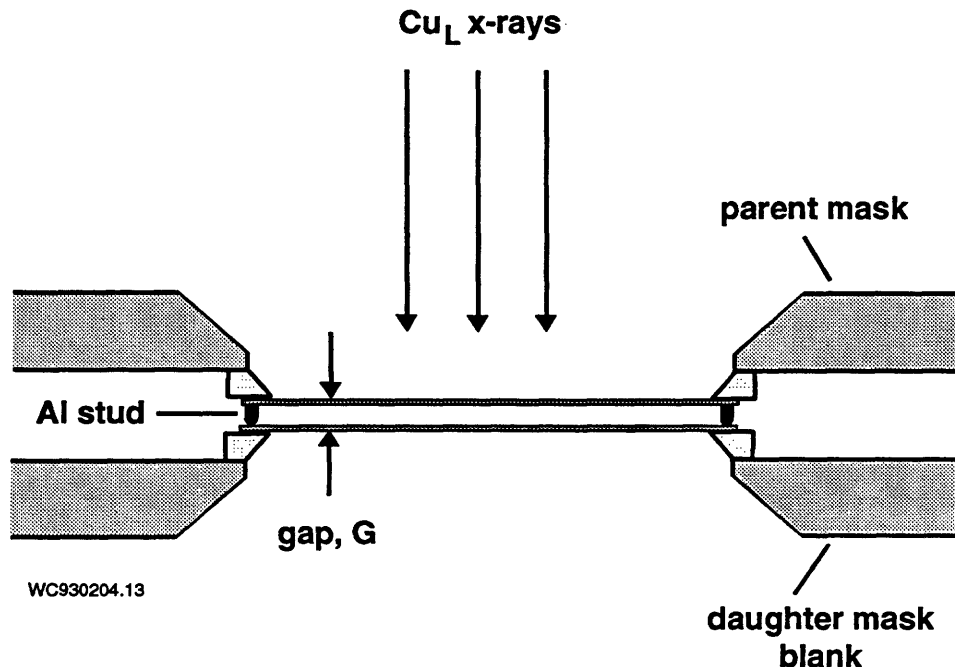
Figure 5-6: Schematic showing the typical daughter mask replication procedure. A set of six Al studs evaporated through a stencil set the gap of the exposure.

a particular point on the membrane as the observer moves from a position directly above the membrane ($\phi_0 = 0$) to a position at 45° from the normal ($\phi_0 = 45°$) where ϕ_0 is defined as in Fig. 5-7 [60]. If a sodium lamp ($\lambda = 0.589$ μm) is used, then the gap is n microns.

The x-ray exposure of the parent mask onto the daughter is performed using a water-cooled copper-target x-ray source ($\lambda = 1.32$ nm). Typical PMMA exposure times are roughly 24 hours at a mask-to-source distance of 23.3 cm (for an anode voltage of 8 kV and an anode current of 75 mA) in a vacuum environment used for the microgap exposures. This corresponds to a required exposure time of 12.7 hours at a mask-to-source distance of 12 cm (again, 8 kV anode voltage, 75 mA anode current) in the helium environment (with a 1 μm-thick SiN$_x$ vacuum window) used for contact exposures. After the daughter blank is x-ray exposed, and with the center membrane area covered, it is flood-exposed with a deep-UV (220 nm) lightsource. The purpose of the deep-UV exposure is to remove (after development) the PMMA in the regions outside of the membrane (x-ray exposed) region so that the area to

SODIUM LAMP

EYE

ϕ_0
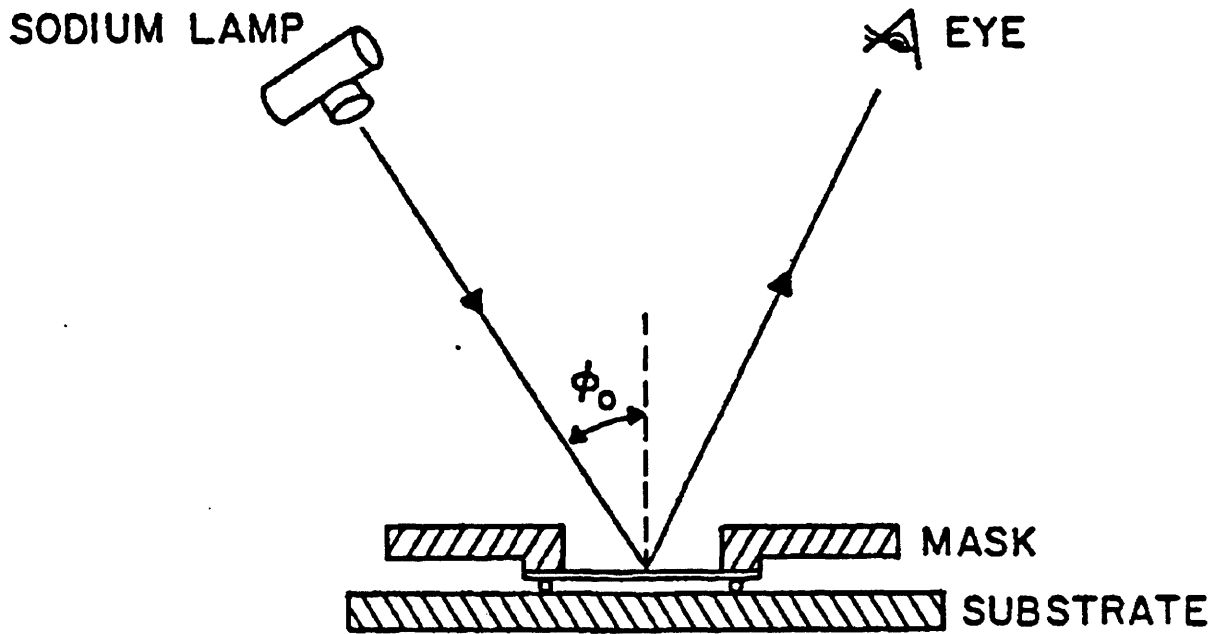
MASK

SUBSTRATE

Figure 5-7: The gap between a mask and substrate (in our case, the substrate is the daughter mask blank) at any point can be determined by counting the number of fringes, n, which move past that point as the observer moves from $\phi_0 = 0$ to $\phi_0 = 45$. The gap is then n microns.

be plated is fixed, and easily calculated. The zero-stress plating-current density (see Chapter 4) multiplied by this calculated area gives us the current that will be used for plating.

5.2.2 Development

Care must be taken in the development of the x-ray exposed daughter mask. Some problems may occur if the linewidth of the exposed resist pattern is small (< 100 nm), or if the aspect ratio (resist height-to-linewidth ratio) is large ($> 5:1$). These problems are illustrated in Fig. 5-8.

For fine-linewidth patterns, the developed resist may lose adhesion to the Au plating base as is shown in Fig. 5-8(b). This occurs because the area of the resist actually contacting the plating base is small due to the fine linewidth, and because polymeric materials such as PMMA do not adhere well to Au anyway. This problem can be easily solved by treating the surface of the Au with an adhesion promoter. The

78

adhesion promoter we use is trimethylsilylacetamide (TMSA) sold commercially by MicroSi, Inc. as MS805 [61]. This adhesion promoter bonds the resist to Au using a complexation or chemisorption mechanism [62]. The MS805 comes in liquid form and is spin-coated (5 krpm for 30 s) onto the plating base immediately before spinning the PMMA. A thin layer of the adhesion promoter (< 3 nm-thick) remains on the plating base after development of the resist and must be removed prior to plating.

For resist structures with high aspect ratios, mechanical stability may be a problem (see Fig. 5-8(c)) even if the adhesion of the resist to the plating base is good (i.e. even if an adhesion promoter is used). This may occur because the surface tension of a receding liquid developer or rinse may force the tall resist lines to bend or fall over. The solution to this problem is what we refer to as "wet processing". The main idea of wet processing is to keep the mask completely immersed in liquid from the time it enters the developer to the time it is is plated in the plating bath. To accomplish this, the mask is developed in a beaker of 1:2 MIBK:IPA, transferred to a beaker of IPA which rinses away the developer, and then transferred to a beaker of DI water which rinses away the IPA. Care is taken to ensure that the transfer between beakers is quick so that liquid is not allowed to recede from the mask. After making sure that the IPA is completely washed away by the DI water rinse, the thin adhesion promoting layer is removed by quickly transferring the mask from the DI rinse beaker to a beaker of a 1:3 buffered HF:DI water solution, again making sure that the water does not recede during transfer. After 10 sec. in the diluted buffered HF solution, the mask is transferred to a running DI water rinse beaker. After making sure that the mask is sufficiently washed, the mask is then transferred to the plating bath where plating is then performed (see Chapter 4 and Appendix C for plating details).

For masks that have only coarse-linewidth features and low-aspect-ratio resist structures, "dry processing" may be used. In the dry process, the development and rinse is the same as in the wet process, but after the IPA rinse, the sample is blown dry with filtered N_2 gas. The advantage of dry processing is that the mask may be examined in an optical microscope after development and before plating. After examining the sample, a "de-scum" reactive-ion-etch is performed. The etch used

(a)

PMMA

liquid

plating base

(b)

Loss of resist
adhesion

(c)

Loss of resist
mechanical stability

WC930204.14
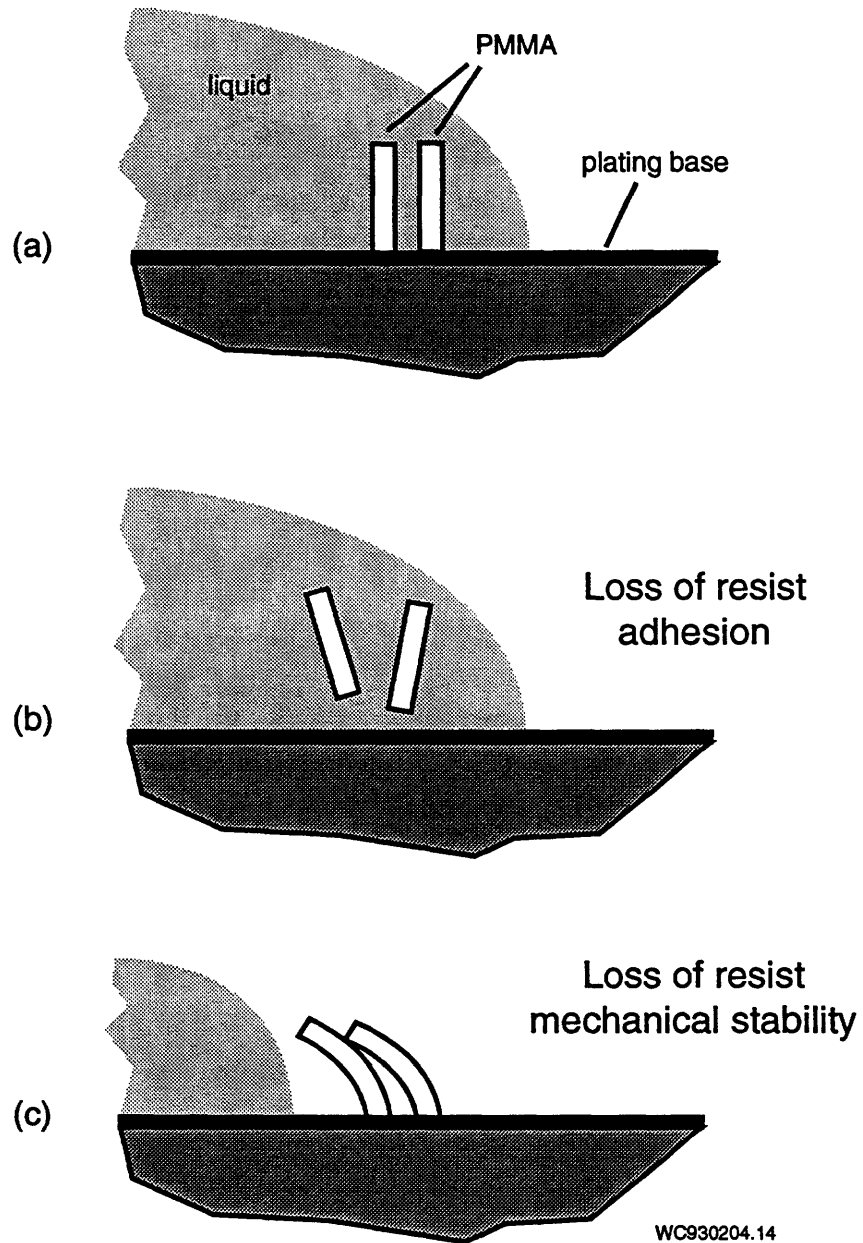
Figure 5-8: Schematic showing problems which may occur during development. (a) Resist-developer-plating base interface. (b) Loss of resist adhesion – this can be solved by using an adhesion promoter (MicroSi MS805). (c) Loss of resist mechanical stability – this is caused by the surface tension of receding liquid (e.g developer or rinse solution) and can be solved by using the "wet development" technique described in the text.

depends on whether or not MS805 adhesion promoter was used. If the MS805 was used, the etch parameters are: 12 sccm O_2, 18 sccm CF_4, 10 mtorr pressure, 400 V bias, and 0.13 W/cm^2 power density. If no adhesion promoter was used, the etch parameters are 15 sccm O_2, 10 mtorr pressure, 400 V bias, and 0.13 W/cm^2 power density, and 8 sec. etch time. After the de-scum etch, the sample is plated with Au.

Once the daughter masks are plated with Au, the PMMA, used as the mold for plating, is no longer needed, and is stripped using O_2 plasma etching. We then spin 400 nm-thick polyimide on the front of the mask. The polyimide serves two functions: (1) to encapsulated and protect the absorber features, and (2) to prevent shorting to the substrate during electrostatic contact in the alignment procedure (described in the next section)

5.3   Alignment and Exposure of Devices

An alignment and exposure system developed for x-ray nanolithography by Moel *et al.* [63] has been adapted for use with small substrates. This alignment and exposure system is shown schematically in Fig. 5-9. The system consists of a Cu_L x-ray source ($\lambda = 1.32$ nm) and an exposure chamber filled with 1 atm of helium. The exposure chamber is separated from the vacuum chamber housing the x-ray source by a 2-cm-diam window of 1-2 μm-thick SiN_x. The alignment system consists of a mask holder, piezoelectrically driven X, Y and Θ stages, and a 0.1 μm resolution motor-driven Z stage to set the mask-to-wafer gap. The mask-to-wafer alignment is performed using a 20 ×, 0.4 NA brightfield objective coupled to a CCD camera. The alignment stage is shown in Fig 5-10.

In addition, special procedures have been developed for working with substrates that are smaller than the diameter of the x-ray mask membrane (31 mm). This is essential for work on quantum-effect devices, where high-mobility substrate material is precious and small substrate pieces are common. The strategy for alignment and x-ray exposure of these small substrates is shown in Fig. 5-11. The procedure is:

X-ray Alignment and Exposure System
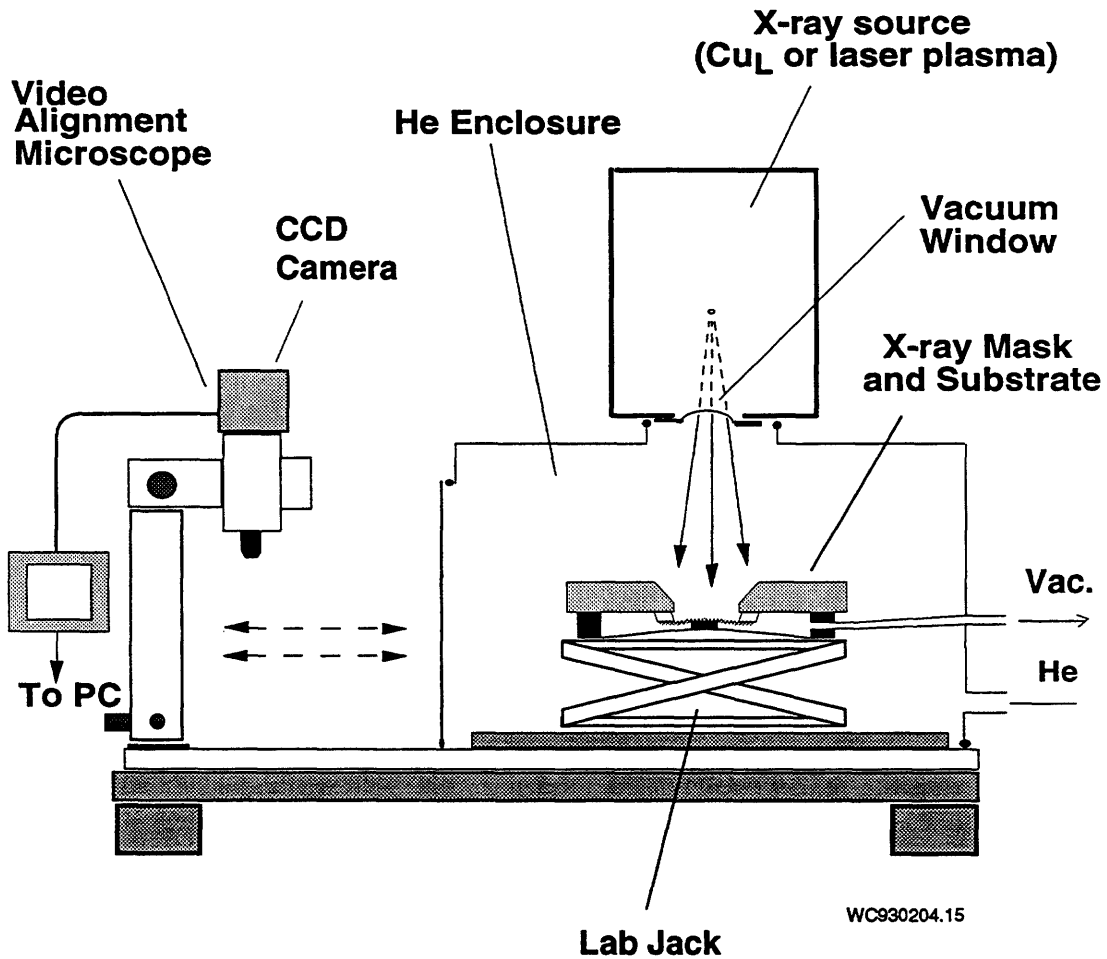
Figure 5-9: X-ray mask alignment and exposure system, developed by Moel *et al.* [63], configured for exposure of small substrates. An alignment system, shown in Fig. 5-10, is used to align masks to substrates. The exposure is performed in a He-filled box.
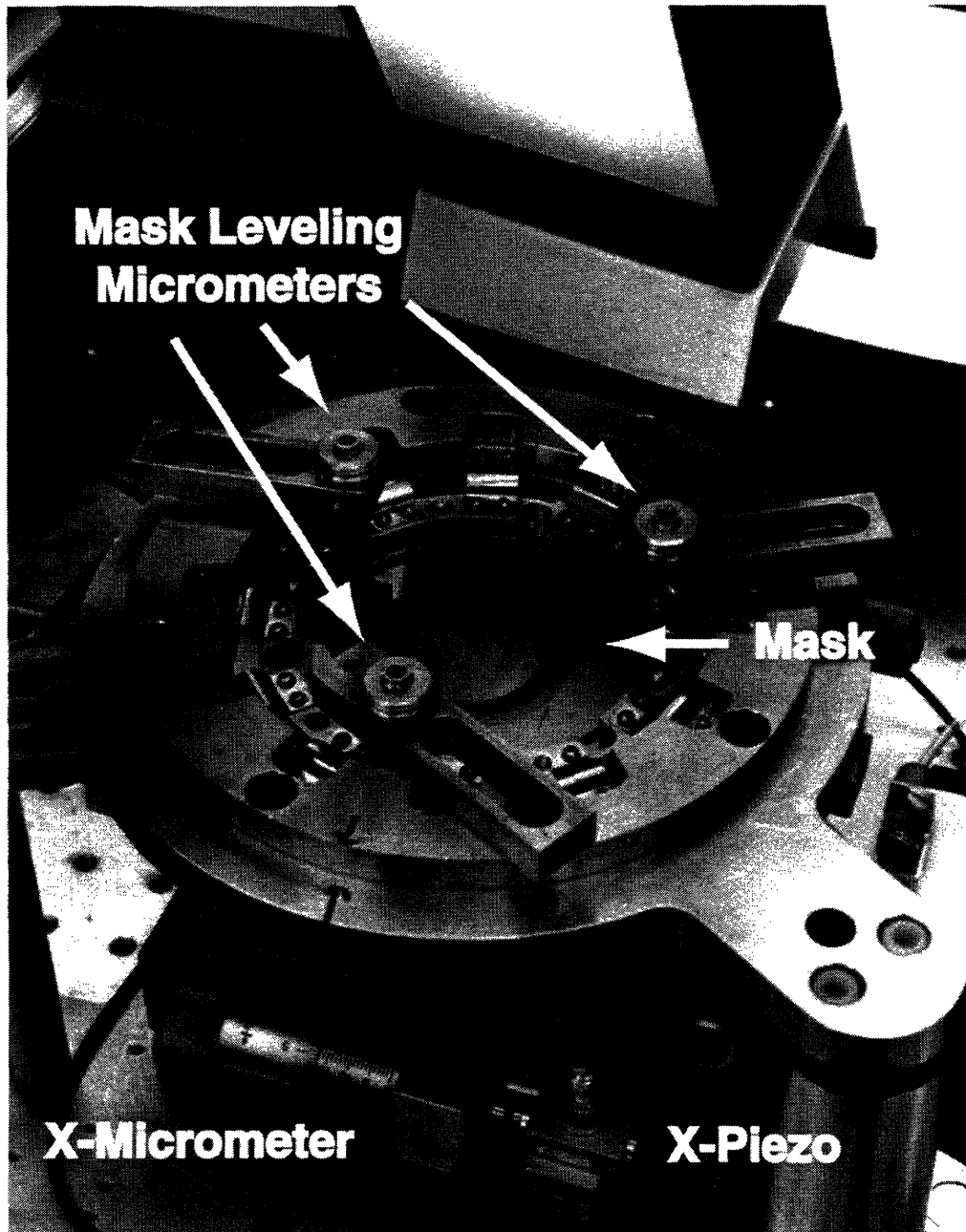
WC920929.2

Figure 5-10: X-ray mask alignment system. The mask is planarized to the substrate using the leveling micrometers. Coarse positioning of the substrate is accomplished using X, Y, and Θ-micrometers. Fine positioning is accomplished with X and Y piezoelectric elements. The Z-position is adjusted using a motor-driven stage with 0.1 μm resolution.

(1) planarization of mask and substrate, (2) alignment, (3) electrostatic contact, (4) transport to a conformable mask fixture, shown in Fig. 5-12 and (4) exposure in the He enclosure. This procedure of alignment and contact x-ray exposure onto substrates smaller than the mask membrane diameter has not been done previously, and is described in detail in the next section

5.3.1   Alignment

Before alignment can proceed, the mask and substrate must be planarized with respect to one another. This is achieved by placing an x-ray mask blank (unpatterned) in the mask holder, looking at the interference fringes (from a monochromatic light source) in the region between the substrate and the mask, and adjusting the mask leveling micrometers until the number of fringes is a minimum. It is important that the substrate is within the coherence length of the "monochromatic" source from the mask blank; otherwise, no fringes will be observed. This is accomplished by raising the substrate with the Z-stage of the aligner. The clear mask blank is then removed and replaced with the actual daughter mask. Because the dimensional variation between masks is small, the daughter mask is coplanar with respect to the substrate. Only minor adjustments need be made at this point. The substrate, is then raised until one corner touches the mask. The leveling micrometers are adjusted until all four corners touch the mask. Contacting of the mask to the substrate in this way does not damage or adversely affect either, despite repeated contact. At this point the substrate is lowered so that it no longer touches the mask, and alignment is carried out.

We align using alignment marks similar to those commonly used in optical lithography, and easily achieve submicron overlay. The job of alignment can be made easier if border frames around each die are patterned on the original parent mask [64]. The borders on the x-ray mask are designed to overlay onto borders on the substrate (patterned using optical lithography). Once the borders are aligned to one another, (a relatively easy task) Θ alignment is essentially complete.

Alignment Scheme

1. Align

Mask
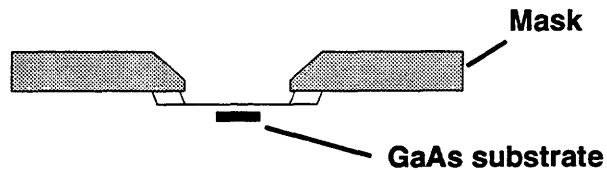
GaAs substrate

2. Electrostatic Contact

After electrostatic contact is established, mask
and substrate adhere. Mask and susbtrate are
transported to conformable-mask fixture.

3. Conformable mask fixture

O-ring

Polypropylene backing

Vacuum line
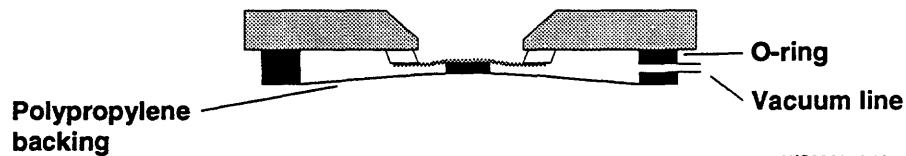
WC930204.16

Figure 5-11: Mask alignment procedure. After planarization using a clear test mask,
the real mask is placed in and the substrate is aligned to the mask patterns. After
alignment, a voltage is applied between the plating base of the mask and the substrate,
whereupon the the mask and substrate come into intimate contact. This contact
remains even when the voltage is off, presumably due to van der Waals attraction.
The mask and substrate are transported to the vacuum conformable mask fixture
which keeps the two in contact during the exposure.

X-ray Mask Holder

SiN$_x$ membrane — Pyrex frame

GaAs sample — Sealing-ring

Polypropylene backing — Vacuum line

WC930204.17
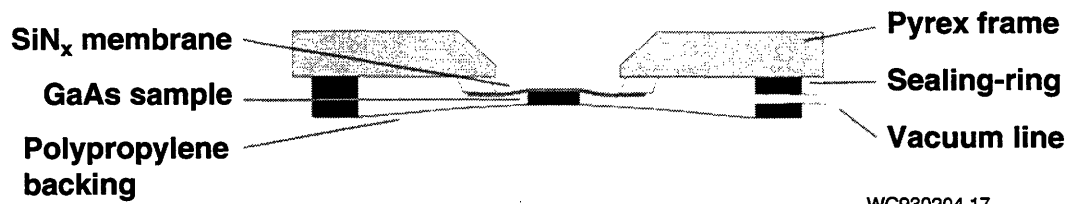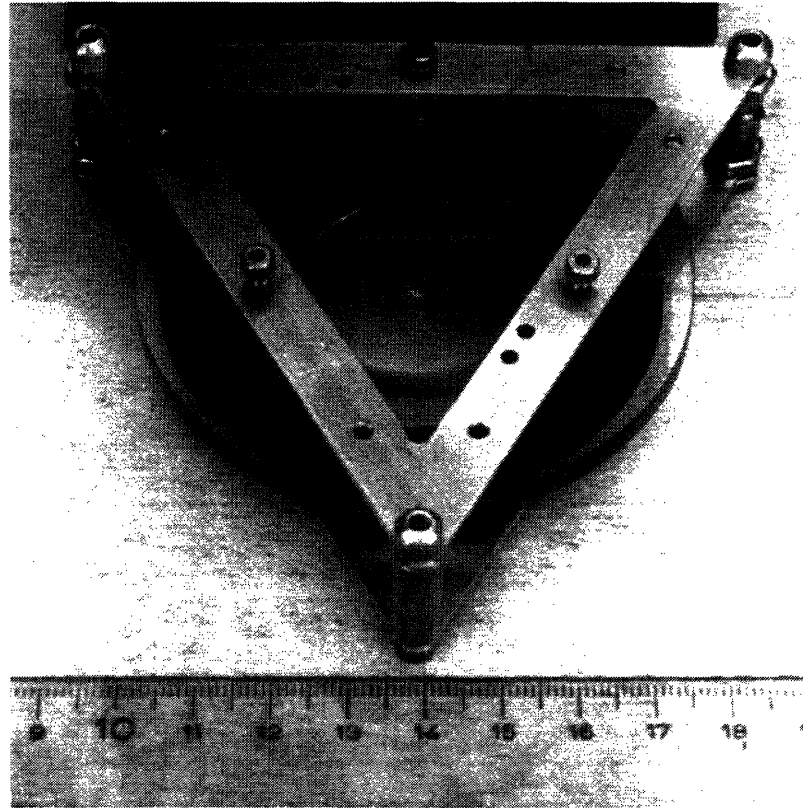
Figure 5-12: Conformable mask fixture which uses partial vacuum to maintain mask-to-substrate contact during x-ray exposure.

Once alignment is achieved, the substrate is raised so that it gently touches the mask. A voltage is then applied between the plating base on the front of the mask and the substrate, bringing the two into intimate contact. The purpose of the electrostatic contact is to allow the transport of the mask and substrate from the alignment tool to remote exposure tools without loss of alignment. The amount of voltage required to bring the two into contact depends on a number of factors such as the conductivity of the substrate and the number and size of dust particles on the substrate, but typically 50 to 100 V is enough to bring the mask into contact with the substrate. The encapsulating polyimide on the front of the mask prevents shorting between the two electrodes and also protects the Au absorber from any mechanical damage.

Once electrostatic contact is achieved, the mask and substrate remain in contact even after the voltage is removed, presumably due to van der Waals forces. While the two remain adhering to one another, we transport them to a specially-designed conformable mask fixture that keeps the two together in contact during x-ray exposure [35]. This fixture, as shown in Fig. 5-12 uses a partial vacuum to keep the mask and substrate in contact during the x-ray exposure. Previous experiments showed that without the vacuum the sample and mask simply came apart, presumably due to the evolution of gaseous byproducts during the exposure of the PMMA on the substrate. The vacuum is controlled with a pressure regulator to 100 Torr below atmospheric pressure. The vacuum fixture causes the mask to conform to the substrate, over dust particles and edge-resist build-up. The gap between mask and substrate after vacuum is applied on the fixture is estimated to be no more than 1 μm based upon the depth-of-focus measurements using a microscope objective.

After the mask and sample are loaded into the conformable mask fixture, the fixture is moved into the exposure chamber in close proximity ($\sim$ 4 cm) to the nitride vacuum window, as shown schematically in Fig. 5-9. The chamber is then sealed, and He is flowed through the chamber. A detector measures the concentration of oxygen in the chamber. A low oxygen content is necessary since oxygen molecules have a strong absorption at the 1.32 nm x-ray wavelength we use for exposure. A value of 400 ppm oxygen or below is required before exposure can begin.

Once the exposure is completed, the sample can be easily removed from the mask with the use of a vacuum wand. There is no observed adhesion or charging between the mask and the substrate. The substrate is developed in a solution of 1:2 MIBK:IPA by inspection. Following development and rinse in IPA, the samples are cleaned for 1 min. in UV ozone in order to completely remove any residual organics at the surface of the substrate. For those samples where gate metallization is required, a Ti/Au evaporation is then performed. Lift-off using heated acetone removes the metal over the PMMA and strips the PMMA at the same time. The devices are then ready for wire bonding and measurement.

Chapter 6

Device Results

The motivation for the work described in the previous five chapters was to develop a technology for the fabrication of quantum-effect devices. The devices fabricated using this technology include electron waveguides in GaAs, the planar resonant-tunneling field-effect transistor (PRESTFET), and multiple parallel quasi-one-dimensional conductors in GaAs. The following sections describe the results from the electron-waveguide devices and the PRESTFET.

6.1   Electron Waveguide

6.1.1   Device Description

A split-gate scheme, as shown in Fig. 6-1, can be used to create a one-dimensional (1D) channel at the heterointerface of a high-mobility modulation-doped GaAs/AlGaAs structure. By applying a negative gate bias to the split-gate, we can deplete the two-dimensional electron gas (2DEG) underneath the gates, leaving a narrow channel in between, as depicted by the shading in Fig. 6-1. Two ohmic contacts allow access to the input and output of the channel. If the electrons travel through the channel without scattering, then the channel is a true electron waveguide.

In an electron waveguide, distinct modes will arise due to the waveguide boundaries as shown in Fig. 6-2. One can think of these modes in a more "electronic" sense

Electron Waveguide Device
(Schematic)
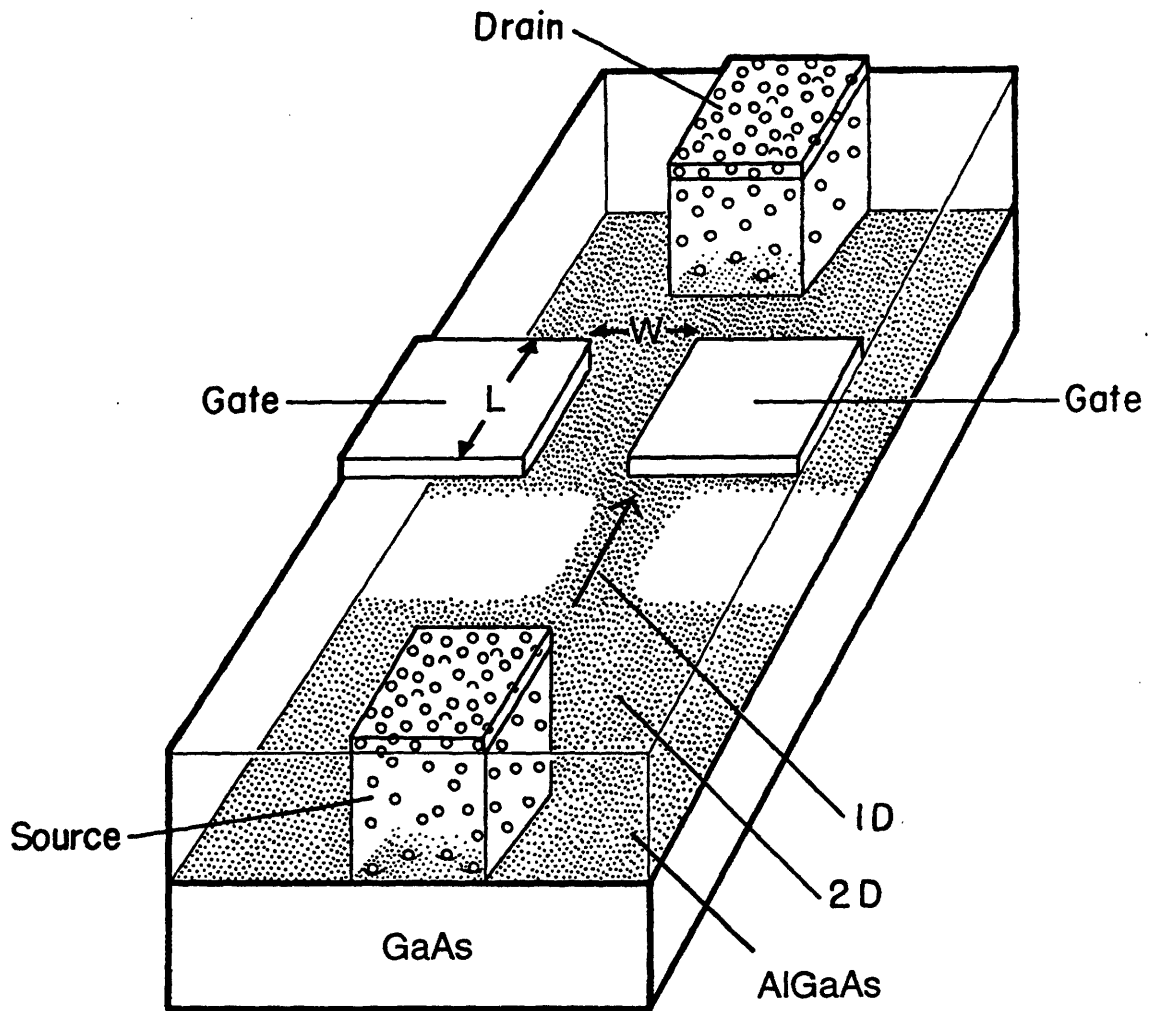
WC930204.18

Figure 6-1: Schematic of an electron waveguide device showing the two-dimensional electron gas (shaded region) at the AlGaAs/GaAs interface constricted by the gate electrodes above. The waveguide has a length L and a width W.

as the 1D subbands. The contribution to the conductance of each subband is simply $2e^2/h$ [65, 66]. This results from the cancellation of the energy dependence in the product of the 1D density of states and the electron velocity. Therefore, the total conductance of the waveguide is simply the summation of all the $2e^2/h$ contributions of the subbands below the Fermi level.

The unique aspect of a split-gate scheme is that we can deplete, and eventually pinch off, the 1D channel through the fringing fields of the gates. We can, therefore, sweep the 1D subbands through the Fermi level by modulating the split-gate bias. Each time a subband is swept through the Fermi level, the conductance changes by $2e^2/h$, with the result that a "staircase" structure appears in the I-V_{GS} characteristics [65, 66].

6.1.2 Fabrication and Measurement

Fabrication of the devices began with molecular-beam-epitaxial (MBE) growth of an AlGaAs/GaAs modulation-doped heterostructure [67] . The mobility of the 2DEG was 300,000 cm^2/V-sec and the carrier concentration was 2.9×10^{11} cm^{-2}, both measured at T = 4.2 K. The depth of the 2DEG from the surface was 89 nm. Mesa isolation, ohmic contacts, and gate pads were all accomplished using optical lithography [68]. The split-gate structures used to implement the electron waveguides were fabricated by x-ray lithography using the process described in Chapter 5 for x-ray lithography on small substrates. A top-view scanning-electron micrograph of the x-ray mask for a 0.1 μm-long waveguide is shown in Fig. 6-3.

After x-ray lithography, a Ti/Au film was evaporated and lifted off to form the split gates. With direct write e-beam lithography, only thin metal films (50 nm or less) can be lifted off because of the thin resist (typically less than 100 nm) used for exposure. Because of the absence of deleterious proximity effects in x-ray lithography, we were not limited in the thickness of resist we could use, and hence were free to increase the metal thickness. We used 300 nm of PMMA resist and lifted off 20 nm of Ti and 120 nm of Au. Thicker metal patterns are more robust (important during

Energy Diagram
for
Electron Waveguide Device

$\longleftarrow$ W $\longrightarrow$

L

Gate   **Gate**

$2e^2/h$ — E_2

E_F

$2e^2/h$ — E_1

Conductance per mode
$= 2e^2/h$

WC930204.19
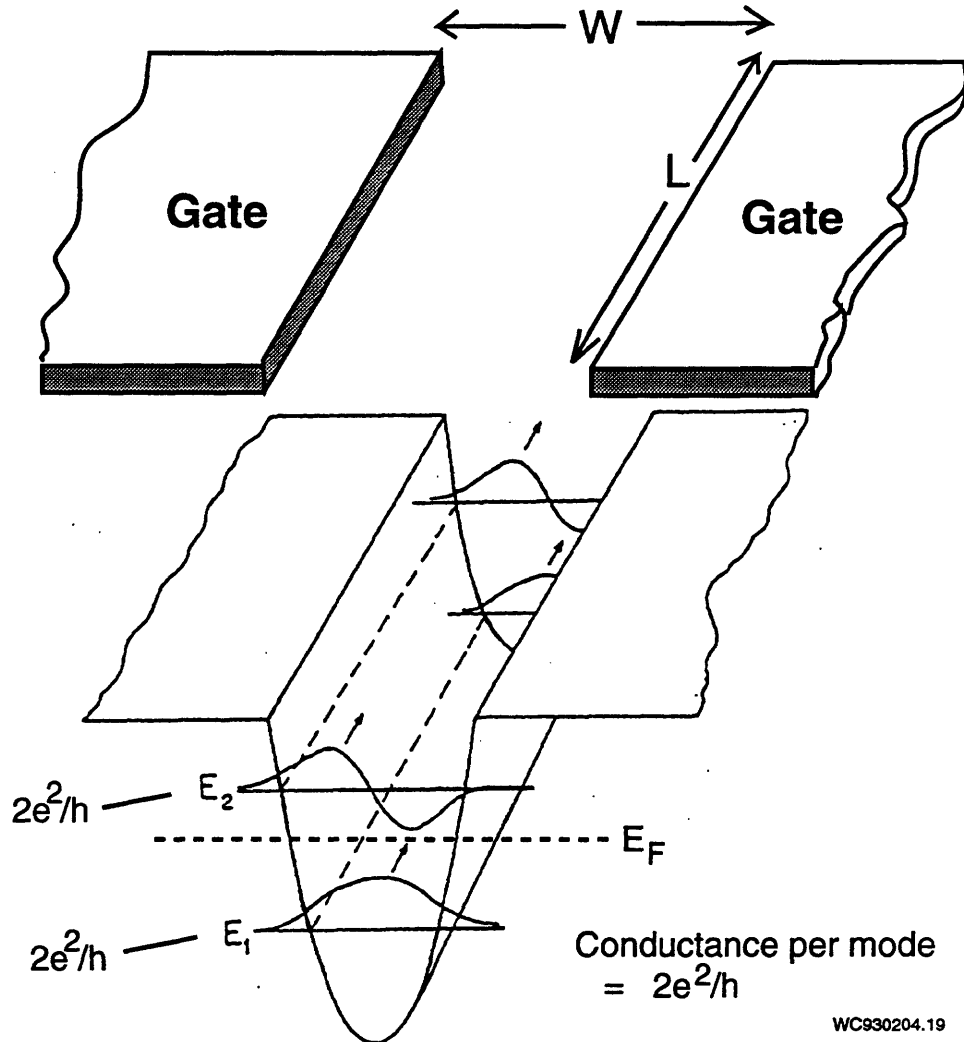
Figure 6-2: Energy diagram of an electron waveguide. If the electron gas is truly "one-dimensional," (i.e. quantized energy levels) and ballistic (i.e. no scattering) throughout the channel of length L, then the device behaves like a true waveguide in the sense that distinct modes of travel are allowed. Each occupied mode (those below E_F) contributes $2e^2/h$ to the conductance.

**Top View of X-ray Mask
(100 nm-long waveguide).
Mask written by e-beam lithography at NRL.**
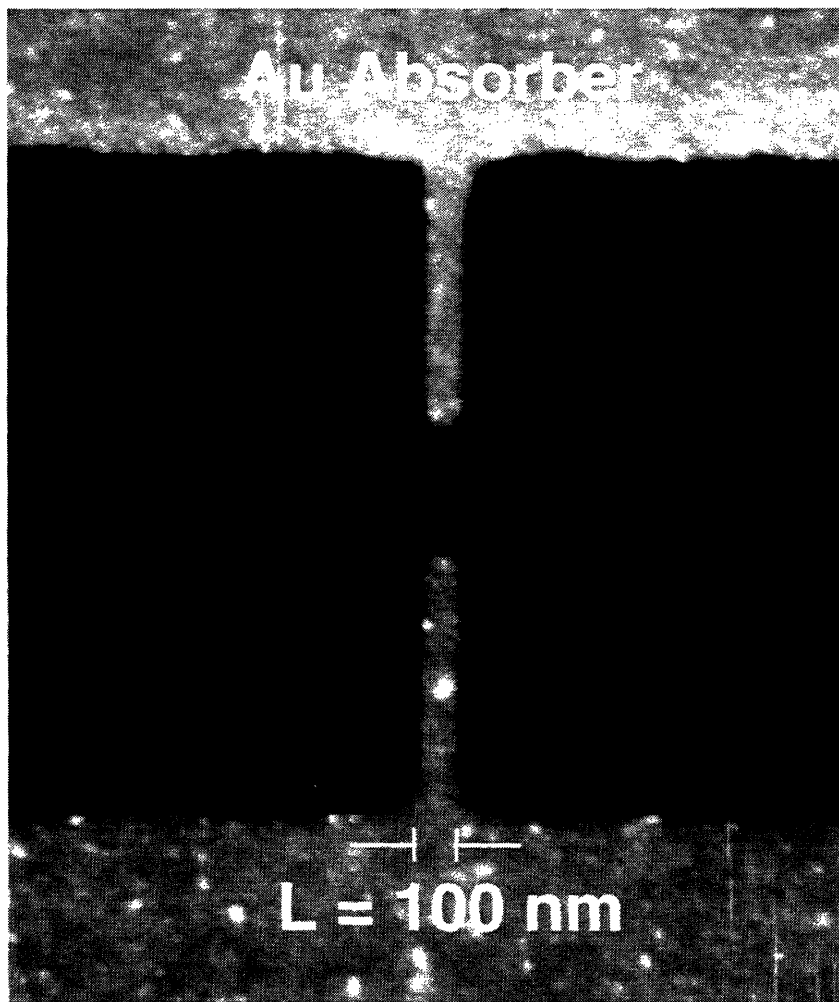
WC930204.20

Figure 6-3: Top-view scanning-electron micrograph of the x-ray mask pattern for a
0.1 μm-long waveguide device.

the processing and wire bonding steps) and exhibit better step coverage than thin metal films. After liftoff, two-probe measurements of the waveguide devices were carried out at liquid helium temperatures [69]. A small AC drain-source bias of 100 μV was applied between the two ohmic contacts. The source current I_S was fed into a current/voltage preamplifier whose output was monitored with a PAR 5210 lock-in amplifier. The split-gate voltage V_{GS} was controlled with an HP 4145B.

The plot of the conductance (I_S divided by the drain voltage) of two waveguide devices of length 0.2 and 0.75 μm are shown in (Fig. 6-4a) and (Fig. 6-4b), respectively. For both devices, sharp $2e^2/h$ steps confirm the existence of clean, ballistic electron waveguides. This is quite a remarkable result for the 0.75-μm-long device. The deviation from the $2e^2/h$ values for the higher lying conductance steps is a consequence of the two-terminal measurement technique. The conductance steps are clearly visible up to temperatures of 15 K. At higher temperatures, thermal broadening is comparable to the subband spacing and we are no longer able to resolve the individual levels. The relatively low conductance at $V_{GS} = 0$ V is due to a slight unintentional etch of the semiconductor that occurred during the cleaning process before the gate metal evaporation. As a result of this etching, the 2DEG is turned off directly underneath the gates even at zero bias. The observation of conductance quantization in waveguide devices as long as 0.75 μm is a consequence of a high-mobility 2DEG and the ability of x-ray lithography to preserve this high mobility [15].

6.2 PRESTFET

The idea of a PRESTFET structure was first suggested independently by Ismail [70] and Chou [71] and was realized experimentally by Ismail using direct-write e-beam lithography [70]. The device, as depicted in Fig 6-5, consists of a set of fine-linewidth and closely spaced pair of Schottky-gate fingers patterned on top of a conventional modulation-doped GaAs/AlGas structure where the 2DEG is 55 nm from the surface. If the gates are appropriately biased, and if the gate fingers are in close proximity to one another, quantized energy states can exist in a potential well between two

Conductance Quantization of Electron Waveguides at T = 1.6 K as a Function of Split-Gate Voltage

(a)

(b)

WC930204.21
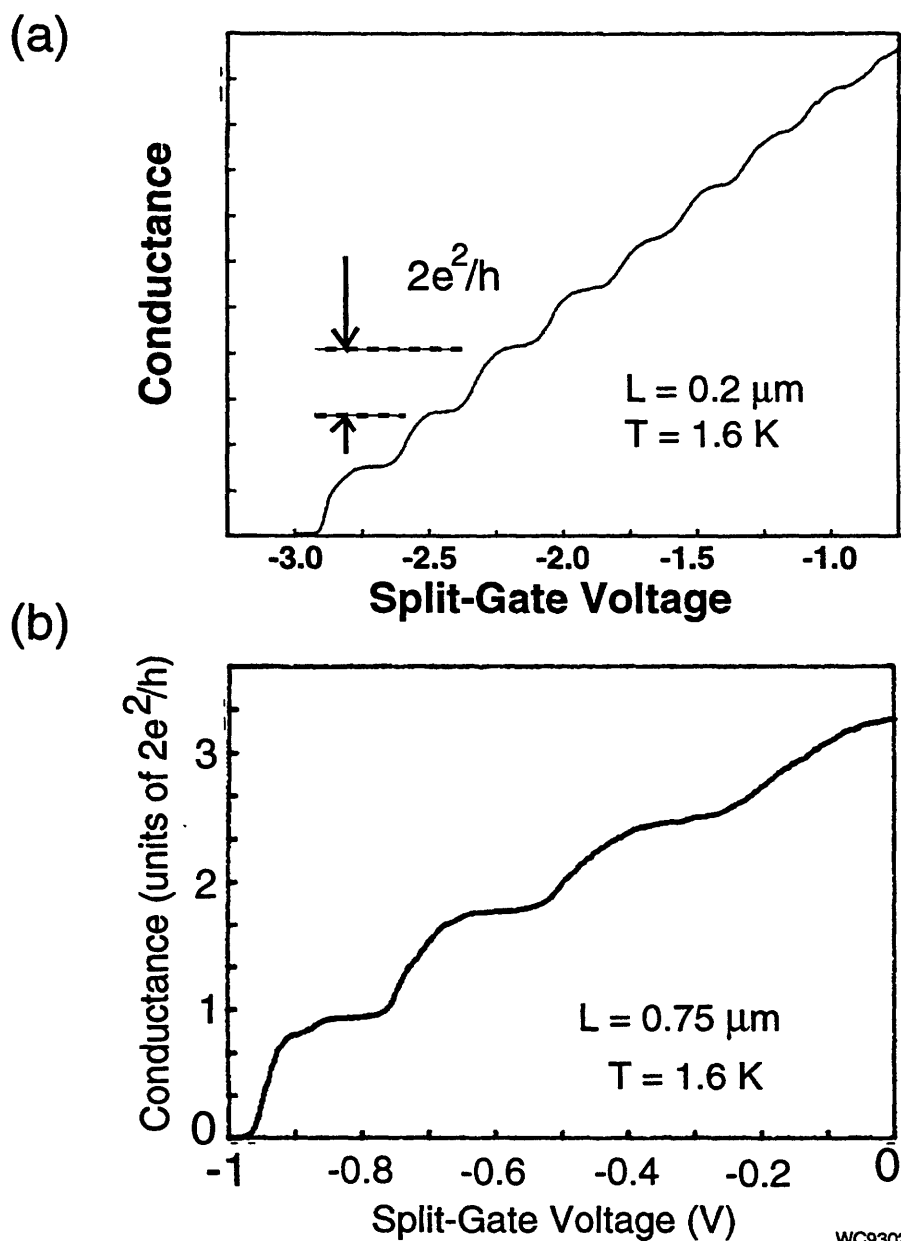
Figure 6-4: Conductance quantization for electron waveguides of length (a) 0.2 μm and (b) 0.75 μm. The units of quantization are $2e^2/h$.

Planar Resonant-Tunneling Field-Effect Transistor (PRESTFET)

(a) Device schematic

mesa-etched GaAs/AlGaAs
modulation-doped heterostructure
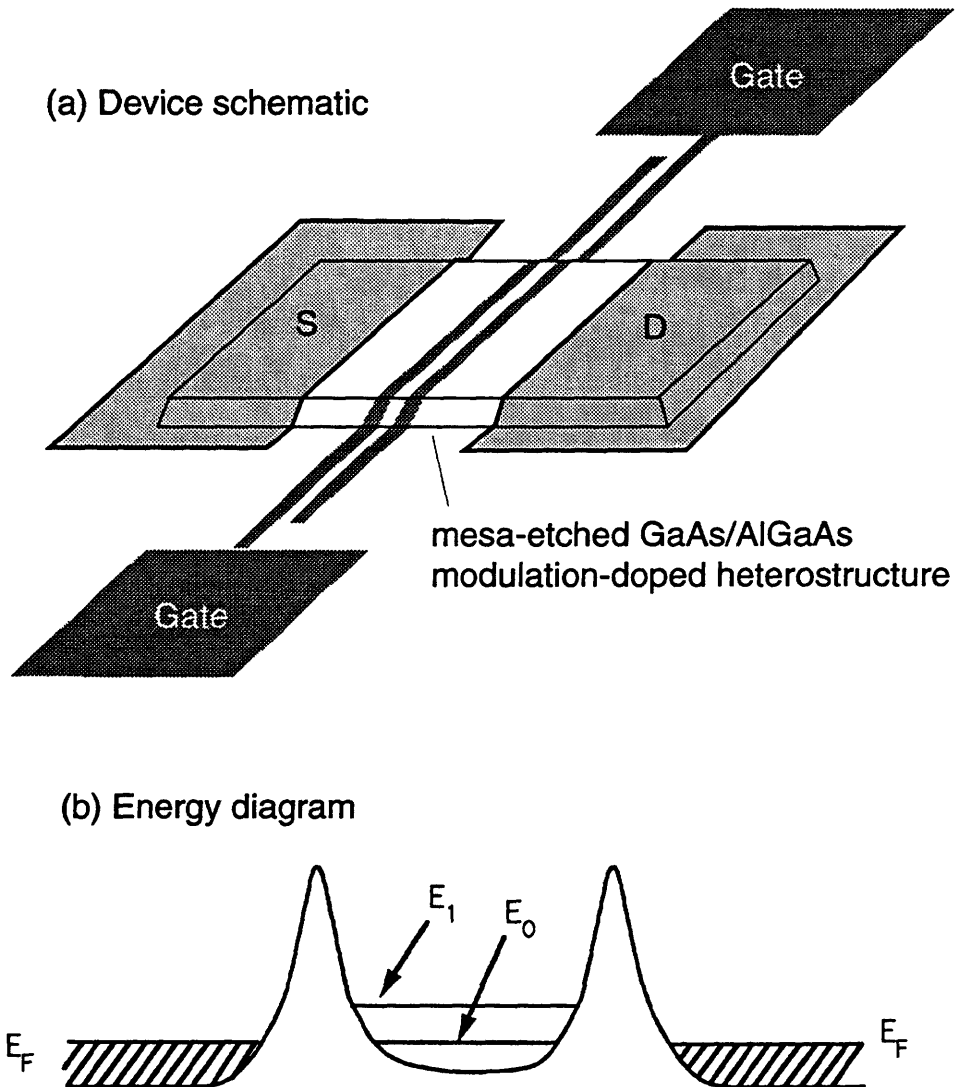
(b) Energy diagram

Figure 6-5: (a) Schematic of a PRESFET device. The substrate is a GaAs/AlGaAs modulation-doped structure on top of which fine-linewidth, closely spaced gate electrodes are patterned. (a) The energy diagram in the 2DEG, 55 nm beneath the gate fingers. If the gates are appropriately biased, and if the gate fingers are in close proximity to one another, quantized energy states can exist in a well between the two electrostatic potential barriers. Under proper drain-source bias, resonant tunneling may occur.

electrostatic potential barriers. Under proper drain-source bias, resonant tunneling may occur [70]. The details of the device behavior is best summarized in the thesis by Ismail [72].

The fabrication of the PRESFET began with MBE growth. The mesa, ohmic contacts, and coarse-feature Schottky gates are defined by optical lithography and liftoff. The fine gate fingers are then patterned in PMMA using x-ray lithography. The x-ray level is aligned to the ohmic contact level using the techniques described in the previous chapter. After x-ray exposure and development of the PMMA, 70 nm of Ti/Au metal is e-beam evaporated and lifted off. Fig. 6-6 shows a finished PRESTFET device with 200-nm-pitch gate fingers (the linewidth of the gate finger is approximately 50 nm). The devices are then characterized at room temperature .

The first batch of PRESTFET devices were fabricated with only 200-nm-pitch devices. We are currently in the process of replicating a daughter mask with 150 and 100-nm-pitch devices as well. Some of the 200-nm-pitch devices exhibited independent gate control and normal transistor behavior at room temperature. Some of the other devices exhibited behavior indicative of broken gate fingers. Only those devices which exhibited proper behavior were wire bonded. These devices were then characterized at liquid-helium temperature (4.2 K).

We were unable to measure any device characteristics in the 200-nm-pitch devices that were indicative of resonant tunneling. This, we believe, is due to the large separation (150 nm in the 200-nm-pitch devices) between the gate fingers. As a rough estimate of the energy level spacings, consider the energy difference between the first and second energy levels in an infinite square well of 150-nm width. The energy spacing ΔE is given by

$$\Delta E = \frac{3\pi^2 \hbar^2}{2m^* L^2} \approx 0.75\,meV \tag{6.1}$$

This is comparable to the thermal energy spread kT at 4.2 K ($kT \approx 0.4\,meV$). A 100-nm-pitch device, with a well spacing of roughly 50 nm, would have an energy spacing nine times larger. We expect to see evidence of resonant-tunneling in such

PRESTFET
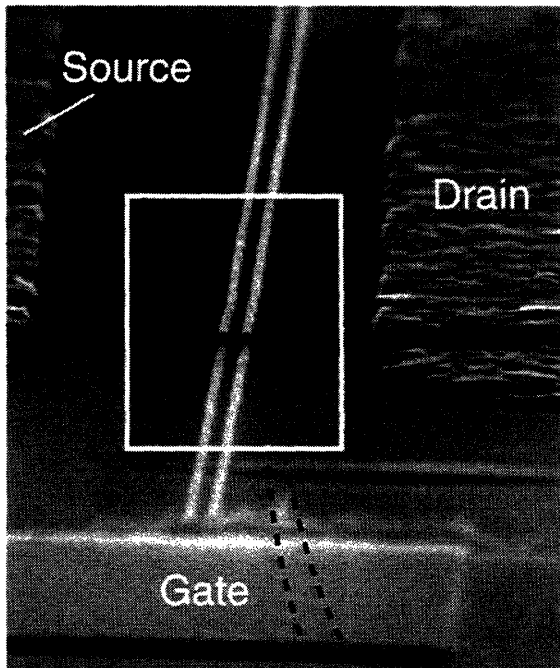
- Good step coverage over mesa edge (120 nm height)
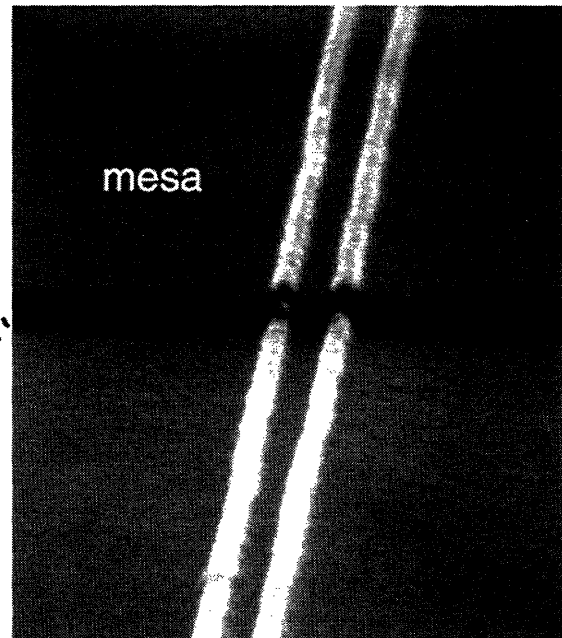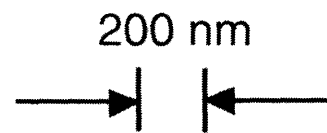
200 nm

- Gate lines 50 nm-linewidth, 70 nm-thickness

mesa

WC930204.23

Figure 6-6: Scanning electron micrograph of a finished PRESTFET device with 200-nm-pitch gate electrodes. The electrode linewidth is approximately 50 nm and the thickness of the metal is 70 nm. Note that the step coverage over the 120-nm-deep mesa etch is excellent.

devices, and it is anticipated that such devices will be made by x-ray lithography in the very near future.

Chapter 7

Summary and Future Work

The object of this dissertation has been to develop a mask technology for the exposure of quantum-effect devices using x-ray lithography. The advantages of x-ray lithography over other nanolithography techniques are numerous. These advantages include high resolution, absence of scattering (as opposed to electron scattering in e-beam lithography and standing waves in optical lithography), process robustness, large process latitude, and absence of substrate damage. In order to apply all of these advantages to the fabrication of devices, a technology has been developed to fabricate high-flatness x-ray mask membranes, pattern them using focused-ion-beam or electron-beam lithography, electroplate low-stress gold absorbers, replicate the masks using contact or microgap x-ray lithography, align and expose x-ray masks on substrates smaller than the diameter of the mask membrane. In addition, we measured and characterized the quantum-effect devices at cryogenic temperatures.

The x-ray masks, which we have found to be suitable for our research applications, were 31-mm-diameter membranes of low-stress Si-rich SiN_x, anodically bonded to optically-flat Pyrex rings. In order to avoid the difficult dry-etching and low yield associated with a multilevel process, the x-ray masks were patterned using a single layer of PMMA resist, thick enough (≥ 250 nm) to be used as a mold for plating 200 nm of Au (10 dB at 1.32 nm x rays). The PMMA was patterned using focused-ion-beam lithography and electron-beam lithography. In the case of focused-ion-beam lithography, 280 keV Be^{++} ions were used to pattern features as fine as 50 nm

100

linewidth directly onto the mask membrane. Proximity effect was absent in the FIBL due to the massive ions used, and suggests that FIBL could be a valuable tool in the patterning of x-ray masks, particularly those where thick absorbers are needed or where patterning onto high-atomic-number absorber, e.g. tungsten, is required. In the case of e-beam, 50 keV e-beam lithography was used to pattern 300 nm-thick PMMA on x-ray mask membranes. The reduction of proximity effect (relative to writing on a solid substrate), enabled the patterning of features as fine as 50 nm lines and spaces. This reduction of proximity affect is attributed to patterning on a thin membrane, where a significant number of incident electrons pass through the membrane (and out the back side) rather than backscattering into the resist. A protocol was developed for the transferral of converted pattern data from MIT to remote sites where e-beam lithography is performed. In effect, the technology developed will allow researchers access to nanolithography without having to invest in the large capital cost of a high-resolution e-beam system.

A process was developed for electroplating Au absorbers under low stress. By plating at a specific value of current density, using a confined plating geometry in a stagnant solution of BDT-510, zero-stress plated films are achieved. Monitoring of the plating bath using a computerized database ensures repeatable results.

Masks made by e-beam and focused-ion-beam lithography were replicated using x-ray lithography in both microgap and vacuum-contact configurations to make "daughter" masks. For fine-linewidth patterns (< 100 nm), vacuum-contact x-ray lithography provides better process latitude in making the daughter masks. For masks with larger features, microgap exposures were used. Experimental results were shown which demonstrates that the effects of diffraction are not as severe as had been anticipated, based upon simple scalar diffraction calculations. This disparity is attributed to the fact that in the x-ray regime the absorber should be treated as a lossy dielectric rather than as an ideal metal and hence abrupt transitions of the E-field does not occur. Moreover, the assumption of spatially coherent illumination (plane wave illumination) in previous diffraction calculations produced spurious edge ringing and did not reflect reality, i.e. partially-coherent illumination is used in practice.

101

A procedure was developed for the alignment and exposure of small GaAs substrates (smaller than the diameter of the mask membrane) using vacuum contact x-ray lithography. This is critical in quantum-effect-devices research where small substrates are common. This represents the first time contact x-ray lithography has been performed on samples smaller than the x-ray mask membrane. The advantanges of using x-ray lithography to fabricate quantum-effect devices include: (1) High contrast areal images which allow for the use of thicker resist and the liftoff of thicker metal films. Thicker metal films are more robust and allow for better step coverage (useful when fine metal lines must run down into mesa etched regions or onto coarse contact pads). (2) Large process latitude (compared to direct-write e-beam lithography). This means that the development of resist patterns is insensitive to parameters such as development time and temperature. (3) No damage to high mobility substrates [15].

Devices made using these alignment and exposure techniques were measured at cryogenic temperatures. These devices include GaAs electron waveguides and planar resonant-tunneling field-effect transistors (PRESTFET). The electron waveguide devices exhibited conductance quantization in waveguides as long as 0.75 μm at a temperature of 4.2 K – an indication of ballistic transport over that distance. This remarkable result is strong evidence that x-ray lithography and associated processing do not degrade the high mobility of MBE-grown layers. PRESTFETs with 200-nm-pitch gate electrodes were fabricated and measured. These devices did not exhibit resonant-tunneling behavior. We believe this can be attributed to the large spacing between electrodes which results in a small inter-subband spacing for energy levels in the quantum well between the electrodes. We are currently working on making daughter x-ray masks with PRESTFET patterns from 300 nm down to 100 nm pitch to investigate the device behavior as a function of electrode spacing. Future work in the device area will definitely include the replication of these masks onto substrates and the measurement of the PRESTFET devices at liquid-helium temperature.

The direction for other work in this area may be toward the study of novolak resists such as Shipley SAL-601 and Hoechst's RAY-PF and Ray-PN. These resists have

higher sensitivity and more resistance to plasma etching than PMMA. If resolution in the sub-100 nm regime can be proven with these resists (or perhaps some other novolak resist) they will prove quite useful as an etch masks for polysilicon in short-channel MOSFET work, and as an etch mask for tungsten in x-ray mask patterning.

In will also be important to explore the resolution limits of x-ray mask patterning. By optimizing focus, astigmation, and dose, it should be possible to achieve mask features below 50 nm- linewidth using 50 keV e-beam lithography (and 300 nm-thick resist). In the future, it may also be worthwhile to pursue e-beam lithography using 75 keV e-beam systems.

Appendix A

Preparation of Mask Samples for E-Beam Lithography

- Talk to the person in charge of the membrane inventory about getting some samples. The membrane blanks are kept in blue boxes right near the entrance to the inner lab of the SSL. Be careful when removing the blanks not to hit one against another. Also, check and make sure that the blanks that you take are fully finished (that is, all the processing steps have been done.

- Examine the membranes in the optical microscope for obvious defects (e.g. large scratches, bumps, etc.). Select only the best samples for further preparation.

- Place the samples in the boat designed for the mask blanks.

- Mix up a Piranha etch (3 parts sulfuric acid to 1 part hydrogen peroxide) in a beaker big enough to hold the boat. Mix enough of the solution to fully immerse the blanks. The piranha etch heats up by itself rather quickly. As with all other solutions containing acids, always wear the full acid protection gear (acid- resistant gloves, apron, and face-shield).

- Immerse the blanks into the Piranha etch. Let it sit in the etch for 15 min. While the membranes are being cleaned in the Piranha etch, fill a beaker (again, big enough to hold the boat) with hot (80°C) DI water.

- Mix up a beaker of RCA organic cleaning solution (5 parts DI water to 1 part ammonium hydroxide to one part hydrogen peroxide) and heat on the hotplate until it reaches 80°C.

- When the 15 minutes in the Piranha etch are done, remove the samples from the etch and place in the beaker of hot DI. Use the spray gun from the cleaning station to spray DI water gently into the beaker such that it overflows. Allow the water to overflow for about 2 to 3 minutes.

- Remove the samples from the DI water beaker and place into the RCA clean beaker which should be at 80°C already. This should be done quickly such that the membranes do not have a chance to dry. Dump and rinse the DI water beaker several times. Let the samples sit in the RCA cleaning solution for 15 minutes.

- While the samples are sitting in the RCA clean, carefully dump the Piranha etch solution down the drain in the sink. There should be plenty of running water in the sink before, during, and after pouring the acid down the drain.

- Fill the DI water beaker with hot DI water again.

- When the 15 minutes in the RCA is over, place the boat into the DI water beaker. Again, this should be done quickly. Again, apray hot DI water into the beaker until it overflows, and allow the water to overflow for 2-3 minutes.

- Dry the samples by gently blowing nitrogen over the front of the membrane. Be careful to remove all the water from the front of the membrane. This is where the patterns on the mask will sit, and must therefore be free of residue. Try to get most of the moisture off the back of the blank. I have found that it is pretty difficult to get the water off of the back because of the many nooks and crannies of the mask structure. Therefore, I would advise that you get the front side dry, try to get most of the water off the back side, and then place the sample face up on the hotplate above the spinning staion (set at LOW or 1

setting). This will dry the back side by evaporation. The evaporation process generally takes 5 minutes or less.

- After the blanks are dry, immediately mount them on the membrane evaporation plate (You should have previously arranged to get a double evaporation.). The first evaporation is for plating base and consists of $50\overset{\circ}{A}$ of NiCr followed by $100\overset{\circ}{A}$ of Au.

- After the first evaporation is done, the hats are flipped over to cover the membranes and a second evaporation of $2000\ \overset{\circ}{A}$ of Au is performed. This Au serves to provide electrical continuity from the Pyrex area to the area on the mesa.

- After the second evaporation is done, unload the sample from the evaporation plate, and *immediately* spin on PMMA. Use the spin chuck with the four fingers which are designed to hold the Pyrex-bonded sample. The type of PMMA you use and the thickness will depend on the type of work that you want to do. You should make up a spin curve for the PMMA that you want to use.

- After spinning on the PMMA, use a Q-tip soaked with chlorobenzene to remove the PMMA from four areas of the mesa. If the flat is at 6 o'clock, then clean small spots on the mesa at the 3, 6, 9, and 12 o'clock positions. This will later provide focusing spots in the e-beam lithography system.

- Bake the sample at 180°C for at least 90 minutes.

- Remove the sample from the oven and allow to cool. Using a pin (similar to those which have a wood stick on the end), scratch a cross in the thick Au in the regions that have been cleaned of PMMA. Do not use a scribe, as this will scratch into the Si.

- Place the sample face-down into an individual mask carrier (designed to hold the Pyrex-bonded samples). Place a spider onto the back of the sample and put the cap on. Use scotch tape to tape the top of the carrier to the bottom.

- Wrap the sample in bubble-wrap, and then scotch-tape the bubble wrap so that the sample is enclosed in the wrap.

- Place the sample(s) in the center of a box filled with styrofoam peanuts and tape the box closed. The sample are now ready for shipping out.

Appendix B

Processing the Parent Mask

Once the mother mask has been written by e-beam or focused-ion-beam lithography, it is ready to be developed and plated. This section describes the procedure.

1. Unpack the mask from its carrier carefully.

2. Set up the OAI to do a flood exposure at 220 nm wavelength. To do this, make sure the proper pair of mirrors are in and then turn on the power supply and start the lamp. Allow the lamp to warm up for about 5 min. before doing the exposure.

3. Measure the UV intensity under the light source by placing the 220 nm UV meter (set on B scale) on the table underneath the condenser lens and opening the shutter of the light source (flip the toggle switch on the back of the timer to the ON position and press the LAMP TEST button). It should read roughly 100 on the B scale (10 mW/cm^2).

4. Place the sample on the small plate with attached Chinese hat assembly. Make sure the hat covers the membrane area. Center the plate on the aligning fixture and push the alignment assembly underneath the light source. The shutter should open automatically.

5. Expose for however long it takes to expose the thickness of PMMA that you have on your sample. For 300 nm of PMMA, I usually expose for 30 min. This

is enough exposure to make the PMMA develop out almost instantaneously in 1:2 MIBK:IPA at 21°C. Since the OAI timer has a maximum time setting of 999 sec., I usually set it to 900 sec. (15 min.) and do two exposures. The second exposure can be started by pressing EXPOSE when the first exposure is done.

6. While the sample is being deep-UV exposed, do a clean-up run on the reactive-ion-etching (RIE) system to set up the parameters for an an oxygen de-scum etch. (Use the polyimide target.) The parameters are: 400 V bias, 0.13 mW/cm^2 power, 15 sccm O_2 flow rate, and 10 mtorr pressure. Let the RIE run for at least 5 min. for the system to stabilize.

7. Mix up developer and rinse in two beakers. The developer is methyl isobutyl ketone (MIBK) and isopropyl alcohol (IPA) mixed in the ratio 1:2 MIBK:IPA. The solution cools upon mixing, dropping to about 17°C. You must heat the solution on a hotplate set at a low setting (typically between 1 and 2). Be extremely careful about heating the solvents and never leave the solution unattended. It is critical that the solution be at 21 ± 0.1°C. If the temperature overshoots 21°C, cool the solution by wrapping ice packs around the beakers.

8. Once the developer temperature has settled to 21 ± 0.1°C, place the mask on a teflon holder and immerse in a solution. Agitate slowly, but constantly by stirring the teflon holder in the solution. The development time should be kept constant for each project. Do not get the urge to develop by inspection. Keep your development parameters (developer concentration, temperature, development time) exactly the same each time, and make variations at the e-beam lithography stage by designing in a dose variation.

9. Develop for the time you need. I typically use 75 sec. for samples from NRL (300 nm-thick, 950 K mol. wt. PMMA) and 120 sec. for samples exposed at IBM (250 nm-thick, 496 K mol. wt. PMMA).

10. When the development time is up, immediately transfer the samples into the IPA beaker. Do not let the developer dry while transfering between beakers.

11. Rinse in the IPA beaker for 45 sec. while stirring.

12. Blow the sample dry gently using the filtered N_2 gun. It is critical not to blow on the sample too hard. I usually set the N_2 flow rate to less than 4 psi (barely registers on the dial). Make sure the dry the back off as well.

13. Load the sample in the RIE for de-scum. Put some thin, glass cover slides onto the etch plate and then rest the mask on the cover slides. The purpose of the slides is to make sure the pyrex ring of the mask does not seal to the plate. If this happens, a pressure differential can exist across the two sides of the membrane. The RIE parameters are as follows: polyimide target, O_2 gas (15 sccm flow rate), 400 V bias, 40 W forward power, and 10 mtorr pressure.

14. Etch for 6 sec. using these parameters. This should remove any scum on the plating base as well as about 20 nm of PMMA.

15. Keep the sample under vacuum in the RIE until you are ready to plate.

16. Electroplate Au aborbers to the desired thickness (see Appendix C).

17. Strip the PMMA mold using O_2 plasma etching. At a 200 W power setting this typically takes 7-8 min.

18. Stencil-evaporate Al studs onto the mesa. The thickness of the Al studs sets the gap if a microgap configuration is to be used.

Appendix C

Au Electroplating

The procedure for plating Au absorbers onto x-ray masks follows the procedures originally discussed in Chapter 4. Before plating, get trained by the technician in charge of plating.

1. While the RIE is pumping for the de-scum step, set up the Au plating system. Begin by replacing the two particulate filters on the plating loop line.

2. Rinse out the beaker and tube by running two beakers-full of DI water through the beaker while the pump is on.

3. Pour the plating solution into the beaker. Place the plating-dedicated spin bar in the beaker.

4. Adjust the spin speed to 500 rpm and the set the pump to a pumping speed between 2 and 3.

5. Remove the Au plating thermocouple from its white box. rinse the glass-coated end with DI water and blow dry. Plug the connector end into the back of the hotplate, and place the glass-coated tip into the solution inside the glass receptacle attached to the side of the beaker.

6. Measure the pH of the solution using the pH meter. The pH of the solution should be between 8.5 and 9.0 (around 8.8 is ideal). If the pH is not in this range, see a technician.

7. Fill out the plating database.

8. Calculate the optimum, zero-stress current to be used for plating based upon the amount of area of exposed plating base (after the PMMA has been developed) multiplied by the zero-stress current density (obtained from previous monitor runs). For BDT-510, this zero-stress current density is approximately 0.8 mA/cm^2.

9. Set the Probe Temperature on the hotplate to 33°C. The solution will take about half an hour to reach this temperature. In the meantime, perform the RIE de-scum step.

10. Develop the sample in 1:2 MIBK:IPA at 21°C. If adhesion promoter is used, then use one of the following de-scum procedures:

    - Wet process (fine-linewidth or high resist aspect ratio):
        - After developing for the required time, quickly transfer the sample to an IPA beaker for rinsing being careful not to let the developer recede from the mask.
        - After IPA rinse, quickly transfer the sample to a DI water rinse beaker without letting the IPA recede from the mask. Run the DI into the beaker for 5 min. allowing it to overflow so that the IPA is rinsed away.
        - Place a small Petri dish into the Di water rinse beaker. Transfer the sample into the Petri dish under water. Transfer the Petri dish (filled with DI water) with the sample in it into a beaker of 1:3 buffered HF:DI water. Immerse in this solution for 10 sec. The purpose of this etch is to remove the MS805 adhesion promoter.
        - After 10 sec in the 1:3 buffered HF:DI water solution, transfer the Petri dish (filled with the etch solution) containing the sample into another DI water rinse beaker. Again, let the DI water rinse the etch solution away for 5 min.

- After the DI water has rinsed away the etch solution, immerse the plating sample holder into the rinse beaker. Take the sample out of the Petri dish and place in the sample holder while under water.

- With the sample holder folded so that the sample is horizontal and facing up (This arrangement traps the rinse water so that transfer can be achieved from the rinse water into the plating solution without the sample drying.), transfer into the plating solution.

- Dry process (coarse linewidth or low aspect-ratio resist):

    - After development, blow the sample gently with the N_2 gun.

    - De-scum in the RIE using the parameters 0.13 W/cm^2 power density, 400 V bias, 12 sccm O_2, 18 sccm CF_4, 10 mtorr pressure, 8 sec. etch time.

11. If adhesion promoter is not used, then use the same oxygen RIE de-scum detailed in Appendix B for the parent masks.

12. After the de-scum RIE (if a de-scum step is performed), measure the thickness of the resist. This will be used as a reference to determine the thickness of Au plated. This can be achieved by using either the Alpha-Step profilometer directly on the membrane or optically using the Linnik interferometer. Of course, if a wet process is used, it is not possible to obtain this measurement since the sample is already in the plating bath.

13. Plate at the optimum-stress current calculated earlier.

14. Measure the amount of Au plated either with the Alpha-Step or the Linnik. If the thickness is sufficient (> 200 nm for the 1.32 nm Cu_L line, or > 100 nm for the 4.4 nm C_K line), then the plating is complete. If not, place the sample back in the plating sample holder and plate at the same current as before. Repeat until the desired Au thickness is achieved.

Appendix D

Processing the Daughter Mask

1. Strip PMMA from exposed daughter mask using oxygen plasma.

2. Spin on 400 nm of polyimide. I use 3:2 PI 2610:NMP at 3 krpm for 60 sec.

3. Clean off the polyimide at the edges of the mask with a NMP soaked q-tip.

4. Bake at 130 C for half an hour and 180 C for 1 hour.

5. After taking the masks out of the oven, plasma ash for 6 sec. at 200 W in oxygen.

6. Spin on 5:15 PI:NMP to get roughly 80 nm of polyimide.

7. Bake at $140\pm5°C$ for 30 min. It is critical to keep this temperature close to 140 C, so use the temperature-controlled oven.

8. Immediately spin on 500 nm of photoresist.

9. Bake at 90 C for 25 min.

10. Expose with a 100 micron period grating flex mask.

11. Develop for 30 sec using 5:1 DI water:Shipley 351 developer.

12. Examine the grating in the optical microscope with the red filter in place.

13. Strip the resist using acetone and methanol.

14. Bake at 180 C for 1 hour.

Bibliography

[1] K. R. Early, *Experimental Characterization and Physical Modeling of Resolution Limits in Proximity Printing X-ray Lithography*. PhD thesis, Massachusetts Institute of Technology, 1991.

[2] Y. C. Ku, *Fabrication of Distortion Free X-ray Masks using Low-Stress Tungsten*. PhD thesis, Massachusetts Institute of Technology, 1991.

[3] J. Scott-Thomas, S. B. Field, M. Kastner, H. I. Smith, and D. A. Antoniadis, "Conduction oscillations periodic in the density of a one-dimensional electron gas," *Phys. Rev. Lett.*, vol. 62, p. 583, 1989.

[4] T. J. Thornton, M. Pepper, H. Ahmed, D. Andrews, and G. J. Davies, "Universal conductance fluctuations and electron coherence lengths in a narrow two-dimensional electron gas," *Phys. Rev. Lett.*, vol. 56, p. 1198, 1986.

[5] G. Timp, M. Chang, R. Behringer, J. E. Cunningham, T. Y. Chang, and R. E. Howard, "Quantum transport in an electron-wave guide," *Phys. Rev. Lett.*, vol. 59, p. 732, 1987.

[6] C. P. Umbach, P. Santhanam, C. van Haesendonck, and R. A. Webb, "Nonlocal electrical properties in mesoscopic devices," *Appl. Phys. Lett.*, vol. 50, p. 1289, 1987.

[7] K. Ismail, P. F. Bagwell, T. P. Orlando, and H. I. Smith, "Quantum phenomena in field-effect-controlled semiconductor nanostructures," *IEEE Proc.*, vol. 79, p. 1106, 1991.

[8] H. Kawata, J. M. Carter, A. Yen, and H. I. Smith, "Optical projection lithography using lenses with numerical aperture greater than unity," *Microelectron. Eng.*, vol. 9, p. 31, 1989.

[9] E. H. Anderson, *Fabrication and Electromagnetic Applications of Periodic Nanostructures.* PhD thesis, Massachusetts Institute of Technology, 1989.

[10] A. Yen, E. H. Anderson, R. Ghanbari, M. L. Schattenburg, and H. I. Smith, "An achromatic holographic configuration for 100 nm-period lithography," *Applied Optics*, vol. 31, p. 4540, 1992.

[11] T. H. P. Chang, "Proximity effect in electron-beam lithography," *Journal of Vacuum Science Technology*, vol. 12, p. 1271, 1975.

[12] S. A. Rishton and D. P. Kern, "Point exposure distribution measurements for proximity correction in electron beam lithography on a sub-100 nm scale," *J. Vac. Sci. Technol B*, vol. 5, p. 135, 1987.

[13] D. Flanders, "Replication of 175-Å lines and spaces in polymethylmethacrylate using x-ray lithography," *Appl. Phys. Lett.*, vol. 36, p. 93, 1980.

[14] K. Early, M. L. Schattenburg, and H. I. Smith, "Absence of resolution degradation in x-ray lithography for λ from 4.5 nm to 0.83 nm," *Microelectron. Eng.*, vol. 11, p. 317, 1990.

[15] R. A. Ghanbari, M. Burkhardt, D. A. Antoniadis, H. I. Smith, M. R. Melloch, K. W. Rhee, and M. C. Peckerar, "Comparative mobility degradation in modulation-doped GaAs devices after e-beam and x-ray irradiation," *J. Vac. Sci. Technol B*, vol. 10, p. 3196, 1992.

[16] G. G. Shahidi, D. A. Antoniadis, and H. I. Smith, "Electron velocity overshoot at room and liquid nitrogen temperatures in silicon inversion layers," *IEEE Electron Devices Letters*, vol. EDL-9, p. 94, 1988.

117

[17] K. Ismail, W. Chu, D. A. Antoniadis, and H. I. Smith, "Negative transconductance and negative differential resistance in a grid-gate modulation-doped field-effect transistor," *Applied Physics Letters*, vol. 54, no. 1, p. 460, 1989.

[18] M. Sekimoto, H. Yoshihara, and T. Ohkubo, "Silicon nitride single-layer x-ray mask," *J. Vac. Sci. Technol.*, vol. 21, p. 1017, 1982.

[19] A. M. Haghiri-Gosnet, F. Rousseaux, B. Kebabi, F. R. Ladan, C. Mayeux, A. Madouri, D. Decanini, J. Bourneix, F. Carcenac, H. Launois, B. Wisniewski, E. Gat, and J. Durand, "A 100-nm patterned x-ray mask technology based on amorphous SiC membranes," *J. Vac. Sci. Technol. B*, vol. 8, p. 1565, 1990.

[20] G. M. Wells, S. Palmer, F. Cerrina, A. Purdes, and B. Gnade, "Radiation stability of SiC and diamond membranes as potenial x-ray lithography mask carriers," *J. Vac. Sci. Technol. B*, vol. 7, p. 1575, 1989.

[21] A. Moel, W. Chu, K., Y.-C. Ku, E. Moon, F. Tsai, H. I. Smith, M. Schattenburg, C. Fung, F. Griffith, and L. Haas, "Fabrication and characterization of high-flatness mesa-etched silicon nitride x-ray masks," *Journal of Vacuum Science Technology B*, vol. 9, no. 6, p. 3287, Nov/Dec 1991.

[22] C. P. Umbach and A. N. Broers, "Experimental determination of the proximity effect from 25 to 100 keV in electron beam patterned x-ray masks," *J. Vac. Sci. Technol. B*, vol. 8, p. 1614, 1990.

[23] A. Yen, R. A. Ghanbari, Y. C. Ku, W. Chu, M. L. Schattenburg, J. M. Carter, and H. I. Smith, "X-ray masks with large-area 100nm-period gratings for quantum-effect device applications," *Microelectronic Engineering*, vol. 13, p. 271, 1991.

[24] W. Chu, A. Yen, K. Ismail, M. I. Shepard, H. J. Lezec, C. R. Musil, J. Melngailis, Y.-C. Ku, J. M. Carter, and H. I. Smith, "Sub-100-nm x-ray mask technology using focused-ion-beam lithography," *J. Vac. Sci. Technol. B*, vol. 7, p. 1583, 1989.

[25] W. Chu, H. I. Smith, S. A. Rishton, D. P. Kern, and M. L. Schattenburg, "Fabrication of 50 nm line-and-space x-ray masks in thick Au using a 50 keV electron beam system," *J. Vac. Sci. Technol. B*, vol. 10, p. 118, 1992.

[26] W. Chu, C. C. Eugster, A. Moel, E. E. Moon, M. L. Schattenburg, H. I. Smith, K. W. Rhee, M. C. Peckerar, and M. R. Melloch, "Conductance quantization in a GaAs electron waveguide device fabricated by x-ray lithography," *J. Vac. Sci. Technol B*, vol. 10, p. 2966, 1992.

[27] S. Matsui, Y. Kojima, and Y. Ochiai, "High-resolution focused ion beam lithography," *Applied Physics Letters*, vol. 53, p. 868, 1988.

[28] R. L. Kubena, F. P. Stratton, J. W. Ward, G. M. Atkinson, and R. J. Joyce, "Sub-20-nm-wide line fabrication in poly(methylmethacrylate) using a Ga^+ microprobe," *Journal of Vacuum Sciences and Technology B*, vol. 7, p. 1798, 1989.

[29] L. Karapiperis, I. Adesida, C. A. Lee, and E. D. Wolf, "Ion beam exposure profiles in PMMA – computer simulation," *Journal of Vacuum Sciences and Technology*, vol. 19, p. 1259, 1981.

[30] E. H. Anderson, D. P. Kern, and H. I. Smith, "Fabrication by tri-level electron-beam lithography of x-ray masks with 50nm linewidths, and replication by x-ray nanolithography," *Microelectronic Engineering*, vol. 6, p. 541, 1987.

[31] J. Melngailis, "Focused ion beam technology and applications," *J. Vac. Sci. Technol. B*, vol. 5, p. 469, 1987.

[32] H. Goldstein, *Classical Mechanics*. Reading, MA: Addison-Wesley, 2nd ed., 1980.

[33] S. A. Rishton and D. P. Kern, "Point exposure distribution measurements for proximity correction in electron beam lithography on a sub-100 nm scale," *J. Vac. Sci. Technol. B*, vol. 5, p. 135, 1987.

[34] S. D. Hector, R. A. Ghanbari, H. Y. Li, , H. I. Smith, and M. L. Schattenburg, "Process window for e-beam and x-ray lithography, accounting for both

aerial-image and resist-development effects." Abstract submitted to the 37th International Symposium on Electron, Ion, and Photon Beams, San Diego, CA, June 1993.

[35] R. A. Ghanbari, W. Chu, E. E. Moon, M. Burkhardt, K. Yee, D. A. Antoniadis, H. I. Smith, M. L. Schattenburg, K. W. Rhee, R. Bass, M. C. Peckerar, and M. R. Melloch, "Fabrication of parallel quasi-one-dimensional wires using a novel conformable x-ray mask technology," *J. Vac. Sci. Technol B*, vol. 10, p. 3196, 1992.

[36] S. A. Rishton, D. P. Kern, E. Kratschmer, and T. H. P. Chang, "Electron beam lithography of sub-0.1μm circuits," *Microelectronic Engineering*, vol. 9, p. 183, 1989.

[37] G. Billingsley and K. Keller, *KIC: A graphics editor for integrated circuits*. Berkeley, CA: University of California at Berkeley, 1980.

[38] Y.-C. Ku, L. P. Ng, R. Carpenter, K. Lu, H. I. Smith, L. E. Haas, and I. Plotnik, "In-situ stress monitoring and deposition of zero stress W for x-ray masks," *J. Vac. Sci. Technol. B*, vol. 9, p. 3297, 1991.

[39] K. Rhee, D. I. Ma, M. Peckerar, R. A. Ghanbari, and H. I. Smith, "Proximity effect reduction in x-ray mask making using thin insulating layers." Presented at the 36th International Symposium on Electron, Ion, and Photon Beams, Orlando FL, May 1992. To be published in the Journal of Vacuum Science and Technology B Nov/Dec 1992.

[40] C. W. Jurgensen, R. R. Kola, A. E. Novembre, W. W. Tai, J. Frackoviak, L. E. Trimble, and G. K. Celler, "Tungsten patterning for 1:1 x-ray masks," *J. Vac. Sci. Technol. B*, vol. 9, p. 3280, 1991.

[41] G. E. Georgiu, C. A. Janoski, and T. A. Palumbo in *Electron-Beam, X-ray, and Ion-Beam Techniques for Submicrometer Lithographies III* (A. Wagner, ed.), p. 96, SPIE, Bellingham, 1984.

[42] Enthome-OMI, Inc., Westhaven, CT 06156.

[43] International Micro Industries, Inc., Cherry Hill NJ 08003.

[44] G. G. Stoney *Proc. R. Soc. London Ser. A*, vol. 82, p. 172, 1909.

[45] S. L. Chiu and R. E. Acosta, "Electrodeposition of low stress gold for x-ray mask," *J. Vac. Sci. Technol B*, vol. 8, p. 1589, 1990.

[46] Au plating database implemented by Dr. Mark Schattenburg of the MIT Center for Space Research.

[47] R. Feder, E. Spiller, and J. Topalian, "Replication of 0.1 μm geometries with x-ray lithography," *J. Vac. Sci. Technol.*, vol. 12, p. 1975, 1975.

[48] K. Deguchi, T. Ishiyama, T. Horiuchi, and A. Yoshikawa, "Effects of photo- and auger electron scattering on resolution and linewidth control in SR lithography," in *Proceedings of the 1990 International Microprocess conference* (S. Namba and T. Kitayama, eds.), (Tokyo, Japan), p. 100, Japanese Journal of Applied Physics, July 1990.

[49] A. C. Warren, I. Plotnik, E. H. Anderson, M. L. Shattenburg, D. A. Antoniadis, and H. I. Smith, "Fabrication of sub-100 nm linewidth periodic structures for study of quantum effects from interference and confinement in Si inversion layers," *Journal of Vacuum Science Technology B*, vol. 4, no. 1, pp. 365–368, Jan/Feb 1986.

[50] K. Murata, M. Tanaka, and H. Kawata, "Theoretical study of energy absorption on x-ray lithography with monochromatic x-rays," *Optik*, vol. 84, p. 163, 1990.

[51] J. A. Bearden, "X-ray wavelengths," *Rev. Mod. Phys.*, vol. 39, pp. 78–124, 1967.

[52] E. P. Bertin, *Principles and Practice of X-ray Spectrometric Analysis*. New York: Plenum, 1975.

[53] A. Faessler. Landolt-Börnstein: Zahlenwerte und Funktionen, 6 Auflage, 1. Band, 4. Teil (Springer, Berlin, 1955) p. 769.

[54] S. D. Hector, M. L. Schattenburg, E. H. Anderson, W. Chu, V. V. Wong, and H. I. Smith, "Modeling and experimental verification of illumination and diffraction effects on image quality in x-ray lithography," *J. Vac. Sci. Technol B*, vol. 10, p. 3164, 1992.

[55] B. J. Lin, "A comparison of projection and proximity printings–from uv to x-ray," *Microelectronic Engineering*, vol. 11, p. 137, 1990.

[56] J. Goodman, *Introduction to Fourier Optics*. San Francisco: McGraw-Hill, 1968.

[57] M. L. Schattenburg, K. Li, R. T. Shin, J. A. Kong, D. B. Olster, and H. I. Smith, "Electromagnetic calculation of soft x-ray diffraction 0.1-μm scale gold structures," *J. Vac. Sci. Technol B*, vol. 9, p. 3232, 1991.

[58] B. L. Henke, P. Lee, T. J. Tanaka, R. L. Shimabukuro, , and B. K. Fujikawa. At. Data Nucl. Data Tables **27**, 1 (1982).

[59] M. Schattenburg, K. Early, Y.-C. Ku, W. Chu, M. Shepard, S.-C. The, H. Smith, D. Peters, R. Frankel, D. Kelly, and J. Drumheller, "Fabrication and testing of 0.1 μm-linewidth microgap x-ray masks," *J. Vac. Sci. Technol. B*, vol. 8, p. 1604, 1990.

[60] M. L. Schattenburg, I. Tanaka, and H. I. Smith, "Microgap x-ray nanolithography," *Microelectronic Engineering*, vol. 6, p. 273, 1987.

[61] MS805, MicroSi Products, 10028 S. 51st St., Phoenix, AZ 85044.

[62] J. N. Helbert, "Photoresist adhesion promoters for gold metallization processing," *J. Electrochem. Soc.*, vol. 131, pp. 451–452, 1984.

[63] A. Moel, M. L. Schattenburg, J. M. Carter, and H. I. Smith, "A compact, low-cost system for sub-100 nm x-ray lithography," *J. Vac. Sci. Technol. B*, vol. 8, p. 1648, 1990.

[64] R. Ghanbari, *private communication*.

[65] B. J. van Wees, H. van Houten, C. W. J. Beenakker, J. G. Williamson, L. P. Kouwenhoven, D. van der Marel, and C. T. Foxon *Phys. Rev. Lett.*, vol. 60, p. 848, 1988.

[66] D. A. Wharam, T. J. Thornton, R. Newbury, M. Pepper, and G. A. C. Jones *J. Phys. C*, vol. 21, p. L209, 1988.

[67] R. Dingle, H. L. Stormer, A. C. Gossard, and W. Wiegman *Appl. Phys. Lett.*, vol. 33, p. 665, 1978.

[68] C. C. Eugster, J. A. del Alamo, P. Belk, and M. J. Rooks *Appl. Phys. Lett.*, vol. 58, p. 2966, 1991.

[69] C. C. Eugster, J. A. del Alamo, and M. J. Rooks *Japan. Journ. Appl. Phys.*, vol. 29, p. L2257, 1990.

[70] K. Ismail, D. A. Antoniadis, and H. I. Smith, "Lateral resonant tunneling in a double-barrier field-effect transistor," *Appl. Phys. Lett.*, vol. 55, p. 589, 1989.

[71] S. Y. Chou, J. J. S. Harris, and R. F. W. Pease *Appl. Phys. Lett.*, vol. 52, p. 1982, 1988.

[72] K. Ismail, *The Study of Electron Transport in Field-Effect-Induced Quantum Wells on GaAs/AlGaAs.* PhD thesis, Massachusetts Institute of Technology, 1989.